

ELECTRON TRANSPORT STUDIES OF THE FERROMAGNETIC
SEMICONDUCTOR CALCIUM HEXABORIDE

By

STEPHANIE A. GETTY

A DISSERTATION PRESENTED TO THE GRADUATE SCHOOL
OF THE UNIVERSITY OF FLORIDA IN PARTIAL FULFILLMENT
OF THE REQUIREMENTS FOR THE DEGREE OF
DOCTOR OF PHILOSOPHY

UNIVERSITY OF FLORIDA

2001

I dedicate this dissertation to my parents for giving me the intellectual freedom to make my own way.

ACKNOWLEDGMENTS

I would like to express my thanks to those who have played a crucial part in my development as a physicist. I would especially like to express my sincerest gratitude toward the chair of my graduate committee, Professor Arthur Hebard, for his generous support when I needed it most, for the critical reading of this dissertation, and for kindly allowing me to participate as a member of his group. I would also like to thank the members of my supervisory committee for having given me indispensable guidance and support: Professor Andrew Rinzler, Professor Cammy Abernathy, and Professor Selman Hershfield.

I would like to express my appreciation to the department staff, in particular Janet Germany for her infinite patience, and Darlene Latimer and Susan Rizzo for the lengths they have gone to in my best interest. Many thanks to the Machine Shop personnel for all their excellent work that has made my research possible: Mark Link, Bill Malphurs, Ed Storch, Ted Melton, John Van Leer, Stephen Griffin, and Bob Fowler.

I extend my thanks to all my family and friends, who have given me encouragement and without whom I would not be the person I am.

TABLE OF CONTENTS

	<u>page</u>
ACKNOWLEDGMENTS	iii
LIST OF FIGURES	vi
ABSTRACT	ix
CHAPTERS	
1 INTRODUCTION	1
1.1 Electronic and Magnetic Properties of the Hexaboride Family of Compounds	2
1.1.1 The Divalent Hexaborides	3
1.1.2 The Rare Earth Hexaborides	5
1.1.3 Valence Fluctuating SmB_6 and CeB_6	6
1.1.4 Ferromagnetic EuB_6	8
1.2 Doping Studies of the Hexaborides	11
1.2.1 Carbon Doping of EuB_6	11
1.2.2 Lanthanum and Ytterbium Doping of SmB_6	13
1.2.3 Cerium and Thorium Doping of CaB_6	14
2 PREVIOUS WORK IN CaB_6 AND RELATED COMPOUNDS	17
2.1 Electron Tunneling Spectroscopy in EuB_6	17
2.2 Recent Experimental and Theoretical Results in CaB_6 and SrB_6	20
2.2.1 Theoretical Studies	20
2.2.2 Experimental Studies	25
3 PURPOSE OF EXPERIMENT	41
3.1 Technological Motivation	42
3.2 Electrical Conductivity in Metals and Semiconductors	44
3.2.1 Electrons in Applied Magnetic Field I: Magnetoresistance	45
3.2.2 Electrons in Applied Magnetic Field II: Hall Effect	48
3.3 Electron Tunneling Spectroscopy	51
3.3.1 Theory of Tunneling	51

3.3.2 Zero Bias Anomalies	56
4 EXPERIMENTAL TECHNIQUES	60
4.1 Crystal Growth and Doping.....	60
4.2 Transport Measurement Techniques	61
4.2.1 Resistivity, Hall Effect, and Magnetoresistance	62
4.2.2 Tunneling Spectroscopy	65
5 PRESENTATION OF RESULTS	72
5.1 Resistivity Measurements.....	73
5.2 Hall Effect Measurements	79
5.3 Magnetoresistance Measurements.....	84
5.4 Tunneling Measurements	86
6 INTERPRETATION AND MODELING OF THE DATA	91
6.1 Interpretation of the Data.....	91
6.1.1 $\text{Ca}_{1-\delta}\text{La}_\delta\text{B}_6$	91
6.1.2 Stoichiometric CaB_6	102
6.1.3 $\text{Ca}_{1-\delta}\text{B}_6$	106
6.2 Band Structure Model.....	111
7 SUMMARY	115
7.1 Synopsis of Experimental Results	115
7.2 Future Directions	116
LIST OF REFERENCES.....	118
BIOGRAPHICAL SKETCH.....	125

LIST OF FIGURES

<u>Figure</u>	<u>Page</u>
1-1. CsCl crystal structure of the hexaborides.....	3
1-2. Tunneling conductance versus bias voltage in SmB_6	6
1-3. Resistivity versus temperature in EuB_6	8
1-4. Resistivity versus temperature in EuB_6 at various magnetic fields.	9
1-5. Resistivity and $d\rho/dT$ versus temperature in EuB_6	10
2-1. Tunneling conductance versus bias voltage in EuB_6	19
2-2. The evolution of a semimetallic band structure with excitonic ordering.....	21
2-3. The band structure of an excitonic system with electron doping.....	22
2-4. Magnetization versus temperature in $\text{Ca}_{0.995}\text{La}_{0.005}\text{B}_6$ showing a T_C of approximately 600 K.	26
2-5. Magnetization versus magnetic field at various La doping concentrations.....	27
2-6. Resistivity versus temperature in the electron doped $\text{Ca}_{1-\delta}\text{La}_\delta\text{B}_6$, Ca-deficient CaB_6 , and stoichiometric $\text{Ca}_{1+\delta}\text{B}_6$ (first report).	28
2-7. Resistivity versus temperature in $\text{Ca}_{1+\delta}\text{B}_6$ (first report).	29
2-8. Specific heat versus temperature in $\text{Ca}_{1+\delta}\text{B}_6$ and $\text{Ca}_{0.995}\text{La}_{0.005}\text{B}_6$ (first report).....	29
2-9. Spin relaxation rate versus temperature in SrB_6 at various magnetic fields.....	31
2-10. Optical reflectivity versus frequency in $\text{Ca}_{0.995}\text{La}_{0.005}\text{B}_6$, $\text{Ca}_{0.99}\text{La}_{0.01}\text{B}_6$, and CaB_6	32
2-11. Angle resolved photoemission spectra in stoichiometric CaB_6	33
2-12. SXE and PFY intensities versus photon energy in various hexaborides.	34
2-13. Electron spin resonance spectra in $\text{Ca}_{0.995}\text{La}_{0.005}\text{B}_6$	35

2-14. Magnetization versus magnetic field in $\text{Ca}_{0.995}\text{La}_{0.005}\text{B}_6$ and CaB_6 grown by FZ and Al-flux techniques.	36
2-15. Resistivity versus temperature in $\text{Ca}_{0.995}\text{La}_{0.005}\text{B}_6$ and CaB_6 grown by FZ and Al-flux techniques.	38
2-16. Magnetization versus magnetic field in polycrystalline CaB_6 : growth conditions.	39
2-17. Magnetization versus magnetic field in polycrystalline CaB_6 : ferromagnetism and diamagnetism.	39
2-18. Resistivity versus temperature in polycrystalline CaB_6	40
3-1. Resistivity versus applied magnetic field in EuB_6	47
3-2. Magnetoresistance versus applied magnetic field in SmB_6	48
3-3. Contact configuration for performing Hall effect measurements.	49
3-4. Schematic of electron tunneling.	52
3-5. Normalized tunneling conductance versus positive bias voltage in a BCS superconductor.	54
3-6. Tunneling conductance versus positive bias voltage in a Pb-I-Pb tunnel junction.	55
3-7. Zero bias anomalies in the tunneling resistance versus bias voltage for a Cr-CrO _x -Ag tunnel junction.	57
3-8. Zero bias anomalies in the tunneling conductance versus bias voltage for magnetically doped electrodes of (a) Ag and (b) Al.	58
4-1. Contact configuration for simultaneous measurement of resistivity, magnetoresistance, and Hall effect.	62
4-2. Depiction of ⁴ He cryostat with pump-out port used for magnetotransport measurements.	64
4-3. Cross-section of tunnel junction.	66
4-4. I-V characteristic of a EuB_6 -I-Pb tunnel junction.	67
4-5. Circuit diagram for tunneling measurements.	70
5-1. Normalized resistivity versus temperature in $\text{Ca}_{1-\delta}\text{La}_\delta\text{B}_6$	74
5-2. Normalized resistivity versus temperature in CaB_6	74
5-3. Normalized resistivity versus temperature in $\text{Ca}_{1-\delta}\text{B}_6$	75

5-4. Fits of resistivity versus temperature to activated form in $\text{Ca}_{1-\delta}\text{B}_6$	76
5-5. Resistance versus temperature in $\text{Ca}_{1-\delta}\text{B}_6$ prior to and following O_2 anneal.	78
5-6. High temperature region of Figure 5.5.....	78
5-7. Carrier concentration and normalized resistivity versus temperature in $\text{Ca}_{1-\delta}\text{La}_\delta\text{B}_6$	79
5-8. Carrier concentration and normalized resistivity versus temperature in $\text{Ca}_{1-\delta}\text{B}_6$	80
5-9. Carrier concentration and normalized resistivity versus temperature in CaB_6	81
5-10. Hysteresis in Hall voltage versus magnetic field in CaB_6 at 4.2 K.....	83
5-11. Hysteresis in magnetization versus magnetic field in CaB_6 at 4.2 K.....	83
5-12. Magnetoresistance versus magnetic field in $\text{Ca}_{1-\delta}\text{La}_\delta\text{B}_6$	85
5-13. Magnetoresistance versus magnetic field in CaB_6	85
5-14. Magnetoresistance versus magnetic field in $\text{Ca}_{1-\delta}\text{B}_6$	86
5-15. Tunneling conductance versus bias voltage in $\text{Ca}_{1-\delta}\text{La}_\delta\text{B}_6$	87
5-16. Tunneling conductance versus bias voltage in $\text{Ca}_{1-\delta}\text{La}_\delta\text{B}_6$	89
5-17. Tunneling conductance versus bias voltage in $\text{Ca}_{1-\delta}\text{La}_\delta\text{B}_6$ (a) for $15 \text{ K} < T < 40 \text{ K}$ and (b) for $2 \text{ K} < T < 20 \text{ K}$	90
6-1. Normalized conductivity versus $T^{1/2}$ in $\text{Ca}_{1-\delta}\text{La}_\delta\text{B}_6$ for $5 \text{ K} < T < 24 \text{ K}$	95
6-2. Normalized resistivity versus $\ln T$ in $\text{Ca}_{1-\delta}\text{La}_\delta\text{B}_6$ for $5 \text{ K} < T < 28 \text{ K}$	97
6-3. $\Delta R/R^2$ versus $H^{1/2}$ in $\text{Ca}_{1-\delta}\text{La}_\delta\text{B}_6$	100
6-4. Magnetoresistance in CaB_6 versus (a) H^2 for $0 \text{ T} < H < 2.5 \text{ T}$ and (b) H for $2 \text{ T} < H < 6 \text{ T}$	104
6-5. Mobility versus temperature in $\text{Ca}_{1-\delta}\text{B}_6$	108
6-6. Magnetoresistance in $\text{Ca}_{1-\delta}\text{B}_6$ versus (a) H^2 for $0 \text{ T} < H < 2.5 \text{ T}$ and (b) H for $1.5 \text{ T} < H < 6 \text{ T}$	110
6-7. Band structure model depicting shifts in Fermi level as a function of doping level.	112

Abstract of Dissertation Presented to the Graduate School
of the University of Florida in Partial Fulfillment of the
Requirements for the Degree of Doctor of Philosophy

ELECTRON TRANSPORT STUDIES OF THE FERROMAGNETIC
SEMICONDUCTOR CALCIUM HEXABORIDE

By

Stephanie A. Getty

December 2001

Chairman: Professor Arthur F. Hebard

Major Department: Physics

Because the alkaline earth and rare earth hexaborides straddle the metal-insulator and magnetic-non-magnetic transitions, this class of materials has consistently been a source of interest. The discovery that CaB_6 , when lightly electron-doped and without any inherent magnetic constituent, exhibits long-range ferromagnetism to a Curie temperature of 600 K further enhances the reputation of the hexaborides for their unusual properties.

Experimental results are presented of electron transport studies of the novel ferromagnet CaB_6 in three doping concentrations: stoichiometric CaB_6 , electron-doped $\text{Ca}_{1-\delta}\text{La}_\delta\text{B}_6$, and Ca-deficient $\text{Ca}_{1-\delta}\text{B}_6$. In particular, dependences of electronic properties on temperature and applied magnetic field were studied. These investigations were conducted to advance the understanding of the origin of this unusual ferromagnetism.

Upon measurement of the quantities of resistivity, magnetoresistance, Hall effect, and electron tunneling spectra, a band structure model consistent with our results has been formulated. We have discovered that CaB_6 single crystals, when grown in excess Ca to counteract the tendency to form Ca vacancies, exhibit semimetallic behavior with a

Fermi level marginally crossing the conduction band separated in energy from the valence band. This result contradicts theoretical expectations of a semiconductor or compensated semimetal. The La-doped counterpart is metallic, as expected. The Ca-deficient compound, however, retains a low electron concentration while exhibiting semiconducting transport properties, implying that the Fermi level resides near the bottom of the conduction band within the semiconducting gap.

Recent theoretical efforts, in addition to predictions of a polarized electron fluid and the formation of a doped excitonic insulator, have proposed that an impurity-induced magnetic moment is conceivable. The results of this work are consistent with the presence of an impurity band and may indicate the validity of a theory of impurity-driven ferromagnetism.

Owing to the combination of a high T_C , low carrier density, and proximity to semiconducting behavior, this novel ferromagnet may be applicable to the field of spintronics, in which the exploitation of the spin degree of freedom aims for integration of spin-based devices into the semiconductor industry. The control of electronic spin in semiconducting devices suggests a variety of technologically important applications, including spin-based transistors, light emitting diodes, and optical sensors.

CHAPTER 1 INTRODUCTION

Metal and rare earth hexaborides have been the focus of extensive experimental and theoretical studies for over three decades. The source of continuing interest is the diversity exhibited throughout this class of materials, owing in part to an unusually sensitive band structure. Small changes in this band configuration tend to result in profound alterations of the physical properties of these systems. Additionally, the magnetic properties exhibited by some of the rare earth hexaborides were found to be very sensitive to electron concentration, prompting studies of the magnetic phase diagrams of these compounds. The discovery of magnetism in CaB_6 , in which there are no magnetic constituents, is a recent example of the interesting physics displayed by the hexaboride family. Electron-doped, stoichiometric, and Ca-deficient CaB_6 comprise the focus of this work.

This chapter will present a general introduction to the hexaborides, emphasizing the importance of these materials in the field of correlated electron systems. An overview of electron transport and the nature of magnetism in these compounds is given in section 1.1. Doping studies will be discussed in section 1.2, including those that led Young et al. to investigate La-doped CaB_6 .

In chapter 2, a review of experimental results obtained by other workers for EuB_6 , CaB_6 , and SrB_6 , a divalent hexaboride very similar to CaB_6 , is presented. An introduction to the experimental quantities probed in these studies is given in chapter 3. Experimental techniques and equipment will be detailed in chapter 4, including sample

growth and preparation, low temperature methods, and measurement procedures, followed by a thorough account of results in chapter 5. Chapter 6 will consist of an interpretation of the work presented in this dissertation, and chapter 7 will summarize.

1.1 Electronic and Magnetic Properties of the Hexaboride Family of Compounds

Although early work on the metal borides dates back to the early 1950s, this class of compounds first became a focus of intense research in the late 1960s. Many of the studies have involved the rare earth and alkaline earth hexaborides. These materials exist in the CsCl crystal structure, in which a cage of B_6 octahedra surrounds the metal atom, as shown in Figure 1-1. Divalent hexaborides were long considered semiconducting, as will be discussed below, and the presence of trivalent (tetravalent) cations gives rise to metallicity with an estimated one (two) conduction electron(s) per metal atom. It follows that these compounds are excellent candidates for the study of the metal-insulator transition. Because the hexaborides are isostructural in the presence of different cations, doping studies have been a major component of the experimental efforts concerning these materials.

Subsection 1.1.1 will serve to present generally obeyed properties of the divalent hexaborides. Subsection 1.1.2 will introduce the electronic and magnetic characteristics of the rare earth hexaborides, while subsections 1.1.3 and 1.1.4 focus on the intermediate valence compound SmB_6 and the ferromagnet EuB_6 , respectively.

As the field has evolved, the experimental and theoretical investigations that have been conducted on these compounds have become the source of much dispute. In particular, the electronic transport properties of the divalent hexaborides, including EuB_6 , are not easily interpreted to be metallic or semiconducting. The origins of long-range

magnetic order in EuB_6 and the topic of this work, CaB_6 , are still subject to much scrutiny.

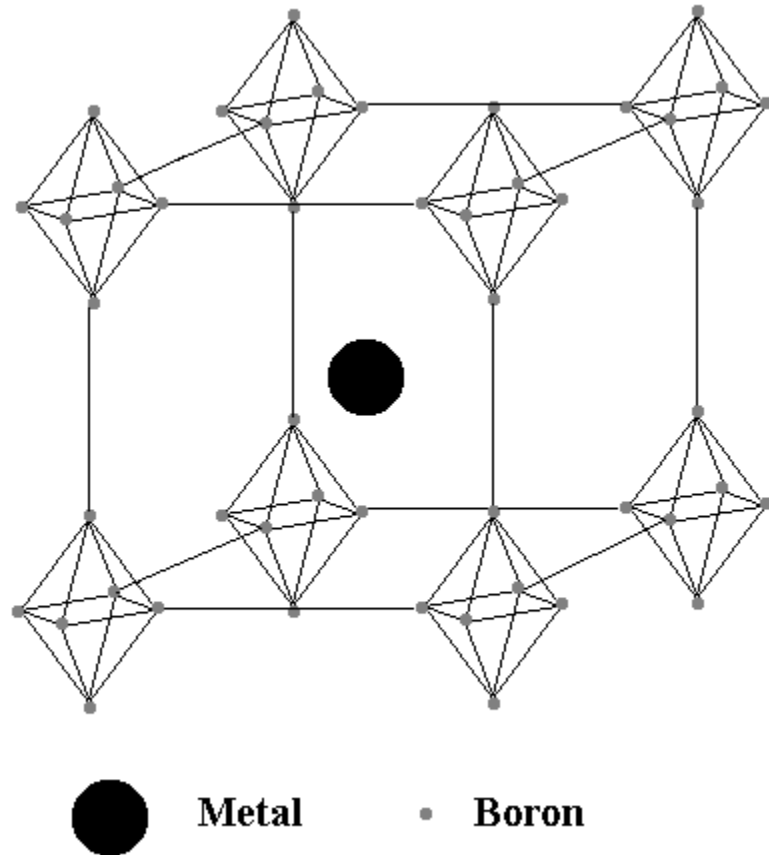


Figure 1-1. CsCl crystal structure of the hexaborides.

1.1.1 The Divalent Hexaborides

The electronic properties of the divalent hexaborides, represented by CaB_6 , SrB_6 , BaB_6 , YbB_6 , and EuB_6 , to be discussed separately below, were long considered to be well understood. Longuet-Higgins and Roberts [1] performed early calculations of the electronic configuration of the B_6 octahedron. The analysis considers that each boron donates 3 electrons to the system; one is a 2p electron, while the other two are 2s

electrons. For a group of six boron atoms, then, there are 18 electrons that can participate in bonding. In preparation for using the tight-binding approximation, these workers enumerated the orbitals available for filling for each octahedron in terms of symmetry groups. By calculating the energy contained in each bond, bonding orbitals were differentiated from anti-bonding orbitals. Of the bonding type, there are seven, each of which can hold two electrons of opposite spin. Combining these 14 orbitals with those bonding between borons and the neighboring octahedron, of which there are six, the total electron capacity required for full covalent character is 20. The implication is that the combination in a unit cell of a divalent metal with the 18 electrons native to the B_6 group gives a fully covalent structure. Measurements of the temperature dependences of resistivity in single- and poly-crystals of the divalent, non-magnetic hexaborides produced activated behaviors, enforcing the apparent correctness of the semiconducting model [2].

Heat capacity studies of the divalent hexaborides reveal a small electronic contribution at low temperatures [3]. The magnitude of this signal is interpreted to reflect a small density of states located at the Fermi level, which in turn reflects a low carrier concentration, in agreement with the semiconductor-like behavior of the resistivity.

Nuclear magnetic resonance (NMR) measurements of ^{11}B chemical shifts in CaB_6 , SrB_6 , and BaB_6 lent further credence to the claim that the alkaline earth hexaborides are semiconducting [4]. The B^{11} chemical shifts measured in powdered samples indicate a diamagnetic response, which the author interprets to be a signature of semiconductivity.

Owing to the excellent agreement between theory and experiment, the alkaline earth hexaborides were somewhat neglected for a number of years. Though similar results were obtained 18 years earlier by Hasegawa and Yanase [5], a re-evaluation of electron transport behavior in these compounds was instigated in 1997 by band structure calculations by Massidda et al. [6], predicting semimetallic behavior for EuB_6 , SrB_6 , and CaB_6 . Due to the near-equality of the inter- and intra- B_6 octahedral bond lengths in these materials, a small, symmetry-induced overlap between the calcium d band and boron p band at the X point of the Brillouin zone was predicted. Subsequent experimental attempts to verify semi-metallicity in the alkaline earth hexaborides have produced conflicting results. Recent results for SrB_6 and CaB_6 will be shown in chapter 2 and compared with the results of this work in chapters 5 and 6.

1.1.2 The Rare Earth Hexaborides

The majority of the rare earth hexaborides are metallic conductors, due to the typically trivalent cation present in the structure. Within the simple interpretation, two of the rare earth electrons contribute to fill the outer shell of the B_6 group, while the third electron exists in a charge conducting state. Resistivity measurements indicate a clearly metallic behavior [7], and measurements of the work function, especially that of LaB_6 , NdB_6 , PrB_6 , and their alloys, reveal that these hexaborides are useful in applications as thermionic emitters [8].

Most of the rare earth hexaborides exhibit some form of long-range order at low temperatures. The most common of these ordering mechanisms is antiferromagnetism through the RKKY exchange mechanism, which is strongly influenced by crystal field effects, as is seen in CeB_6 , PrB_6 , NdB_6 , GdB_6 , TbB_6 , DyB_6 , and HoB_6 . Superconductivity is seen in diamagnetic LaB_6 below 1.3 K and in YB_6 below 7.1 K [9,10].

1.1.3 Valence Fluctuating SmB_6 and CeB_6

The rare earth compound SmB_6 is not easily classified as a divalent or trivalent hexaboride, as it is a mixed-valence system. In the mid-1970s, the considerable interest in intermetallic compounds motivated extensive studies of SmB_6 , in which the ratio of Sm^{3+} to Sm^{2+} was found to be 7:3 and roughly independent of temperature [11]. A simple analysis dictates that this material should be metallic, since each Sm^{3+} ion donates one conduction electron to the system. Resistivity measurements have instead revealed semiconductor-like behavior initially attributed to a small insulating gap, featuring an activated rise at high temperatures followed by a low-temperature plateau region.

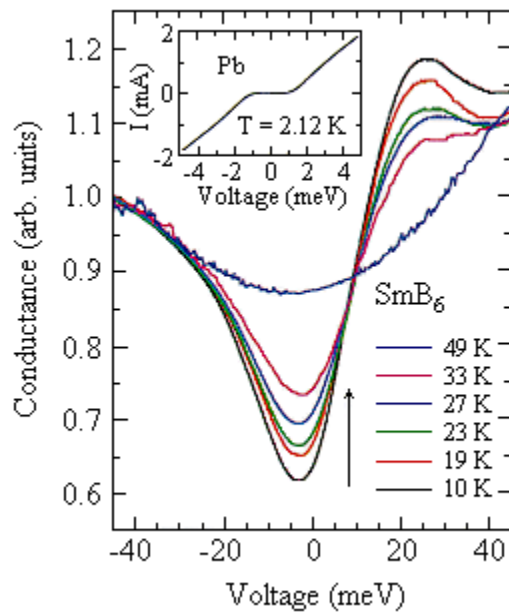


Figure 1-2. Tunneling conductance versus bias voltage in SmB_6 . The arrow denotes the location of the gap edge in energy. The depletion of the density of states near zero is evidence for a pseudo-gap [18].

The form of the resistivity for SmB_6 is consistent with the development of a small gap in the density of states at low temperatures suggested by several workers [12-17].

Tunneling measurements of SmB_6 , shown in Figure 1-2, confirm the appearance of a

pseudo-gap below approximately 40 K [18], where the density of states is steadily reduced with a power-law dependence on temperature. Note the redistribution of electronic states to energies above the gap energy, denoted by the arrow. The origin of the gap is thought to be hybridization between the closely situated f- and d-bands, as proposed by Mott in 1974 [15]. Other workers have instead proposed the formation of a Wigner crystal in which the interaction dominating the kinetic energy may not be coulombic in nature [19]. Later work has proposed that intra-gap impurity bands, due to such defects as Sm vacancies, dominate the low-temperature region [20-22].

While the trivalent Sm cation carries a magnetic moment, SmB_6 has not been found to exhibit long-range order. A paramagnetic response of magnetization to the application of magnetic field appears to persist to temperatures well below 1 K. The most likely scenario to account for the absence of long-range magnetism is the significant spatial separation between trivalent cations. In such a configuration and with a carrier concentration low enough to produce semiconducting behavior, magnetic ordering is difficult to produce by way of the RKKY interaction.

CeB_6 is also classified as a valence fluctuating compound. Magnetic ordering in CeB_6 has been given special attention due to its complicated phase diagram, which exhibits three distinct phases as the material is cooled [23]. At high temperatures, CeB_6 behaves like a typical dense Kondo system with a Kondo temperature of approximately 1 K. At temperatures between 2.4 K and 3.2 K, the material undergoes an antiferroquadrupolar ordering. With the ground state of these moments being the Γ_8 quartet, the Ce atoms are best described by quadrupole moments. Antiferromagnetic ordering of these moments commensurate with the lattice is the phase in which CeB_6

exists at intermediate temperatures. Below 2.4 K, CeB₆ exists in a classical antiferromagnetic phase.

1.1.4 Ferromagnetic EuB₆

Until the discovery of ferromagnetism in CaB₆, EuB₆ was the sole ferromagnetic exception to the generally antiferromagnetic ordering shown in the hexaborides. A review of experimental results for EuB₆ may prove helpful in determining the origin of certain features appearing in CaB₆ data.

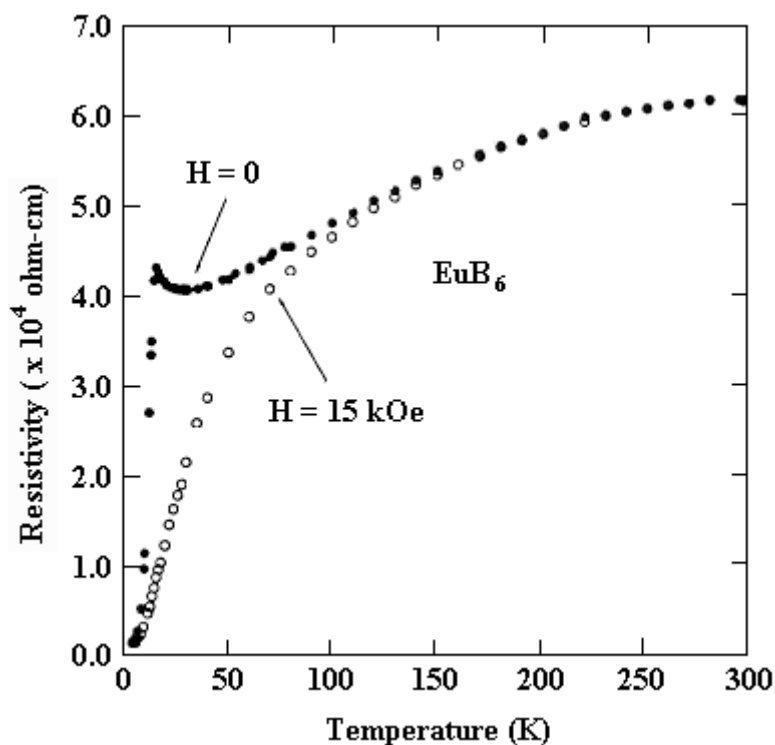


Figure 1-3. Resistivity versus temperature in EuB₆. Closed circles represent zero-field data, while the open circles correspond to a 15 kOe applied magnetic field [25].

Examination of resistivity versus temperature in EuB₆ reveals a sharp maximum followed by a dramatic decline below 16 K [24,25], as shown in Figure 1-3. Since Eu exists in a +2 valence state in this compound, semiconducting behavior was expected. The large drop in resistivity with decreasing temperature was interpreted to indicate semi-

metallic behavior instead and was attributed to a reduction in magnetic scattering upon moment alignment. Negative magneto-resistance corroborates this picture [26,27], as shown in Figure 1-4.

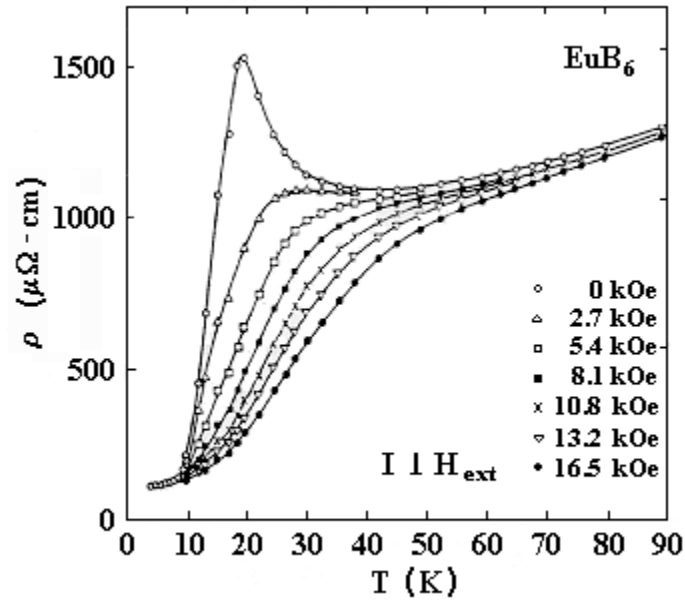


Figure 1-4. Resistivity versus temperature in EuB_6 at various magnetic fields. At low temperatures, the magneto-resistance is clearly negative [26].

Further studies of the magnetic transition in EuB_6 demonstrated that there exist two critical points associated with the onset of ferromagnetic order [28-30], one occurring at 15.1 K and the other at 12.6 K. Figure 1-5 shows that these two transitions appear as sharp peaks in the quantity $d\rho/dT$ as a function of temperature. Subsequent work has attempted to differentiate between the origins of the two transitions. Accompanying this work [28] is a series of Arrott plots of magnetization versus magnetic field for various temperatures. These curves indicate that EuB_6 is ferromagnetic, i.e. exhibits a positive value of magnetization at zero magnetic field, up to a temperature

between 11 and 13 K. These workers assert that the lower transition represents the onset of ferromagnetic order.

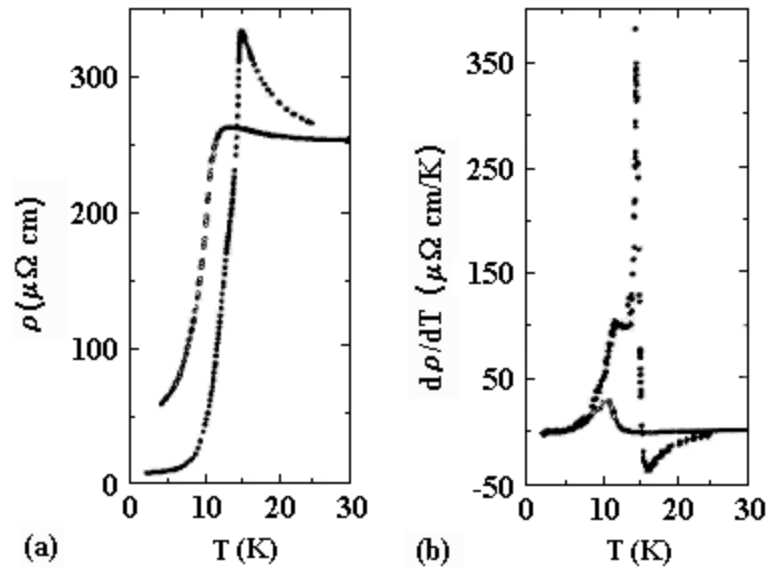


Figure 1-5. Resistivity in (a) and $d\rho/dT$ in (b) versus temperature in EuB₆ [28].

Initially, researchers considered the ferromagnetic order appearing in EuB₆ to be governed by the RKKY interactions that are responsible for the antiferromagnetism seen in most of the magnetic rare earth compounds. Raman spectroscopy studies, however, reveal evidence for the presence of magnetic polarons [31]. Peaks in the Raman spectra for EuB₆ appear to occur at characteristic magnon energy scales and are only evident at temperatures below T_C . Attempts to differentiate the environments corresponding to the two transitions by way of optical measurements have not yet been conclusive.

A picture that has been proposed to describe the onset of long-range ferromagnetism is one of magnetic percolation, in which the polarons grow in size or in number as the temperature is lowered and eventually coalesce into a uniform ferromagnetic state. Electrons in the polaronic state feel a considerable drag due to their interaction with the nearby magnetic moments, an effect that may explain the local

minimum of the resistivity just above T_C . As the fully ferromagnetic state evolves, the moments become aligned, so that the effective masses of the conduction electrons are drastically reduced. The absence of these polarons in the fully magnetic state serves to explain the large resistive drop below T_C discussed above.

1.2 Doping Studies of the Hexaborides

The physical properties exhibited by the hexaborides were found to be very sensitive to electron concentration, prompting a series of doping studies to induce electronic and magnetic transitions in these compounds. For example, by substituting a trivalent cation for a divalent cation, the metal-insulator transition becomes accessible. Furthermore, the dependence of the magnetic interactions on carrier concentration can be probed by substitutionally doping the magnetic hexaborides with cations of dissimilar size. Descriptions of C-doped EuB_6 , La- and Yb-doped SmB_6 , and the Ce- and Th-doped CaB_6 relatives of $\text{Ca}_{1-\delta}\text{La}_\delta\text{B}_6$ are given below.

1.2.1 Carbon Doping of EuB_6

The ferromagnetism exhibited by EuB_6 is unique among rare earth hexaborides. For this reason, many studies of this compound have focused on determining the mechanism behind its ferromagnetism and how it differs from that responsible for the antiferromagnetism typically seen in the rare earth hexaborides.

In initial efforts, carbon doping of EuB_6 has been found to suppress its ferromagnetism [32,33] and is therefore a technique that is used to facilitate the aforementioned investigation. Carbon is incorporated into EuB_6 as a boron substitution and acts as a single electron donor. The radius of carbon is smaller than that of boron so

that, with increasing carbon concentration, the lattice parameter of the compound decreases. This doping results in two transitions, one magnetic and one electronic.

A ferromagnet to antiferromagnet transition occurs with increasing carbon concentration, a progression that may be equivalent to introducing a smaller cation with increased valency. Results show a change in sign of the paramagnetic Curie temperature, θ_p , as the doping level is increased from $x=0$ to $x=0.21$ [32]. Further investigations have yielded information about the intermediate doping regime in which the transition takes place. Neutron diffraction data suggest the coexistence of the low-doping ferromagnetic phase and a high-doping helimagnetic phase, a spiral structure that can be formed through antiferromagnetic interactions [34].

Measurements of resistivity as a function of doping concentration reveal a reduction in resistivity with increased carbon content, consistent with the addition of electrons to the conduction band, which seems to dominate over any decrease in mean free path accompanying the reduction in lattice constant. The correlation between enhanced carrier concentration and the suppressed onset of ferromagnetism and eventual antiferromagnetic order indicates that the higher density of conduction electrons promotes antiferromagnetic order, as seen in the trivalent rare earth hexaborides. These observations are supportive of an RKKY-mediated ordering.

The suggested competition between the addition of charge carriers and the ferromagnetic state is also consistent with the polaronic mechanism for ferromagnetism advocated by Nyhus et al [31]. High carrier concentrations increase electronic screening and tend to inhibit magnetic polaron formation, which would similarly suppress the ferromagnetism characteristic of stoichiometric EuB_6 .

1.2.2 Lanthanum and Ytterbium Doping of SmB₆

The mixed valence state of SmB₆ has been a major subject of study since the early 1980s, when valence fluctuating systems garnered a great deal of attention within the condensed matter physics community. The coexistence of trivalent and divalent cations in a single material inspired a series of doping studies to investigate the metal-insulator transition. La and Yb were good candidates for these doping studies due to their similar ionic size to Sm and their valence states corresponding to the metallic +3 state in LaB₆ and the semiconducting +2 state in YbB₆.

Kasaya et al. [35] incorporated La into polycrystalline SmB₆ using a float-zone technique of crystal growth. The donor was added in varying concentrations from undoped to 50%. Semiconducting behavior is preserved with low doping, but the resistivity value at which the low-temperature flattening sets in is reduced with increasing La concentration. Between the doping levels of 10% and 25%, a change in behavior from semiconducting to metallic is observed.

The Hall coefficient was also measured as a function of doping level and temperature. In the absence of any dopant, the carrier concentration is low, hole-like at high temperatures, and depends significantly on changes in temperature. As the electron concentration is increased, the effect of temperature on carrier density is reduced. At even higher carrier concentrations, where the transition in resistivity occurs, the Hall coefficient changes sign to indicate the dominant carriers are, in this regime, electrons. The data become nearly independent of temperature, and the behavior of the material is interpreted to be metallic.

The results of Kasaya et al. also include studies of Yb-doped SmB₆. These workers discovered that the float-zone growth technique is inadequate for the

incorporation of Yb. For this reason, an arc melting method was used. The range of doping spans the entire range between the parent SmB_6 and stoichiometric YbB_6 .

The resistivity versus temperature curves for each doping concentration indicate the preservation of semiconducting behavior. The carrier concentration, as determined from the Hall effect, changes sign with temperature for an Yb doping level of up to 50%. The changes in carrier sign with temperature for a single sample of lightly doped SmB_6 seem to indicate that a two-band system may be responsible for the transport properties observed. The change in charge carriers from hole-like to electron-like behavior suggests that there are similar numbers of each type of carrier. Under this condition, the dominant carrier type can be holes for one temperature range and electrons for another.

At higher Yb concentrations, the carriers become increasingly electron-like. This trend indicates that, in this regime, Sm can be considered an impurity in an YbB_6 lattice. The enhancement of the electron concentration may be attributed to the evolution of a dominant +3 valence for the Sm species at these high doping levels.

1.2.3 Cerium and Thorium Doping of CaB_6

When employing as dopants cations that produce valence-fluctuating hexaborides, such as Sm and Ce, there is the possibility of a single valence state developing at low concentrations. Young [36] conducted an investigation into this question in which CaB_6 served as a divalent host matrix doped with first Sm, which indicated the dominance of Sm^{3+} at low doping, and then with Ce to further investigate anomalous magnetic properties demonstrated by the Sm series. Although the non-magnetic state of Ce is tetravalent, where all electrons are paired and there is consequently no local moment, it is similar to Sm in that both Ce and Sm have a magnetic state that is trivalent. These investigators explored the presence of a magnetic moment accompanied by metallic

behavior, which would indicate that the Ce cations exist in a trivalent state at dilute concentrations.

Resistivity versus temperature as a function of doping level for Ce concentrations of 0.1%, 0.25%, 0.5%, and 0.75% reveals that metallic behavior appears to correlate with the addition of low levels of Ce doping levels. In addition, measurements of magnetization versus magnetic field yield an unexpected hysteretic behavior. This hysteresis is clear evidence for ferromagnetic order. The assumption that the f-type moments originating from the Ce are responsible for the ferromagnetism conflicts significantly with the RKKY interaction thought to mediate antiferromagnetism in the magnetically dilute regime associated with these observations.

Efforts to simplify the problem and explore the role played by the 4-f Ce moments prompted Young to fabricate La-doped CaB_6 single crystals. The addition of La preserved the trivalent valence state while excluding the magnetic nature of the Ce. An exceptional result was found. In the presence of small La concentrations, ferromagnetic hysteresis in magnetization versus magnetic field was discovered in CaB_6 [37].

The saturation magnetic moment was found to be a maximum value of $0.07 \mu_{\text{B}}/\text{La}$ ion at a doping level of 0.5% and was additionally found to persist to 600 K. These data will be presented in chapter 2. Important evidence in support of the intrinsic nature of this ferromagnetism was obtained by subsequent Th-doping studies. If the addition of one electron per dopant ion gives rise to long-range order, what is the effect of doping with a tetravalent element, thus adding two electrons per dopant ion? The results are consistent with those seen in $\text{Ca}_{1-\delta}\text{La}_\delta\text{B}_6$. The maximum saturation magnetization occurs

at a Th level of 0.25%. This value is half the doping concentration but corresponds to the same electronic content required in the La doping studies.

The discovery of ferromagnetism in $\text{Ca}_{1-\delta}\text{La}_\delta\text{B}_6$ directly inspired the work presented in this dissertation.

CHAPTER 2 PREVIOUS WORK IN CaB_6 AND RELATED COMPOUNDS

The occurrence of ferromagnetism in CaB_6 has no true predecessor, that is, a material composed of non-magnetic constituents that exhibits ferromagnetic order. Section 2.1 includes a review of electron tunneling results for EuB_6 , the only other ferromagnetic hexaboride to date, which may prove helpful in determining the origin of certain features that appear in CaB_6 data.

Section 2.2 will focus on recent data obtained for CaB_6 and SrB_6 , which possess very similar electronic and crystal structures. In fact, some workers have recently inferred the existence of ferromagnetism within the SrB_6 compound because of its similarity to CaB_6 .

2.1 Electron Tunneling Spectroscopy in EuB_6

Electron tunneling spectroscopy is a method by which the electronic density of states of a material can be qualitatively measured. Features appearing in the tunneling spectrum of a compound can provide information on how the states evolve with changes in the external environment, examples of which are temperature variations and the application of a magnetic field. Features important to the understanding of the electronic structure in the material can be resolved, including gap structures, evidence for the presence of magnons, and substantiation for the presence of other inelastic excitations. A more in-depth discussion of tunneling is given in chapter 3.

Specific to EuB_6 is the tunneling spectrum shown in Figure 2-1 [18]. The counter-electrode used in these tunneling studies was Pb, and the I-V characteristic of this

junction clearly features a superconducting gap at temperatures sufficiently below 7.2 K (not shown). The appearance of this gap structure indicates that tunneling is the dominant conduction path through the barrier, as will be described more fully in chapter 3. At temperatures above and near the ferromagnetic ordering temperature, a density of states spectrum qualitatively common to the hexaboride class of compounds is seen. The slope of the spectrum at higher bias voltage is characteristic of the nature of the barrier and is not a property of the electrode.

At 43 meV, the density of states appears to be constant with temperature. Below this bias voltage, there is a depletion in the density of states that becomes more pronounced with decreasing temperature, while the missing states reappear at higher bias. This indicates the formation of a pseudo-gap with an associated energy of 43 meV. It is termed a pseudo-gap because the density of states tends to zero as a power law, as opposed to an exponential, with temperature. Many hexaborides exhibit a similar pseudo-gap on an energy scale specific to the material. The origin of the depletion in the density of states may be a Jahn-Teller-like lattice distortion [18,38].

As the compound orders ferromagnetically, the tunneling conductance increases, indicating an enhanced metallicity. These changes in the spectra are in excellent agreement with the significant reduction in resistivity as the temperature is reduced through the transition temperature of 16 K. In addition, an unusual group of peaks appears about zero bias. While similar peaks are seen in other tunnel junctions featuring a ferromagnet as the electrode of interest, their appearance can be a result of any collective inelastic mechanism present in the electrode. These structures are commonly referred to as zero bias anomalies. Owing to the appearance of the zero bias peaks being concurrent with magnetic ordering, it is believed, though not universally accepted, that

these features may be a signature of ferromagnetism. A more detailed discussion of zero bias anomalies is given in chapter 3, while comparison of this data to the results of this work is presented in chapter 5.

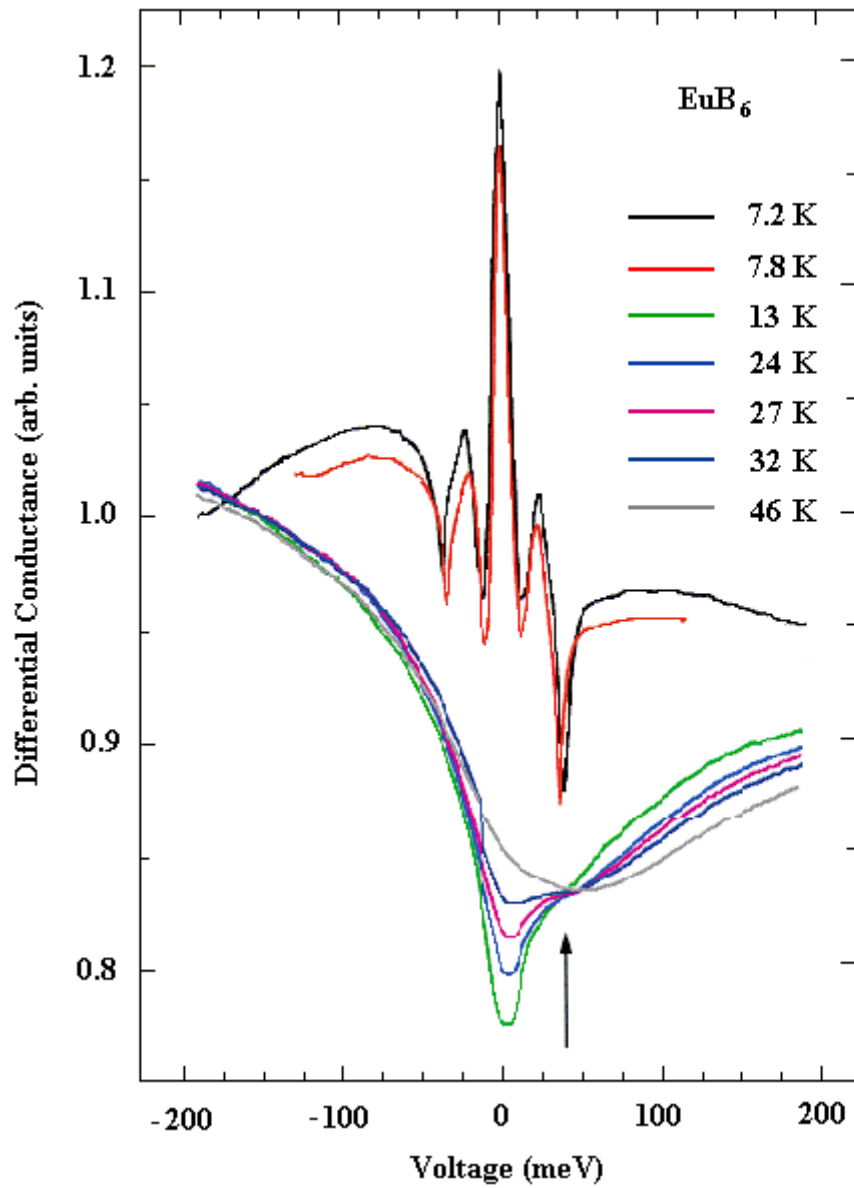


Figure 2-1. Tunneling conductance versus bias voltage in EuB_6 [18].

2.2 Recent Experimental and Theoretical Results in CaB₆ and SrB₆

In this section, a collection of results obtained for SrB₆ and CaB₆ are provided. Comparison of CaB₆ to SrB₆ reveals that the compounds are isovalent and similar in bond lengths. Following the discovery of ferromagnetism in CaB₆ [37], long-range order was inferred to exist in SrB₆ [39]. As a result, experimental data and theoretical results for both materials are compiled here.

2.2.1 Theoretical Studies

Since the discovery of novel ferromagnetism in lightly electron-doped CaB₆, there has been a surge of experimental and theoretical work that forms the basis of current knowledge pertaining to this system. Theoretical efforts have been undertaken by a number of workers. While there are a few avenues that have been pursued in attempting to describe the ferromagnetism, special attention has been given to an excitonic insulator picture. The theoretical foundation of the excitonic insulator model was published nearly simultaneously in 1965 by two independent efforts: Keldysh and Kopaev [40] and des Cloizeaux [41]. The model has been recently revived in applications to CaB₆ and the closely related compound SrB₆.

Initial theoretical efforts focused on a prediction made by Bloch in 1929 [42], in which a polarized electron fluid forms at electron densities between the upper limit of a free electron gas and the lower limit of an insulating Wigner crystal. This intermediate state occurs for a particular range of carrier concentrations, where electron exchange interactions are dominant over Coulomb interactions, the bounds of which have been calculated by several workers [43-46] with a large variation in results. There are two characteristics of the system under scrutiny that appear to be fatal to the success of this theory in application to CaB₆. The first is that the electron densities at which

ferromagnetism appears are rather high with respect to the calculated values. In addition, the polarized electron fluid is treated for one type of carrier, and the transport properties of the divalent hexaborides are generally governed by a combination of electrons and holes. Because of these pathologies, the intermediate density polarized electron fluid was somewhat neglected in favor of the excitonic insulator [47-52].

An excitonic insulator is theorized to form in compensated semimetals where Coulomb interactions are significant in the absence of substantial screening. The band structure corresponding to such a semimetal is illustrated in Figure 2-2 (a). The symmetry between the electron and hole bands makes possible a pairing of electrons and holes in the same k-state. These excitons are bosonic in nature and form what is known as an excitonic condensate. The energy required to form an electron-hole pair is reflected in the formation of a small energy gap in the band structure, at the middle of which lies the Fermi level, as shown in Figure 2-2 (b). This band structure defines the excitonic insulator.

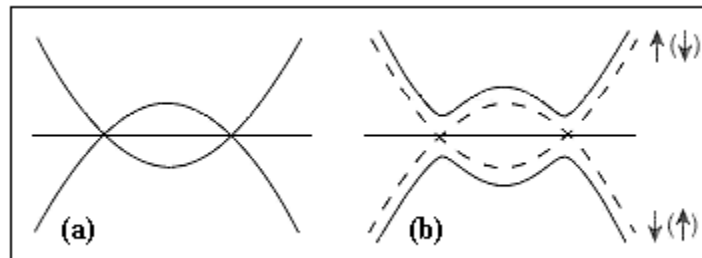


Figure 2-2. The evolution of a semimetallic band structure with excitonic ordering:
 (a) Band structure for a compensated semi-metal.
 (b) Band structure upon formation of an excitonic insulator, where the Fermi level lies at mid-gap [47].

There are degenerate singlet and triplet states that correspond to a charge density wave (CDW) and a spin density wave (SDW), respectively. This degeneracy can be

lifted in two ways. In the event that electron-phonon interactions are important, the CDW state lies lower in energy and implies that charge is the relevant degree of freedom in the system. Conversely, short-range coulomb interactions can dominate, forming a spin-modulated state. The latter possibility is thought to be the ground state of the excitonic insulator in the hexaboride materials, owing to the long mean free paths and low defect content of these compounds.

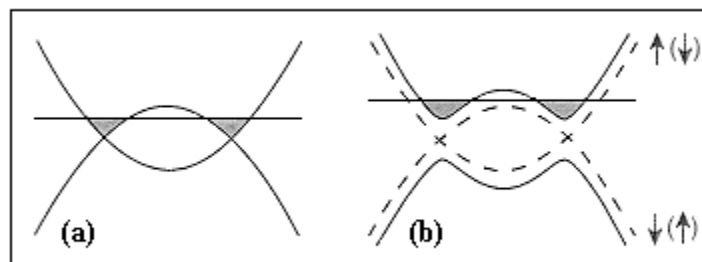


Figure 2-3. The band structure of an excitonic system with electron doping:
 (a) Semi-metallic band structure in the absence of excitonic condensation.
 (b) Band structure showing the excitonic gap for one spin species [47].

The semiconductivity originally observed in CaB_6 in the absence of La has been thought to correspond to the insulating state described above. When carriers are then added to the system, the excitonic condensate becomes slightly unstable. For low doping concentrations, the electron-hole pairing can be maintained by reducing the insulating gap. Additionally, the lowest energy state for the excitonic condensate occurs when all added carriers are placed into one spin band. The cost in energy of accepting electrons unpaired with holes into the system is compensated by a reduction in the excitonic gap for that spin species. The position of the Fermi level is correspondingly raised in the process of doping, and same-spin electrons are responsible for conduction within the doped triplet excitonic insulator. This is shown in Figure 2-3 (a), which shows the band

structure for the doped system in the absence of excitonic order, and (b), which shows the band splitting for one spin species in the presence of excitonic order [47].

There is only a narrow doping range in which the excitonic state is stable, which is shown to be in agreement with experimental results by Young et al., presented below. Specific to CaB_6 , it is not established that the valence and conduction bands are sufficiently symmetric to each other to enable excitonic condensation. It is also not clear whether CaB_6 is a fully or partially compensated semimetal or a direct band-gap semiconductor. The prediction of this dissertation is given in chapter 6.

An experimental signature of excitonic condensation of this type can be seen in far infrared (FIR) spectroscopy. In the purely insulating regime, there should occur one minimum in the reflectivity, denoting a gap that is of equal value for the spin-up and spin-down bands. If asymmetry is introduced into the valence and conduction bands with respect to each other, or if the system is driven from full compensation, as with doping, for example, the gap values will become different for the two spin species. In this case, two minima in the optical conductivity are expected to appear, which represent the energy gaps for each spin species. These FIR studies have been performed by experimental workers and are outlined below.

In addition to the excitonic insulator model, other theoretical proposals have been made. In an argument made by Hirsch [53], the minima of two sub-bands, possibly identifiable with opposite spin species, lie at the same energy, but the curvatures are different. The theory relies on a broadening of one spin band with respect to the other upon ordering. This loss of kinetic energy, Hirsch has argued, drives the ferromagnetism, and because of the difference in curvatures of the two spin bands, one becomes a majority

band and the other a minority band at the Fermi level through differences in effective mass.

Jarlborg has advanced a theory that gives a spontaneous paramagnetic splitting of the conduction band [54]. The Stoner model includes a criterion typically used to predict the occurrence of magnetic order and compares the relative magnitudes of the electronic kinetic energy to the potential produced by the static ions and felt by the conduction electrons. In the limit that the potential energy dominates, the system favors magnetic order. Correction terms to the Stoner model can arise from potential energy gains upon ordering. The potential energy supplements and enhances the exchange energy that exists between electrons. Including this effect can produce a paramagnetic splitting and subsequent spin polarization.

The most recent band structure calculations [46] solve Dyson's equation for the self-energy operator in terms of the Green's function, G , taking into account the dynamical Coulomb interaction, W . This method is called a GW calculation. The resultant band structure features a rather large energy gap of roughly 0.8 eV at the Fermi level, a finding that is contrary to the results of Massidda et al, as discussed in chapter 1. This result, however, seems to agree well with angle-resolved photoemission spectroscopy data to be mentioned in the following subsection. The formation of a band gap is also consistent with the results of this work, to be presented in chapter 5.

The theoretical results outlined above seem to be variations on a general model. All predictions can be interpreted to indicate a spin-split conduction band separated from the valence band by a finite energy gap. The possible appearance of this spin splitting will be revisited in the interpretation portion of this work.

A recent theoretical result proposed recently by Monnier and Delley [55] investigates a possible off-stoichiometry effect in which the single crystals contain boron vacancies. These workers have performed calculations within the local density approximation (LDA) of density functional theory (DFT) to produce theoretical values of the formation energy and magnetic moment associated with plausible types of defect. The defects studied include various substitutions of La and Al (from the flux growth technique of Young et al.) for Ca and B₆, interchange of Ca and B₆, and Ca, B, and B₆ vacancies. Their findings imply the presence of a magnetic moment associated with B₆ vacancies and Ca substitutions on B₆ sites. Ca substitution for B₆ is predicted to produce a moment roughly half the size of that associated with a B₆ vacancy. It was also predicted that the substitution of La or Al for B₆ quenches the moment, an observation that is consistent with a decrease in magnetic moment with La doping at concentrations above 0.5% [37], as is described below.

Monnier and Delley suggest that the most likely source of B₆ vacancies is the [100] set of crystal surfaces, since the cleaving process of single crystal hexaboride surfaces occurs through severing of inter-octahedral bonds at the surface. This region appears to be a good approximation to the B₆ vacancy density corresponding to the experimentally determined magnitudes of magnetic moment. The viability of this argument will be related to the results of this work in chapter 6.

2.2.2 Experimental Studies

The experimental investigations that have been performed to date on the CaB₆-like divalent hexaborides have produced a multitude of unclear results. Contradictory effects are seen, and even the compositions of samples are often ambiguous, as a result of disagreeing behaviors between crystals that are labeled by the same stoichiometry. For

these reasons, care must be taken in the interpretations applied to the results outlined below.

The discovery of ferromagnetism in La-doped CaB_6 arose out of analogous studies by Young [36] using Ce as a dopant, as described in chapter 1. In an attempt to simplify the compound and understand the effect of a trivalent, non-magnetic dopant on the CaB_6 system, single crystals of $\text{Ca}_{1-\delta}\text{La}_\delta\text{B}_6$ were grown. Surprisingly, a small magnetic moment of $0.07 \mu_B/\text{La}$ ion was discovered [37].

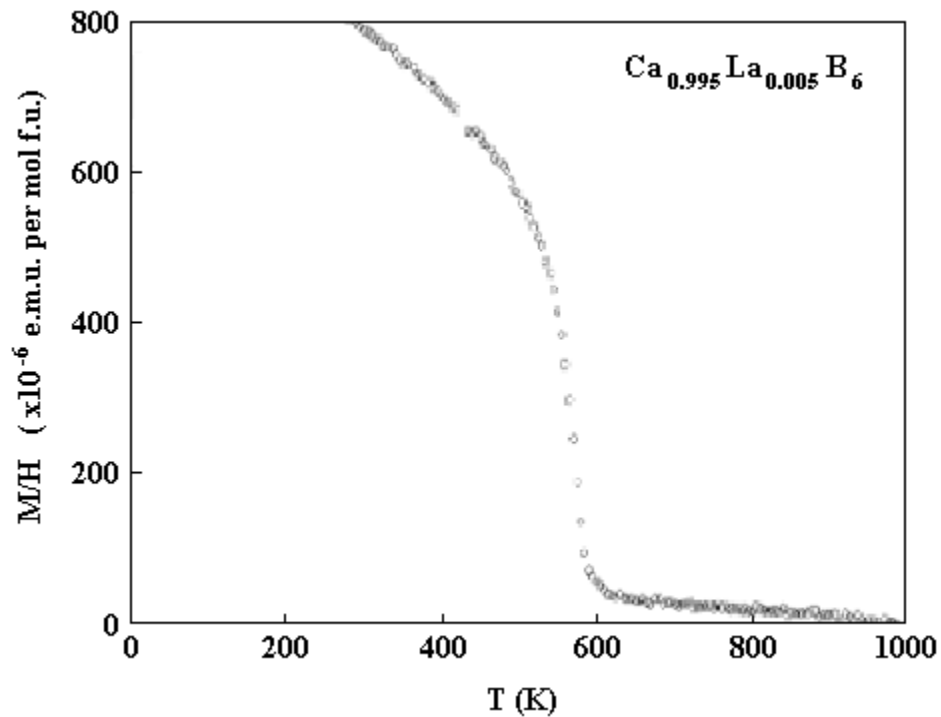


Figure 2-4. Magnetization versus temperature in $\text{Ca}_{0.995}\text{La}_{0.005}\text{B}_6$ showing a T_C of approximately 600 K [37].

Figure 2-4 shows the preservation of a finite magnetization in this material to a temperature of at least 600 K, a T_C that is astounding in its own right because of the extremely small moment. Recent workers have quoted the T_C to occur as high as 900 K. With variations in δ , it was found that there exists a narrow region in doping

concentration above which the ferromagnetism disappears. This is shown in Figure 2-5, where the saturation magnetization reaches a maximum at a nominal doping level of 0.5%.

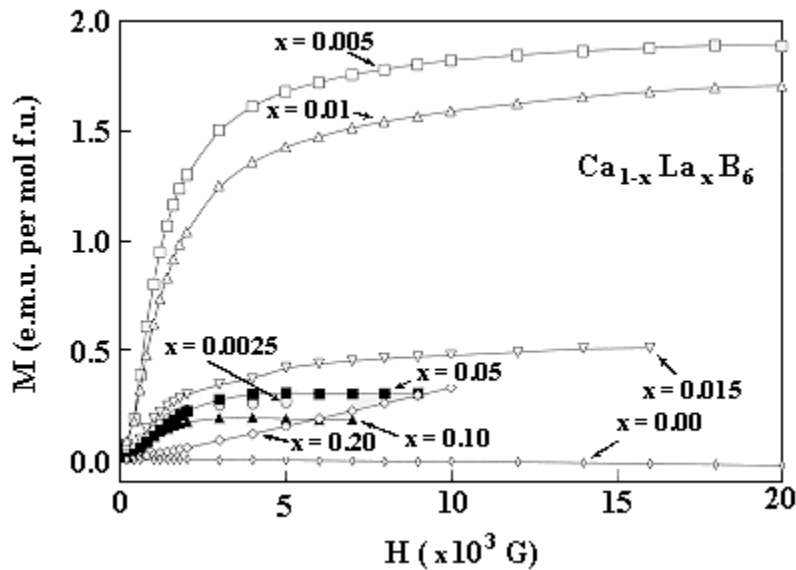


Figure 2-5. Magnetization versus magnetic field at various La doping concentrations. The maximum signal is observed for 0.5% La content [37].

Since CaB_6 is expected to be an intrinsic semiconductor or fully compensated semimetal, an attempt was made to prepare a hole-doped analog of the electron-doped ferromagnet. To discover ferromagnetism in the hole-doped material would establish electron-hole symmetry. An attempt to fabricate hole-doped crystals was carried out by using a self-doping technique. Ca vacancies were purposefully introduced, with the intention that the vacant Ca site would act as an electron acceptor. It was subsequently found that a hole-doped analog is not achieved by depleting the Ca content of the crystal, and interpretations of this result indicate that no ferromagnetism is observed in the Ca-deficient compound. This assertion is not universally accepted, but Hall effect studies that corroborate this conclusion are presented in chapter 5.

Transport and optical studies were undertaken to investigate the possible appearance of evidence for the excitonic insulator picture [56,57]. The single crystals of these studies were grown under the same conditions as those of Young's work, namely by Z. Fisk's group, as were the samples studied for the purposes of this dissertation. According to these workers, the samples called $\text{Ca}_{1+\delta}\text{B}_6$ are thought to be stoichiometric, and the crystals labeled CaB_6 are thought to be hole-doped. Measurements of resistivity, shown in Figure 2-6, asserted that stoichiometric CaB_6 is semiconducting. The La-doped and Ca-deficient compounds were proclaimed to be metallic, due to assumptions that the Ca deficiency corresponds to hole doping. It should be emphasized that the transport results to be presented in chapter 5 disagree with these conclusions for the stoichiometric and Ca-deficient compounds, specifically in that the transport properties of the crystals seem to be interchanged.

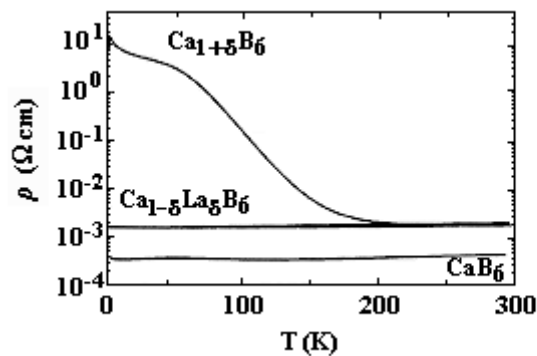


Figure 2-6. Resistivity versus temperature in the electron-doped $\text{Ca}_{1-\delta}\text{La}_\delta\text{B}_6$, Ca-deficient CaB_6 (to be denoted $\text{Ca}_{1-\delta}\text{B}_6$), and stoichiometric $\text{Ca}_{1+\delta}\text{B}_6$ [57]. Note that these identifications conflict with the results of our work for the stoichiometric and Ca-deficient samples.

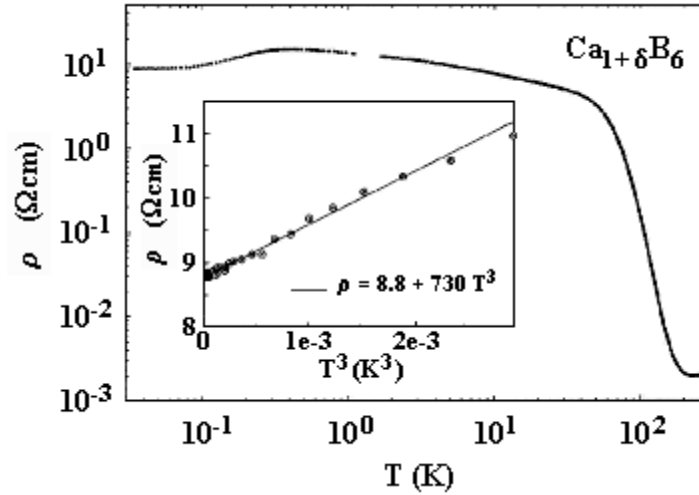


Figure 2-7. Resistivity versus temperature in $\text{Ca}_{1+\delta}\text{B}_6$. The log-log scale emphasizes the low-temperature decrease in resistivity at roughly 0.2 K. The inset shows a fit to T^3 at the lowest temperatures [57].

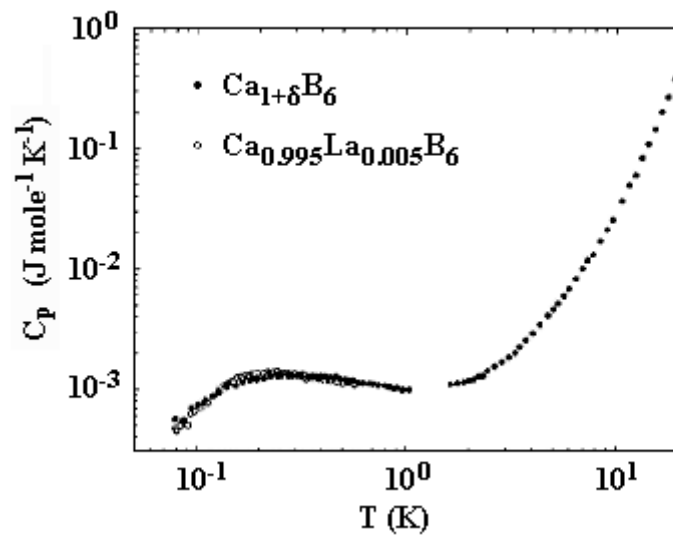


Figure 2-8. Specific heat versus temperature in $\text{Ca}_{1+\delta}\text{B}_6$ and $\text{Ca}_{0.995}\text{La}_{0.005}\text{B}_6$. Note the local maximum at roughly 0.2 K [57].

Low temperature resistivity measurements by Vonlanthen et al. of the semiconducting material show a slight decrease with decreasing temperature below a few tenths of Kelvin. This is shown in Figure 2-7, the inset of which emphasizes a T^3 dependence of low-temperature resistivity. When compared to specific heat versus

temperature data in the same temperature range, a concurrent local maximum is observed, as shown in Figure 2-8. Similar behavior of these quantities has been observed in SrB_6 [56].

Gavilano et al. performed ^{11}B nuclear magnetic resonance studies (NMR) to measure the spin-lattice relaxation rates in SrB_6 and $\text{Ca}_{1-\delta}\text{La}_\delta\text{B}_6$ [58]. The results were compared to NMR spectra in LaB_6 . The workers discovered no discernable difference in the spin echo intensity of all three materials at low temperatures. It is therefore apparent that the drastically different resistivities, and in turn, the electron densities, have no direct relation to the rate of spin relaxation. Furthermore, it was noted that the intensities are too large to be accounted for by itinerant electrons alone.

The relaxation rates for SrB_6 at various magnetic fields are plotted versus temperature in Figure 2-9. The field dependence of T_1^{-1} was found to be of the form $1/H$ (not explicitly shown). Data for LaB_6 at $H=0$ are shown as a constant-slope solid black line for comparison and exhibit a linear dependence on temperature, as is expected for metallic materials. In contrast, SrB_6 demonstrates what may be a linear dependence on temperature below a few Kelvin accompanied by a crossover temperature labeled by T_0 . Above T_0 , the relaxation rate appears to be independent of temperature. The constancy of the relaxation rate suggests that phonons are not the mechanism behind the spin relaxation.

Fits to various relaxation mechanisms, such as localized moments, itinerant magnetic moments, and paramagnetic impurities, were performed and yielded unsatisfactory results. A viable possibility involves scattering of conduction electrons from localized electronic states that only a fraction of the material's electrons occupy. These circumstances would produce a temperature-independent effect and would give a

magnetic field dependence proportional to $1/H$, in agreement with the field dependence of T_0 .

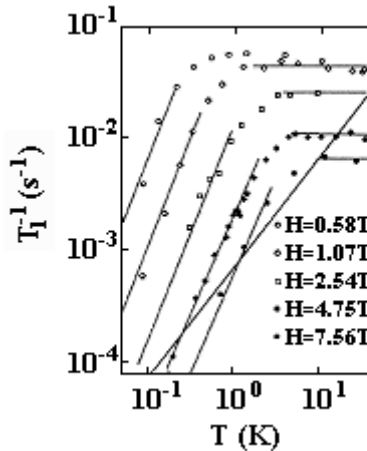


Figure 2-9. Spin relaxation rate versus temperature in SrB_6 at various magnetic fields. The solid black line represents data for LaB_6 at $H = 0$ [58].

The transport and NMR work discussed above indicate a transition below 1 K in CaB_6 and SrB_6 , the exact stoichiometries of which are ambiguous. The transition is accompanied by the activated rise in the resistivity data giving way to a region of decreasing resistivity and enhanced metallicity. In addition, the specific heat in the alkaline earth hexaborides exhibits a local maximum at roughly the same temperature indicating a possible increase of electronic contribution. A transition of the electronic environment to a more metallic state is consistent with these observations. A discouraging detail is the similarity in low-temperature specific heat between the stoichiometric and La-doped materials. The dissimilarity in resistive behaviors at low temperature seems to preclude the association of the specific heat maximum with the reduction in resistance. It is necessary, then, to assert that the specific nature of the transition and final configuration is not clear at this time. The possible appearance of a transition in $\text{Ca}_{1-\delta}\text{La}_\delta\text{B}_6$ will be discussed in later parts of this dissertation.

Work by Vonlanthen et al. presents FIR spectra as a function of La concentration [57]. Results of optical reflectivity versus wavevector are shown in Figure 2-10 and have been related to the excitonic insulator model, since a minimum in the reflectivity spectrum indicates the presence of a gap. In semiconducting CaB_6 , there appear two narrow minima close to each other in energy at frequencies 240 and 275 cm^{-1} . These features are shown in higher resolution in the inset and may imply the presence of gaps for each spin species. Excitonic ordering in a material with a small degree of incomplete nesting of the Fermi surface can produce a similar effect resulting from asymmetry-induced band splitting. The possibility of such asymmetries in the Fermi surface cannot be excluded for this material.

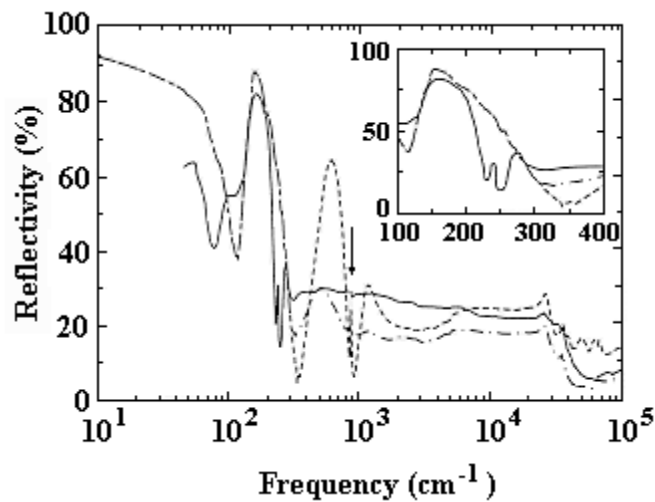


Figure 2-10. Optical reflectivity versus frequency in $\text{Ca}_{0.995}\text{La}_{0.005}\text{B}_6$ (dash), $\text{Ca}_{0.99}\text{La}_{0.01}\text{B}_6$ (dot/dash), and CaB_6 (solid) [57].

Upon examination of the reflectivity in 0.5% La doped CaB_6 , we find two clear minima in the spectrum at higher energies of 700 and 1200 cm^{-1} . With further La doping to a level of 1%, the features broaden considerably but appear to preserve the energy scale set by the 0.5% La-doped material. As the doped excitonic insulator model requires different gap values for the different spin flavors, these minima may be evidence for a

physical manifestation of the model. It is troubling, however, that these features are very far from the energy scale of the undoped material. This large shift in energy is not predicted to accompany slight doping of an excitonic insulator.

The results of band structure calculations by Massidda et al. that predict an overlap between the conduction and valence bands and form the foundation for the excitonic insulator seem to be contrary to the findings of several workers, the results of which indicate a gapped band structure. Among these is angle resolved photoemission spectroscopy data [59] that provides evidence for a band gap of the order of 1 eV. The ARPES technique is a direct probe of the band structure, which is shown for CaB_6 in Figure 2-11. The band structure in solid black represents the calculations performed by Tromp et al. that are in good agreement with the experimental findings. It is worthwhile to note that the valence band image differs significantly from the doubly peaked band that is predicted for an excitonic insulator, and the band gap is substantially larger than an excitonic instability is expected to yield.

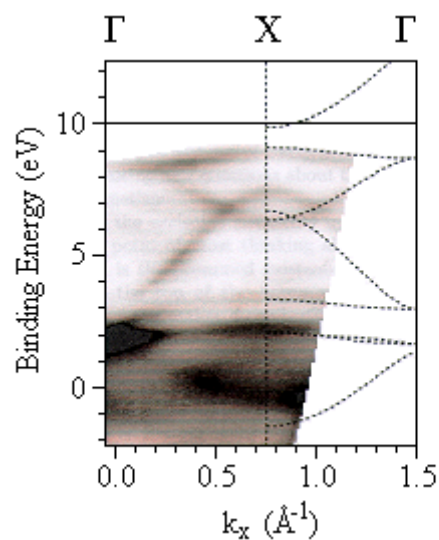


Figure 2-11. Angle resolved photoemission spectra in stoichiometric CaB_6 . The theoretical GW-calculated band structure is shown in the dotted lines [59].

The recent ARPES work is accompanied by techniques more sensitive to bulk properties, soft x-ray emission (SXE) data and partial fluorescence yield (PFY), shown in Figure 2-12. These data show the positions of the valence band maximum (VBM) and Fermi level for selected hexaborides. It is clear from these data that, in CaB_6 and SrB_6 , the VBMs and Fermi levels occur at distinctly different energies, and the Fermi levels intersect a marginally populated region of the band structure. The conclusions are that there appears to be electron density at the Fermi level, and the divalent hexaborides of CaB_6 -type may be semimetallic.

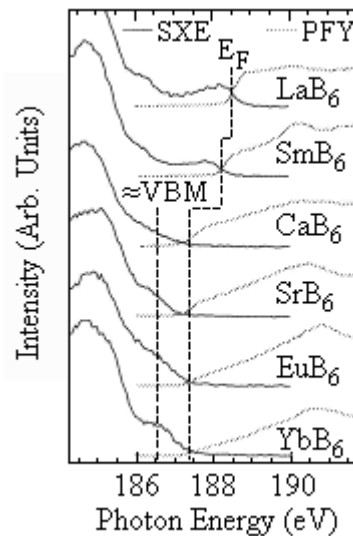


Figure 2-12. SXE and PFY intensities versus photon energy in various hexaborides. Positions in energy of the Fermi level and valence band maximum are shown for each compound [59].

From de Haas-van Alphen measurements of the Fermi surface in SrB_6 , CaB_6 , and $\text{Ca}_{1-\delta}\text{La}_\delta\text{B}_6$, Donovan Hall et al. [60] report the appearance of two pockets in the similar Fermi surfaces of SrB_6 and CaB_6 . There is a higher frequency resonance attributed to an electron pocket, while these workers have identified a dominant lower frequency resonance as a hole pocket with an effective mass five times larger than that of the electron pocket. As electrons are added to the system, to a La doping level of $\delta = 0.0025$,

the low-frequency signal apparently disappears. Further addition to electrons, to a La concentration of $\delta = 0.005$, reveals the appearance of an additional high-frequency resonance, with an effective mass slightly differing from the aforementioned electron pocket. While the association of the lower resonance with hole-like carriers appears straightforward, problems arise when these measurements are compared with those of Denlinger et al., in which the curvature of the bands can be resolved, and no hole component is observed to be present at the Fermi level of SrB_6 . The identification of the low-frequency signal will remain tentative for the purposes of this dissertation.

Electron spin resonance studies undertaken by Kunii provide supportive evidence for anisotropy in the electronic Fermi surface [61]. By rotating a disk-like crystal of 0.5% La-doped CaB_6 with respect to the applied RF and static magnetic fields, the resonance field shifts. In addition, the sharpness of the peak varies with sample orientation. This data is shown in Figure 2-13, where the angle is between the plane of the disk and the direction of the static, or external, magnetic field. It is important to acknowledge that the shape of the sample may produce inherent asymmetries, due to considerations such as demagnetizing factors.

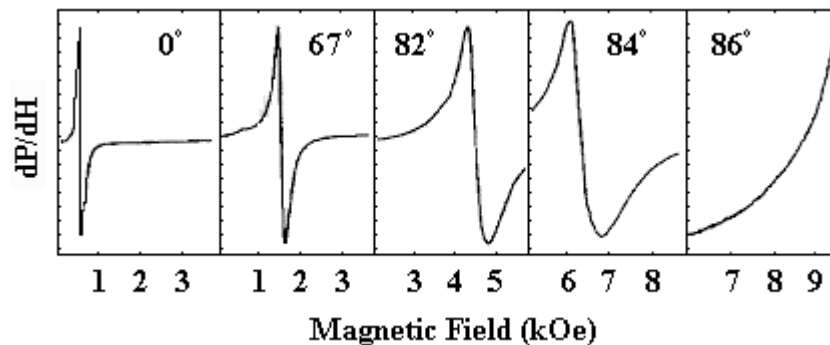


Figure 2-13. Electron Spin Resonance spectra in $\text{Ca}_{0.995}\text{La}_{0.005}\text{B}_6$. The angle is defined to be that between the plane of the disk and the external static magnetic field [61].

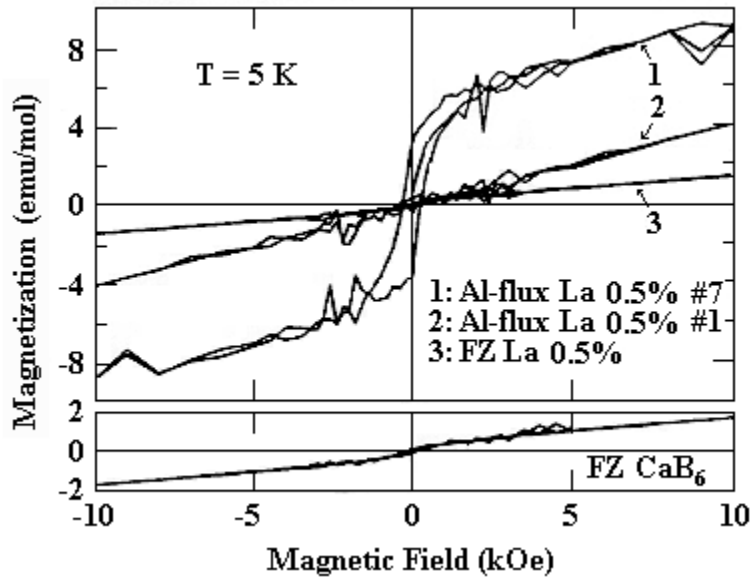


Figure 2-14. Magnetization versus magnetic field in $\text{Ca}_{0.995}\text{La}_{0.005}\text{B}_6$ and CaB_6 grown by FZ and Al-flux techniques [62].

Other workers have recently grown single crystals of electron-doped and stoichiometric CaB_6 by two methods: out of an Al flux, the method used by Young et al., and a floating-zone (FZ) method [62]. Comparisons of crystals grown by the different methods are somewhat conflicting. A ferromagnetic signal was detected in one of the La-doped crystals grown by the Al-flux method, as shown in Figure 2-14 (curve 1). Another of the flux-grown La-doped crystals (curve 2) exhibited no hysteresis but finite magnetization, as did a La-doped crystal grown by FZ (curve 3). Magnetization versus field is also given in the lower plot for stoichiometric CaB_6 grown by FZ as a reference.

Speculating on the origin of these apparently conflicting results, Terashima et al. have suggested the presence of an inhomogeneous ferromagnetic phase, containing magnetic domains separated by paramagnetic regions. These workers point out the possibility that there is a lower critical limit on ferromagnetic domain size required for a material to exhibit hysteresis. For sufficiently small domains, then, the response of the material to an applied magnetic field may be superparamagnetic in nature, a model in

which the magnetization exhibits no hysteresis. These interpretations are consistent with the existing data.

The recent theoretical predictions given by Monnier and Delley [55], discussed above, combined with the magnetic domain structure suggested by Terashima et al. may serve to explain the variation in moment size as a function of growth technique and even among separate attempts of the same technique. The magnetic domains may represent clustering of B_6 vacancies or substitutions so that domain size could account for the reported discrepancies in moment magnitude. This model is discussed relative to our work in chapter 6.

Terashima et al. also performed resistivity measurements on these samples, giving results shown in Figure 2-15 that appear to be uncorrelated with the crystal composition. The crystals grown by FZ are characterized by a high resistivity. Interestingly, the La-doped resistivity extrapolates to a higher value than that of CaB_6 at zero temperature. The Al-flux grown crystals instead show a low and metallic resistivity with an anomalous drop off at low temperatures. This feature was attributed to the superconductivity of Al inclusions, a conclusion supported by the magnetic field induced suppression of the effect.

In response to the contradictory results for the same nominal doping concentrations, Morikawa et al. undertook a systematic study of CaB_6 in an attempt to isolate the effect Ca vacancies have on the electronic properties of the material [63]. The crystals were prepared by reacting CaO with B at various temperatures and at various growth rates and resulted in polycrystalline samples. By manipulating the growth temperature and rate, the workers asserted the ability to control the Ca content of the crystals. The assumption was that a lower growth rate enabled the escape of Ca from the

crystal. The results of the study indicated that there was no correlation between the inferred crystal stoichiometry and the resistivity of the sample.

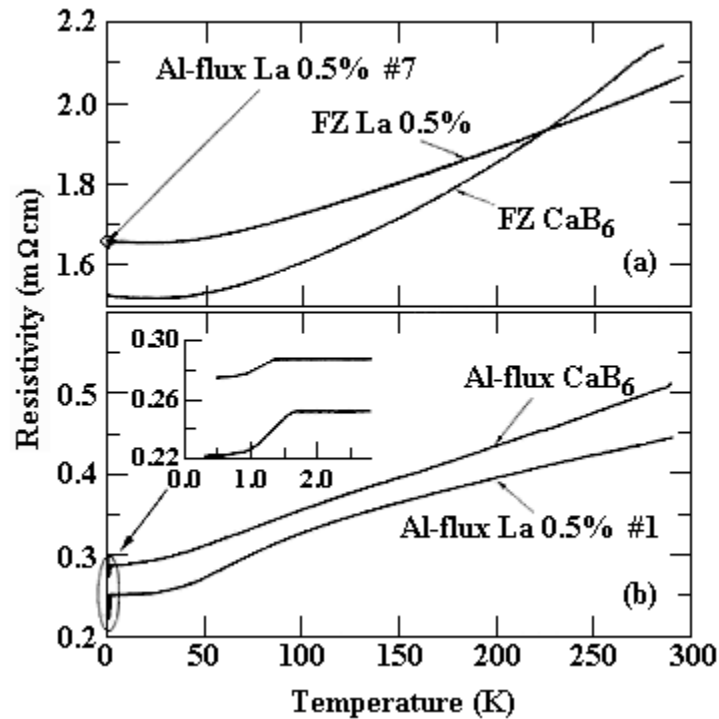


Figure 2-15. Resistivity versus temperature for $\text{Ca}_{0.995}\text{La}_{0.005}\text{B}_6$ and CaB_6
 (a) grown by FZ technique and
 (b) grown by Al-flux technique [62].

Magnetization versus magnetic field data is shown in Figure 2-16, where samples (1) through (4), which were grown at either 1200 °C for 12 hours or at 1500 °C for one hour, are diamagnetic, and (5) through (8), which were grown at 1500 °C for longer times, exhibit ferromagnetism. In Figure 2-17, the magnetization for a ferromagnetic sample (9) and a diamagnetic sample (1) is shown. Comparison with the resistivity versus temperature for diamagnetic samples (2) through (4) and ferromagnetic sample (9) in Figure 2-18 indicates no correspondence between ferromagnetism and metallic or semiconducting behavior. Morikawa et al. therefore assert that ferromagnetism in this

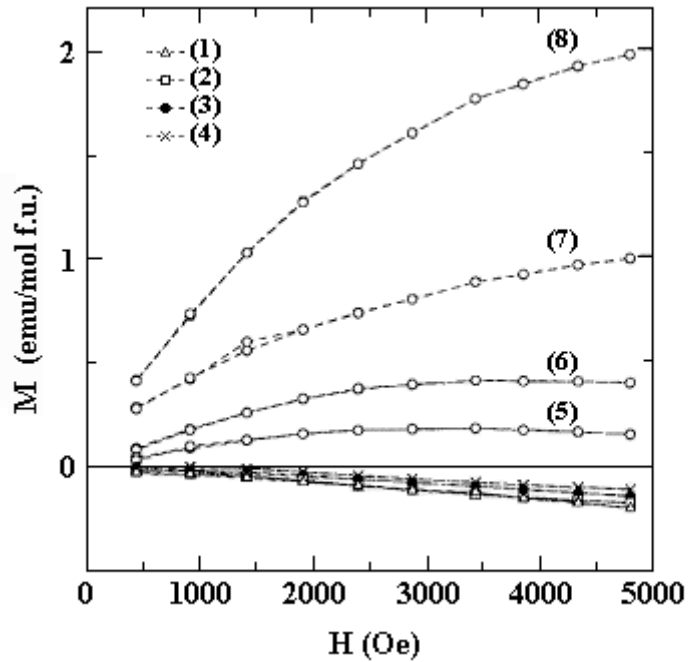


Figure 2-16. Magnetization versus magnetic field for polycrystalline CaB_6 : growth conditions. Diamagnetic samples (1)-(4) were grown at a high rate or low temperature compared to the ferromagnetic samples (5)-(8), grown at a low rate and high temperature [63].

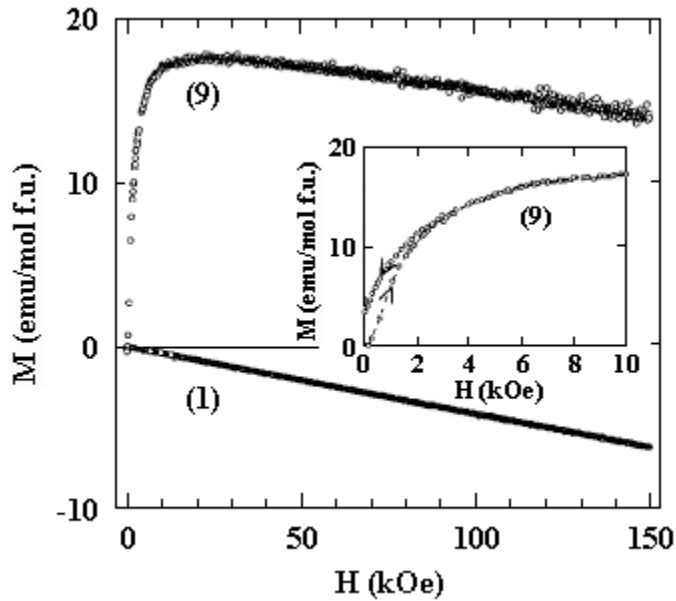


Figure 2-17. Magnetization versus magnetic field in polycrystalline CaB_6 : ferromagnetism and diamagnetism. (1) was synthesized at a $1200\text{ }^\circ\text{C}$ for 12 hours and (9) at $1500\text{ }^\circ\text{C}$ for 6 hours. The inset shows ferromagnetic hysteresis in sample (9) [63].

system is independent of carrier concentration and is instead related to a reduction of symmetry in the crystal.

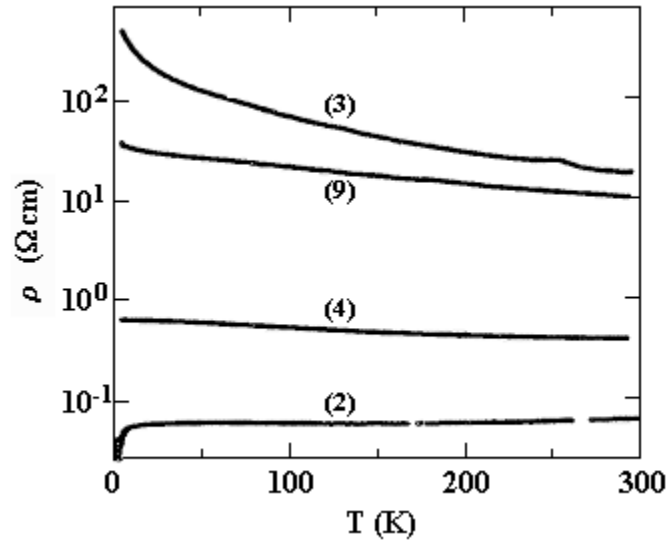


Figure 2-18. Resistivity versus temperature in polycrystalline CaB_6 . Samples (2)-(4) are diamagnetic and sample (9) is ferromagnetic [63].

Another possibility can be derived from the results of Terashima et al. If there are variations in magnetic domain size, then a lower growth rate might be expected to produce larger grains and perhaps larger magnetic domains. This may justify the appearance of ferromagnetism in only samples (5) through (9). More difficult is relating this effect to the electrical resistivity, but the variations in Ca content suggested by these workers is insufficient to account for the wide variations in transport data accompanying this work. For example, it is difficult to see how samples (2), (3) and (4) exhibit such different behaviors, and in particular, why (3) is more resistive than sample (9), if (2) through (4) are nominally stoichiometric. It is apparent that fabricating crystals with stoichiometric precision currently limits coherent progress in the field.

CHAPTER 3 PURPOSE OF EXPERIMENT

To investigate the nature of the ferromagnetism in CaB_6 , a series of electron transport studies were performed on electron-doped, Ca-deficient, and on-stoichiometry CaB_6 . Electron transport measurements are expected to give information about the novel magnetism observed in these compounds for two reasons. The first is that, in the event that there are no local moments native to this material, it is natural to expect the ferromagnetism to be entirely itinerant. In addition, the magnetic properties of the hexaborides are very sensitive to the electronic environment and content. Manipulation of parameters such as doping level and external electric and magnetic fields and the response of the material to these variations should give insight into the mechanism responsible for ferromagnetism. The questions this work has attempted to answer include

- (1) Is CaB_6 semimetallic or semiconducting in accordance with the latest band structure calculations?
- (2) How does the electron transport change in magnetic field and with doping?
- (3) How does the carrier concentration change as a function of temperature and doping level?
- (4) Can ferromagnetism be detected through tunneling techniques?

A number of experimental techniques have been used in the investigation of the CaB_6 system. The combined information that has been obtained through resistivity, magnetoresistance, Hall effect, and electron tunneling measurements has suggested a self-consistent picture of the electronic environment within these compounds, as will be

presented in chapters 5 and 6. This chapter contains a description of the technological motivation for our studies, followed by brief theoretical descriptions of electrical conductivity and electron tunneling microscopy.

3.1 Technological Motivation

The quest to integrate the spin degree of freedom into the semiconductor-based electronics industry is the driving force of the emerging field of spintronics. Through the use of spin-polarized carriers, both the electronic and magnetic responses of semiconductor devices can be exploited.

The materials that are applicable to the field of spintronics must satisfy a number of criteria. The usefulness of a candidate material depends on the degree of electron spin imbalance, the operating temperature relative to T_C , and the ability to effectively transfer spin-polarized current into the materials used in the existing semiconductor-based industry. Future progression of the field of spintronics relies exclusively on the ability to develop a compound satisfying the above requirements.

Spin-polarization of electrons is associated with ferromagnetic materials. The known ferromagnetic metals were employed as the first attempt to inject spin-polarized current into semiconductors. While these ferromagnetic metals have high ordering temperatures and do produce spin-polarized current, they lack the ability to effectively transfer this current to a neighboring semiconductor. The band structures of the two materials differ to such an extent that the wave vector mismatch across the boundary significantly hinders the transmission of current. Efforts now focus on another approach: to develop a ferromagnetic semiconductor.

The applicability of a ferromagnetic semiconductor to the field of spintronics depends on a number of properties. The candidate must display a low carrier concentration, a low spin-flip scattering rate, a way to externally control the degree of spin-polarization, by electric field gating, for example, and ferromagnetism at operating temperatures above 300 K.

Many magnetic semiconductors are now known. Mn doping of III-V semiconductors, such as InMnAs [64], has been the predominant method for inducing ferromagnetism in these materials. The relevant challenge is that of ordering temperature. Applicability necessitates device operation at room temperature, a T_C that has not been historically attainable.

A new candidate system has been developed recently. Recent work by Theodoropoulou et al. indicates that Mn-doped GaN at a nominal doping level of 3 to 5 atomic percent is ferromagnetic with a T_C of approximately 250 K [65]. Theoretical predictions suggest that improved film quality at a Mn concentration of 5 at. % may produce ferromagnetism that persists to room temperature. The ferromagnetic ordering temperature is predicted to be proportional to the band gap of the host semiconductor, and the large gap value for GaN of roughly 3.5 eV is consistent with the prediction of a high T_C with the addition of Mn moments.

The discovery of ferromagnetism in the CaB_6 system has spawned interest in the compound for possible application to spintronics, in light of its high ordering temperature, long mean free path, and the sensitivity of its ferromagnetism to carrier density. With a low enough carrier concentration, CaB_6 thin films may ultimately be industrially applicable.

Electric field gating of magnetic semiconductor thin films is highly desirable, as it provides a way to externally control the magnetism. The gated material essentially forms one of the electrodes of a capacitor. The opposite electrode is metallic. By controlling the voltage across the structure, charge carriers can be drawn into the insulating layer, thus depleting the semiconducting electrode of conduction electrons, a procedure requiring a low carrier density and minimal screening. Since the extent of magnetic order in CaB_6 is highly dependent on carrier concentration, field gating would enable a high-resolution study of the ferromagnetic-non-magnetic transition in CaB_6 .

3.2 Electrical Conductivity in Metals and Semiconductors

One of the simplest ways to probe the electronic properties of a solid is by measuring the motion of electrons under the influence of an applied electric field. The conductivity of a rudimentary metal is given by the Drude formula in Equation 3-1, where σ is the conductivity, n is the electron density, e is the electron charge, m is the electron mass, and τ is the scattering time, a quantity that takes into account finite temperature and scattering processes.

$$\sigma = \frac{n e^2 \tau}{m} \quad (3-1)$$

This expression can be modified to account for realistic band structure effects by replacing m with m^* , the effective mass, and remains approximately correct in the presence of electron-electron correlations.

The inverse of the conductivity is the resistivity, and is commonly measured as a function of temperature for material characterization purposes. Metallic systems exhibit a resistivity that is reduced with decreasing temperature. At high T, the behavior is

typically linear, with a correction term that approaches T^5 at lower T, containing information about electron-phonon scattering, which contributes a T^3 -dependence, and small-angle electron-electron scattering, which contributes a factor of T^2 . At the lowest temperatures, there is insufficient thermal energy to excite phonon modes, and ultimately, the dominant scattering mechanism is that of electron-impurity scattering. In a perfect crystal at zero temperature, the resistivity vanishes.

In contrast, perfect semiconductors exhibit infinite resistivity at zero temperature. At finite temperature, these materials rely on thermal energy to promote valence band electrons across an energy gap into the conduction band. The resistivity in the presence of thermal excitation follows an exponential form as a function of temperature, as in Equation 3-2.

$$\rho(T) = \rho_0 e^{\Delta/kT} \quad (3-2)$$

In the following subsections, the effect of an applied magnetic field on the electron transport in metals and semiconductors will be presented.

3.2.1. Electrons in Applied Magnetic Field I: Magnetoresistance

The magnetoresistance of a material refers to the effect of an applied magnetic field on its electronic transport properties. There are two main configurations commonly used to measure the magnetoresistance: longitudinal, and transverse. In the longitudinal configuration, the current is injected, the magnetic field is applied, and the voltage is recorded along the same crystal direction. In the transverse orientation, the field is applied in a direction perpendicular to that of the parallel current injection and voltage measurement.

A simple metal in which there is one type of carrier and has a perfectly spherical Fermi surface exhibits no change in resistance with applied magnetic field. In this simple metal, an electric field is set up by the charge carriers that is transverse to both the current direction and the magnetic field and perfectly cancels the Lorentz force due to the applied magnetic field. This transverse electric field makes Hall measurements possible, as will be discussed below.

In the presence of anisotropy in the Fermi surface or when more than one type of carrier is responsible for the charge transport, the resistivity of a typical metal will become enhanced when placed in a magnetic field. This phenomenon is known as magnetoresistance, and to first order follows a positive H^2 dependence on magnetic field. This dependence can be easily understood from symmetry arguments in the sense that the magnetoresistance should be symmetric with respect to the sign of the magnetic field. To complicate matters, when dealing with correlated electron systems, there can be significant contributions from other sources.

In many ferromagnets, it is common to observe a reduction in sample resistance with the application of a magnetic field. This occurs due to the alignment of moments along the direction of the field. The state of lower disorder leads to reduced spin-dependent scattering and increases the electronic mean free path, thus reducing resistivity. At the saturation field, the moments are completely aligned, so that no further reduction of the resistivity is attained by the application of additional field. At fields sufficiently above the saturation field, the negative effect becomes overpowered by the standard positive H^2 behavior, and the magnetoresistance turns over and approaches positive values. A relevant example of negative magnetoresistance is exhibited in EuB_6

[66], as shown in Figure 3-1. The negative signal features a saturating effect at the highest fields, implying an eventual turnover. The positive component at low field may be due to magnetic hysteresis.

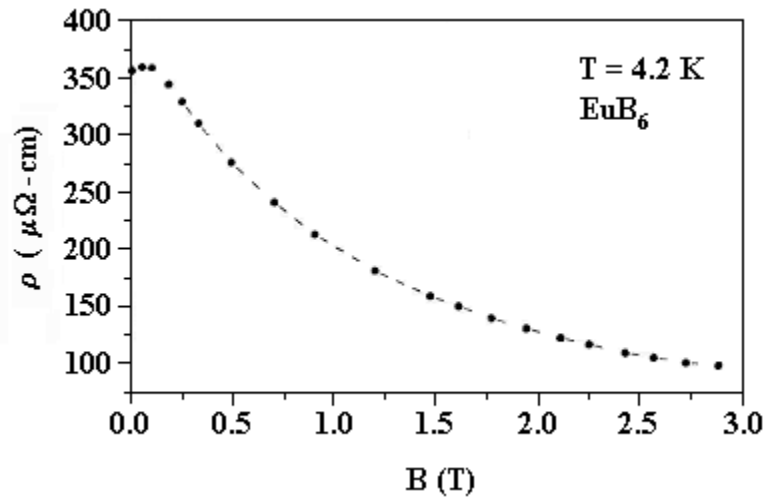


Figure 3-1. Resistivity versus applied magnetic field in EuB_6 [66].

Another mechanism by which a negative magnetoresistance can be attained is observed in semiconducting systems. The resistivity of the semiconductor can be reduced due to the application of a magnetic field and the subsequent paramagnetic splitting of the conduction band. The resultant band structure features one spin band closer to crossing the valence band. Since the conduction of this band is exponentially dependent on its proximity to the valence band, it will dominate the transport and give rise to a lower resistivity resulting from the reduced gap. This effect is clearly represented by the high-field magnetoresistance of semiconducting SmB_6 [67], shown in Figure 3-2.

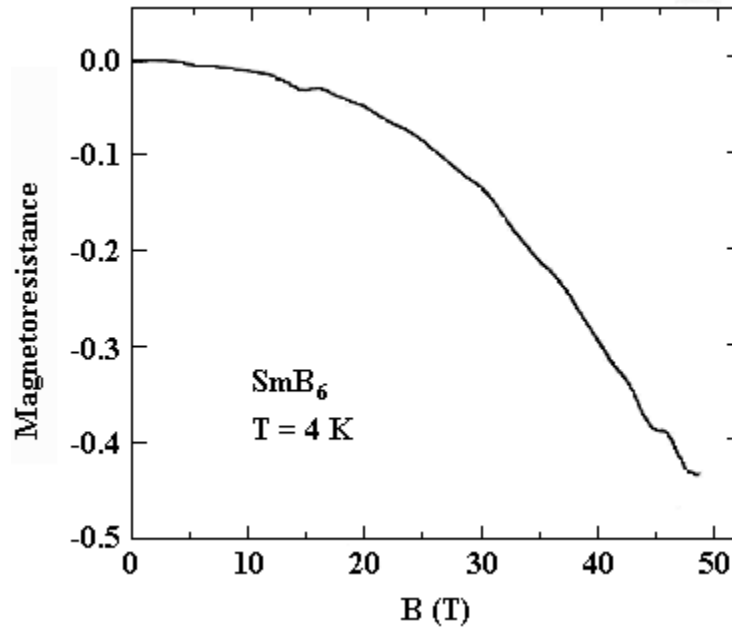


Figure 3-2. Magnetoresistance versus applied magnetic field in SmB₆ [67].

3.2.2. Electrons in Applied Magnetic Field II: Hall Effect

The Hall effect is a widely used method for measuring the carrier concentration in a material. While the magnetoresistance, as discussed above, is the change in resistivity along the direction parallel to the current, or longitudinally, in the presence of a magnetic field, the Hall effect is the change in resistivity along the direction perpendicular to both the current direction and the magnetic field. In Cartesian coordinates, if the current flows in the y-direction, the Hall voltage is measured along the x-direction, and the magnetic field is applied in the z-direction, as shown in Figure 3-3.

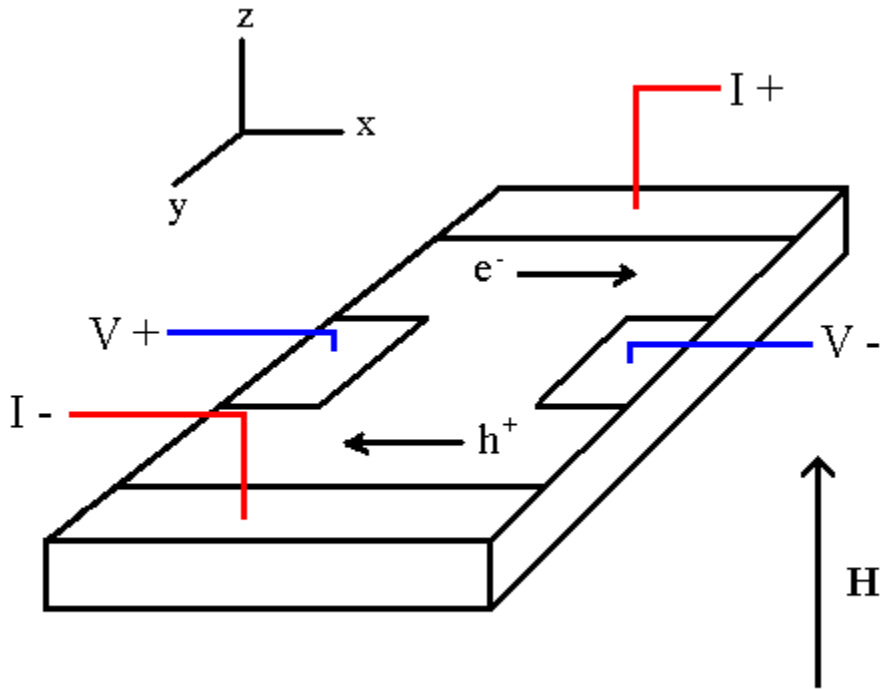


Figure 3-3. Contact configuration for performing Hall effect measurements.

The Hall effect is a manifestation of the manner in which the magnetic field exerts forces on different charge carriers. The electrons are pushed to one side of the crystal, and the holes are pushed to the other. The transverse voltage can be interpreted to give the carrier concentration by Equations (3-3) and (3-4), applicable to a system with a majority carrier type.

$$V_H = R_H IH/d \quad (3-3)$$

$$R_H = (ne)^{-1}, \quad (3-4)$$

where V_H is the Hall voltage, R_H is the Hall coefficient, I is the longitudinal current, H is the applied magnetic field, d is the thickness of the crystal, n is the carrier concentration, and e is the charge of the particle. The sign of the Hall coefficient conveys the nature of

the charge carriers. A positive value corresponds to holes, and a negative value indicates electrons.

Corrections to this simple analysis are required for a compensated system, in which both electrons and holes participate in conduction. Complications arise because the Hall coefficient is dependent not only on the carrier concentrations for each type of carrier, n and p , but also on the corresponding mobilities, μ_n and μ_p , as shown in Equation (3-5). As a result, the Hall coefficient reveals the sign of the dominant carrier type, but quantitative results are difficult to extract.

$$R_H = \frac{p \mu_p^2 - n \mu_n^2}{e (p \mu_p + n \mu_n)^2} \quad (3-5)$$

The presence of interacting magnetic moments in a material can further complicate the Hall effect. In addition to the externally applied magnetic field, the magnetism of the material itself influences the trajectories of the charge carriers. Under these conditions, the anomalous Hall effect appears. Instead of a linear dependence of Hall voltage on magnetic field, a hysteretic component can contribute to the signal.

In a ferromagnet that displays hysteresis in magnetization versus field, the Hall voltage will also be hysteretic at fields less than the saturation field. The origin of this behavior is easily explained. When an external magnetic field is applied, the magnetic moments become increasingly aligned with increasing field. The fraction of aligned moments determines the magnitude of the internal field experienced by the charge carriers. Since the Lorentz force is proportional to magnetic field, the internally induced component of the Hall voltage should follow the response of the magnetization to applied

field. The observed Hall resistivity, the ratio of Hall voltage to longitudinal current, takes the form of Equation (3-6):

$$\rho_H = R_o B + R_S 4\pi M, \quad (3-6)$$

where R_o is the conventional Hall coefficient, B is the applied magnetic field, R_S is the anomalous Hall coefficient, and M is the sample magnetization, which is field-dependent until saturation of the moments.

3.3 Electron Tunneling Spectroscopy

The density of states of a material contains valuable information that can advance the understanding of the physical properties of that material. One method by which the density of states can be probed is electron tunneling spectroscopy, in which the quantum mechanical transmission of electrons across a thin insulating barrier can be monitored and used to interpret the distribution of electronic states within a solid. The technical aspects of tunneling will be presented in chapter 4. Subsection 3.3.1 will serve to introduce the basic theory of tunneling, while subsection 3.3.2 will discuss features known as zero bias anomalies that can appear in tunneling spectra.

3.3.1 Theory of Tunneling

A tunnel junction consists of a sandwich structure, where a thin insulating material separates two electrodes. Many variations of tunneling spectroscopy exist, in which the electrodes can have very different electronic environments. Commonly, the electrodes are normal metals, superconductors, or magnetic materials, and the type of one electrode can differ from that of the opposite electrode. The appearance of the spectra may differ with type of electrode, but what it represents to first order is characteristic of the material, in the sense that the choice of barrier does not influence the form of the

normalized tunneling spectra but may superimpose a linear or quadratic background onto the conductance signal.

The quantity measured in a tunneling experiment is the conductance across the tunnel barrier, dI/dV . By applying a DC bias voltage across the junction, the chemical potentials of the electrodes can be shifted with respect to each other, as depicted in Figure 3-4 [68]. The tunneling conductance represents the product of the densities of states of the two electrodes, and the bias voltage indicates the energy level with respect to the Fermi energy that is being investigated.

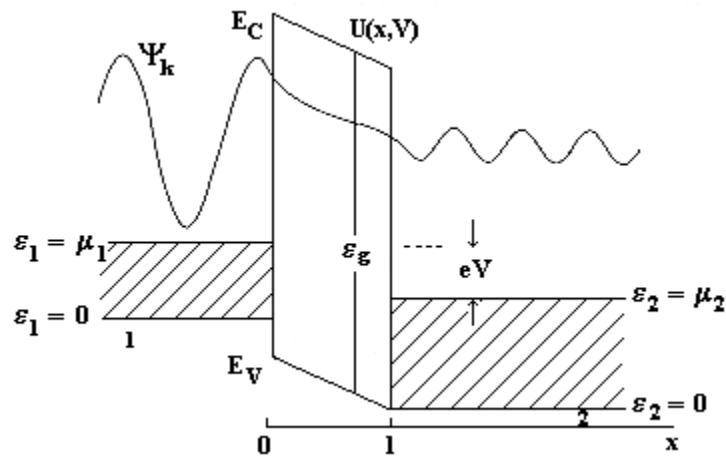


Figure 3-4. Schematic of electron tunneling. The electronic wavefunction tunnels from electrode 1 to electrode 2 through an insulating barrier of height U . The bias voltage, V , is applied to shift the densities of states with respect to one another [68].

One arrives at the conclusion that the tunneling process reveals information about the density of states through a calculation of transition probability per unit time [69].

This quantity is approximately obtained by treating the tunneling Hamiltonian as a perturbation with respect to the Hamiltonians, H_1 and H_2 , of each electrode. There is assumed to be no electron-electron interaction across the barrier. The conserved

quantities in tunneling spectroscopy are taken to be the transverse momentum and total energy. Based in these approximations, Fermi's golden rule can be used to obtain the transition probability per unit time between electrodes 1 and 2. The transition probably differs from the tunneling current by a prefactor, denoted as A in the following expression.

$$\begin{aligned}
 I_{1-2} &= A \int_{-\infty}^{\infty} |T|^2 N_1(E) f(E) N_2(E+eV) [1-f(E+eV)] dE \\
 I &= I_{1-2} - I_{2-1} \\
 &= A |T|^2 \int_{-\infty}^{\infty} N_1(E) N_2(E+eV) [f(E) - f(E+eV)] dE
 \end{aligned} \tag{3-7}$$

The expression, as shown in Equation 3-7 [70], is intuitive. N_1 and N_2 are the densities of electronic states in electrodes 1 and 2, respectively. An electron with energy E is annihilated in electrode 1, leaving a vacant state. An electron with energy $E+eV$ is created in electrode 2, filling an empty state and conserving transverse momentum. The product of these densities of states is multiplied by the tunneling probability $|T|^2$ and the corresponding Fermi distribution functions, so that the expression is valid at finite temperature. At zero temperature, dI/dV is simply proportional to the product of the densities of states. At finite temperature, the tunneling conductance is, to first order, proportional to the product of the densities of states of the two electrodes, and correction terms only become important when the thermal energy becomes comparable to the Fermi energy, which is typically tens of thousands of Kelvin. The form of this product, and in turn the appearance of the tunneling spectrum, depends on how the densities of states of the electrodes vary with bias voltage.

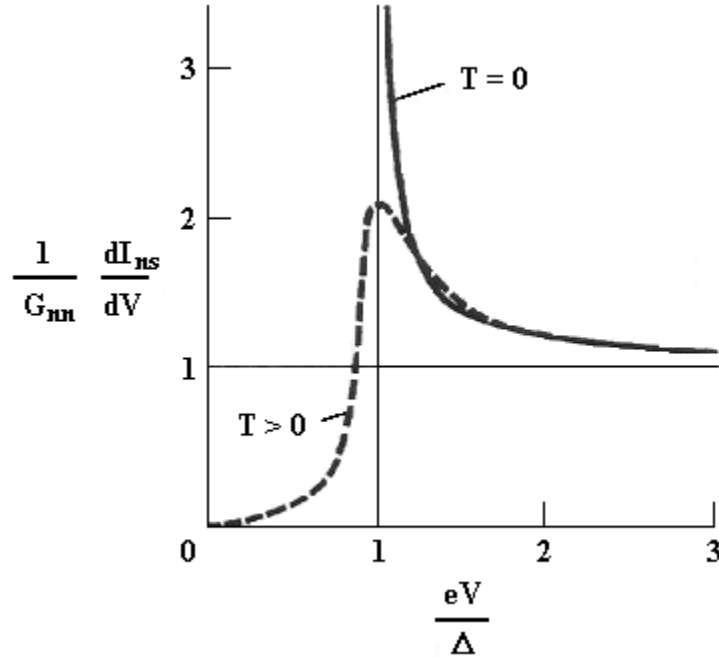


Figure 3-5. Normalized tunneling conductance versus positive bias voltage in a BCS superconductor [70].

A normal metal has a density of states that is roughly constant in energy at moderate bias voltages. A metal is commonly used as the counter-electrode to study a material that is not well characterized because the tunneling spectrum of such a structure is proportional to the density of states of interest. The density of states for a superconductor, however, reveals the gap structure about zero bias and, for a BCS superconductor at zero temperature, follows the form given in Equation (3-8) [70], where N_s is the superconducting density of states and N_n is the normal density of states. An illustration is given in Figure 3-5 at zero temperature and at finite temperature, where there is thermal smearing of the gap edge.

$$N_s(E) = \begin{cases} N_n(E) E / (E^2 - \Delta^2)^{1/2} & |E| \geq \Delta \\ 0 & |E| < \Delta \end{cases} \quad (3-8)$$

Under certain circumstances, inelastic excitations can couple to the quasiparticles in the electrode and appear as broad features at characteristic energies in the tunneling conductance versus bias voltage [69]. An example of this phenomenon can be found in so-called strong-coupling superconductors like Pb and Hg. In these materials, electron-phonon interactions induce a spreading of the single-particle states so that they are no longer eigenstates of the BCS Hamiltonian. The signatures of these states appear as deviations centered about 7 meV and 11 meV in the tunneling spectrum as shown in Figure 3-6 for Pb.

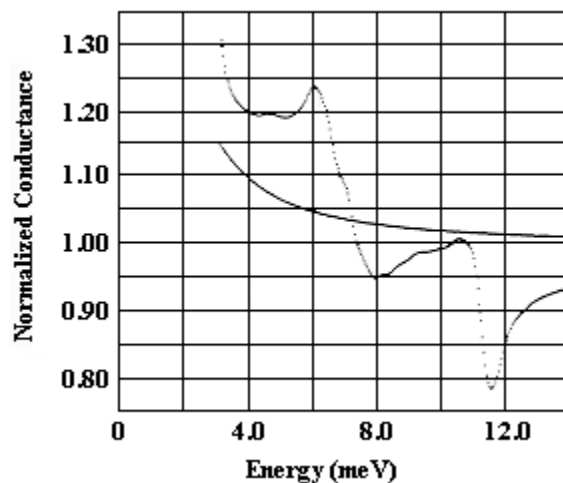


Figure 3-6. Tunneling conductance versus bias voltage in a Pb-I-Pb junction. The coupling of phonons to the quasiparticle spectrum is seen as maxima in the broken data. The solid curve represents BCS theory [69].

In a manner similar to the phonon structure discussed above, evidence for other types of inelastic excitation can be seen in tunneling. For example, a ferromagnetic metal may reveal magnons or magnetic polarons in the form of smoothly varying bumps or wiggles [71]. The identity of the feature depends critically on the energy scale at which the features appear.

3.3.2 Zero Bias Anomalies

Sharp features centered about zero voltage in the tunneling conductance known as zero bias anomalies (ZBAs) have been associated with inelastic mechanisms present in the electrode [68]. The concept of a ZBA was introduced in chapter 2 during the discussion of tunneling results in EuB_6 , and it was noted that the appearance of the zero bias peak is simultaneous in temperature with ferromagnetic ordering. It is important to mention that there is no consensus concerning the origins of these features, and the term anomaly certainly suggests incomplete understanding.

One type of ZBA is known as the giant resistance peak and is the least understood of all types of ZBA. This type of feature has appeared in work on Cr-CrO_x-Ag tunnel junctions [72], as shown in tunneling *resistance* (dV/dI) versus bias voltage (Figure 3-7). Initial observations noted that there are most likely magnetic moments present in the barrier, as CrO₂ is ferromagnetic and CrO₃ is antiferromagnetic. Mezei and Zawadowski presented a Kondo-like effect as a possible mechanism leading to the increase in resistance [73]. This mechanism explained a logarithmic dependence of the resistance on temperature but was inadequate to explain the magnitude of the effect, which can be two orders of magnitude larger than the resistance at 100 meV. A guideline provided by this model is that conductance peaks are produced by moments in the barrier and dips are a result of moments in the electrode. Artificial implantation of magnetic Ni into Al electrodes gave a giant resistance peak [74] of the correct magnitude, but no conclusions have been reached as to the actual mechanism responsible for the effect.

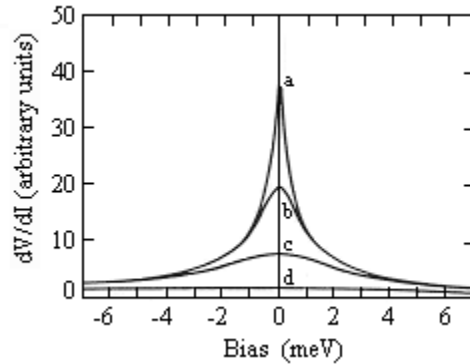


Figure 3-7 Zero bias anomalies in the tunneling resistance versus bias voltage for a Cr-CrO_x-Ag tunnel junction [72] at

- (a) $T = 0.9$ K
- (b) $T = 20.4$ K
- (c) $T = 77$ K
- (d) $T = 290$ K

In metals, conductance peaks and dips can appear for various reasons. In an experiment undertaken by Cooper and Wyatt (1973) [75], magnetic and non-magnetic dopants were introduced into host electrodes chosen to be Al and Ag separated by a thin layer of Al₂O₃. When the dopants were confined to the Ag electrode, conductance peaks were observed only for Ti and Ni, as shown in Figure 3-8(a). When Al was chosen to be the host electrode, a conductance peak was seen for all dopants except Mn, as shown in Figure 3-8(b). These conflicting results indicate that the host electrode into which the dopants are introduced is highly influential on whether or not zero bias peaks are seen.

Interpretation of the results presented above within the Mezei and Zawadowski model suggests that impurities in Ag are more likely to produce a magnetic moment within the metal, while in Al, it is suggested that the moments are more likely to be situated in the barrier. This scenario is somewhat awkward in its viability. An alternate picture, given by Wyatt (1974) [76], relies on an estimate of the magnetic coupling

strength as a product of the s-d exchange energy and density of states of the electrode at the Fermi level.

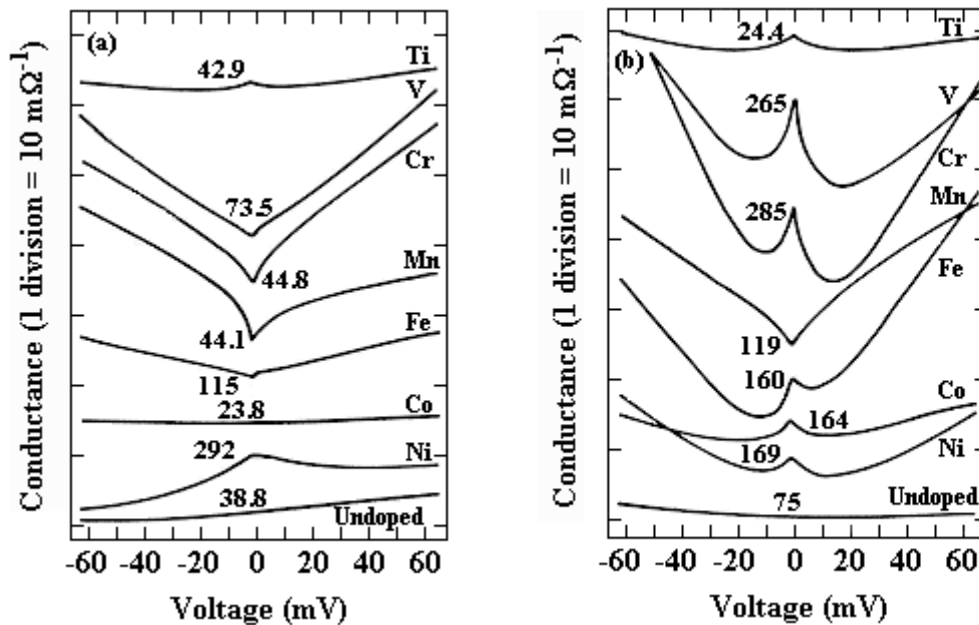


Figure 3-8. Zero bias anomalies in the tunneling conductance versus bias voltage for magnetically doped electrodes of (a) Ag and (b) Al. The data are expressed in the same units of conductance but shifted with respect to each other for presentation purposes. The zero bias conductance is given as the number corresponding to each curve [75].

Table 3-1 lists the dopants used, the number of 3d electrons each possesses, whether a moment exists when incorporated into the host electrode, as interpolated by the presence or absence of a zero bias peak, and the strength of the moment. The s-d exchange constant is inversely proportional to both the magnitude of the moment and the energy of the d-band relative to the Fermi level. The presence of a magnetic moment is expected to correspond to a lower limit of the coupling strength, $JN(0)$. It is known that Ag has a smaller density of states at the Fermi level than does Al. Since J is inversely proportional to the product of the total spin of the impurity and the energy of the d-band relative to the Fermi energy, a qualitative prediction can be made. Small spins

accompanied by low d-band energies give large values for J , which apparently collaborate with the small $N(0)$ in Ag to give local moments, as observed experimentally for spin-1 Ti and Ni. The larger $N(0)$ in Al accommodates larger spin values and d-band energies, giving a smaller J , to satisfy the requirement for local moment formation.

These predictions are consistent with experiment, as moments appear to be formed in the Al electrode for a broad range of dopant spin.

Table 3-1. Dopants purposefully implanted into metallic tunnel junction electrodes and corresponding properties [76].

Dopant	n (3d)	Junctions		Nominal Spin
		Ag	Al	
Ti	2	Y	Y	1
V	3	N	Y	3/2
Cr	4	N	Y	2
Mn	5	N	N	5/2
Fe	6	N	Y	2
Co	7	N	Y	3/2
Ni	8	Y	Y	1

This brief discussion of zero bias anomalies is intended to form the framework within which comparisons can be made between the data from intentionally doped electrodes presented above and tunneling spectra of ferromagnetic compounds such as EuB_6 (see chapter 2) and, in a preliminary way, CaB_6 , as will be presented in chapter 5. Further information on zero bias anomalies in compounds less related to this work can be found in *Principles of Electron Tunneling Spectroscopy* by E. L. Wolf [68].

CHAPTER 4 EXPERIMENTAL TECHNIQUES

In this chapter, the technical aspects of this work will be discussed. First, a brief description of the growth of the CaB_6 crystals will be given, followed by sample preparation methods prior to our transport measurements, including resistivity, Hall effect, and magnetoresistance. An overview of electronic, magnetic field, and data acquisition equipment will follow. In addition, a presentation of planar tunneling techniques, as well as the low-noise electronics required for these investigations, will be provided.

4.1 Crystal Growth and Doping

Single crystals of CaB_6 were grown and provided by Z. Fisk's group at Florida State University. The samples were grown out of a molten Al flux using high-purity starting materials, encapsulated in an alumina crucible. Stoichiometric CaB_6 required an excess of Ca that was incorporated into the melt, due to the suggestion of a tendency of this material to form Ca vacancies. In the initial growth process, it was believed that the excess Ca is not incorporated into the resultant crystal. Further discussion of this assumption is given in the conclusions presented in Chapter 6.

Electron doping was achieved by substitution of La for Ca. The data presented in this work were obtained from samples that were La doped at a level of roughly 0.5%. A second doping procedure involved the exclusion of a small amount of Ca from the melt, in an effort to intentionally incorporate Ca vacancies into the material. In the discussion

of experimental findings, the electron-doped system will be denoted by $\text{Ca}_{1-\delta}\text{La}_\delta\text{B}_6$, the intended stoichiometric material will be labeled CaB_6 , and the Ca deficient compound will be referred to as $\text{Ca}_{1-\delta}\text{B}_6$.

These single crystals form in a rectangular shape with typical dimensions being approximately 2mm x 0.5mm x 0.5mm. However, we believe that electron transport may be confined to a fraction of the crystal smaller than the physical size would suggest. As an adequate means of measuring these reduced dimensions is absent, an attempt has been made to conduct all transport measurements corresponding to a particular doping concentration on the same crystal, so that the results can be related within the data set.

4.2 Transport Measurement Techniques

The oblong crystal shape adopted by these samples suggests a natural orientation for contact formation. The contact configuration shown in Figure 4-1 was found to be suitable for resistivity, Hall effect, and magnetoresistance simultaneously. A significant advantage to this permanent configuration became apparent during studies of the Ca deficient compound, where it was discovered that repeated processing of this material generates small cracks in the crystal, drastically altering the transport properties of the sample. Tunneling experiments employed a tri-layer structure that will be described in Subsection 3.2.2.

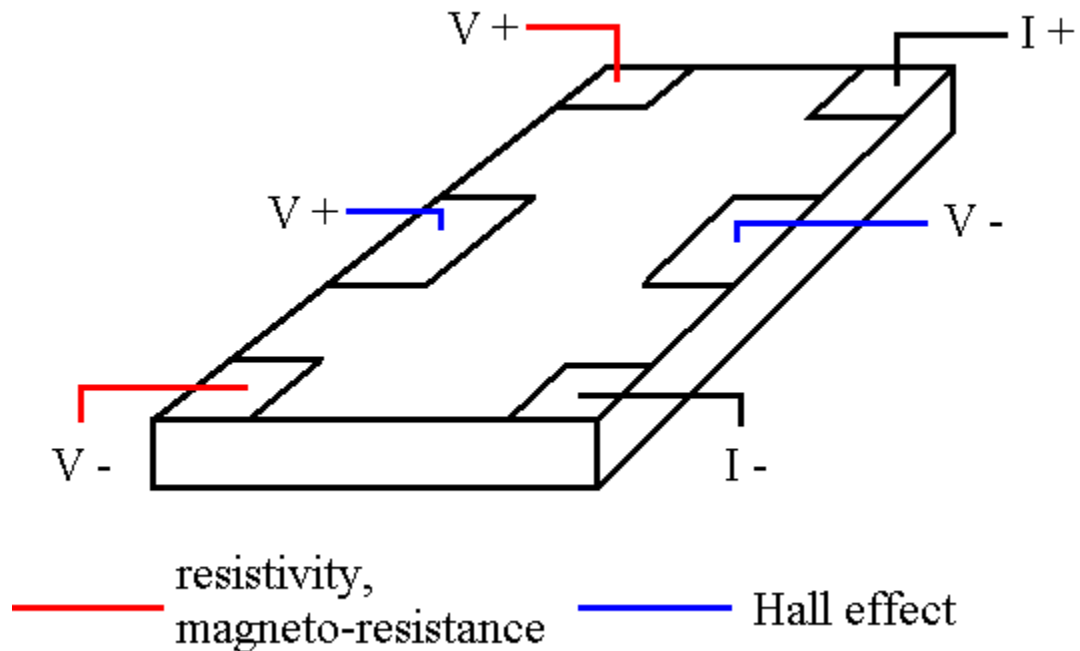


Figure 4-1. Contact configuration for simultaneous measurement of resistivity, magnetoresistance, and Hall effect.

4.2.1 Resistivity, Hall Effect, and Magnetoresistance

Initial efforts to establish electrical contact to the crystals entailed submersion into a weak nitric acid solution for 5 minutes, followed by a rinse in water, and manual application of conductive silver paint in the desired contact configuration. Upon the observation that the contacts deteriorated with thermal cycling, it was apparent that a more careful process would be required. Good-quality, low-resistance contacts were formed in a high vacuum chamber with a base pressure of 5×10^{-7} Torr. To clean the surface and improve sticking probability, the crystal was exposed to a high-purity Xe plasma at a beam voltage of 450 V. This was followed by thermal evaporation of 20 nm of Au in the pattern discussed above defined by a shadow mask. Subsequent 8- to 12-

hour annealing in an inert Ar environment at temperatures of approximately 100 °C further established the low-resistance character of the contact pads.

The Hall effect and magnetoresistance studies, for which a magnetic field is required, were conducted in a ^4He cryostat, as shown in Figure 4-2. The dewar is equipped with a pump-out port, making possible a base temperature of 1.6 K, as well as an American Magnetics, Inc. (AMI) superconducting magnet with a maximum field of 8 Tesla. The cryostat is equipped with temperature sensors, a small resistive heater for low temperature regulation, and a power resistor with which temperatures near 300 K can be attained. Two layers of vacuum provide good thermal isolation of the sample stage from the liquid helium bath making high temperature measurements in magnetic field possible. Temperature regulation was performed using a LR-400 resistance bridge coupled with a LR-130 temperature controller. At low temperatures, the small 50 Ω resistor provided adequate heating. Above roughly 15 K, the 5-Watt power resistor served to bring the equilibrium temperature up, while the small resistor functioned as a fine control.

A smaller ^4He probe with one layer of vacuum isolating the sample from the helium bath was employed for resistivity measurements. The temperature was varied in a very simple way. Cold N_2 gas was first circulated through the N_2 jacket, without collecting liquid. Liquid He was transferred into the dewar only until the sample reached 4.2 K. With the aid of automated data acquisition, which will be described below, the measurement can be performed without supervision, as the dewar slowly warms. The voltage output of the LR-400 is used to record the sample temperature.

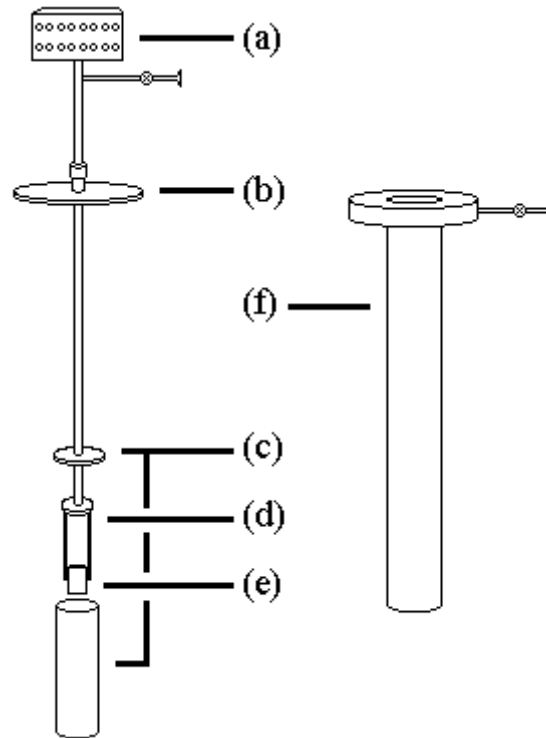


Figure 4-2. Depiction of ^4He cryostat with pump-out port used for magnetotransport measurements.

- (a) Measurement leads.
- (b) Flange to mate with top of dewar, pressure fitting to adjust height.
- (c) Vacuum can with Ag solder seal (first layer of vacuum).
- (d) Thermal insulation of stage from He bath.
- (e) Cu sample stage with θ -rotation capability.
- (f) Outer vacuum jacket with pump-out port (second layer of vacuum).

All transport measurements were performed in an RF shielded room using analog electronics, including a Princeton Applied Research (PAR) 124A lock-in amplifier equipped with a PAR 116A preamplifier and accompanied by low-noise Ithaco 1201 preamplifiers. The sample was driven with an AC level out of the lock-in. Constant current was achieved by placing in series with the sample current leads a dropping resistor of value $R_{\text{drop}} = 100 \times R_{\text{sample}}$ or greater. The current through the sample was measured during data acquisition to confirm its constancy. The voltage across the sample was first fed into an AC-coupled preamplifier, whose output was followed by the lock-in

amplifier. The output of the lock-in, as well as the independent parameter (temperature, magnetic field) were measured and transmitted out of the shielded room to an automated data-acquisition LabVIEW program by fiber optic cable.

For the Hall effect and magnetoresistance measurements, an AMI superconducting magnet was used to produce fields up to 8 Tesla. The magnet was employed using an AMI 4Q-05100 four-quadrant power supply and an AMI 420 power supply programmer. Data points were taken by ramping the magnet to a specific field and recording a number of points, usually 5 points/field, to be averaged in data analysis. This eliminated two undesirable effects: not only is there a high level of noise associated with field ramping, but this technique also corrects for a lag in sample voltage with respect to field due to the time interval intrinsic to the data acquisition technique. Attempting to measure the anomalous Hall effect is an exception to this static-field procedure. During these measurements, the magnet ramp rate was sufficiently low that the time lapse between recording the field and recording the sample voltage was taken to be negligible.

Data analysis was performed using Origin. Since magnetoresistance tends to contain contributions from the Hall effect, and vice-versa, it was important to take magneto-transport data at both positive and negative magnetic fields. In this way, accurate results were obtained by eliminating any anti-symmetry seen in the magnetoresistance and any symmetry in the high-field Hall voltage. This procedure is, in effect, the van der Pauw method of correctly measuring said quantities [77].

4.2.2. Tunneling Spectroscopy

Further investigation of the electronic structure in the form of planar tunneling spectroscopy was performed on a crystal of the La doped material. Tunneling is a

technique by which one can measure the density of electronic states at energies away from the Fermi level. The tunneling structure is a tri-layer junction formed by the material to be investigated and a well-characterized material separated by an insulating layer a few tens of angstroms thick, as depicted in Figure 4-3. The tunneling conductance, dI/dV , across this device is approximately proportional to the product of the density of states of the two electrodes. Typically, the counter-electrode of choice has a constant density of states, as in the case of a metal or superconductor above its T_c , so that the tunneling conductance is proportional to the material being studied. By applying a variable DC bias to the junction, the Fermi levels of the two electrodes are shifted with respect to one another, and the density of states at energies away from the Fermi level can be probed. For an in-depth discussion of tunneling spectroscopy, see chapter 3.

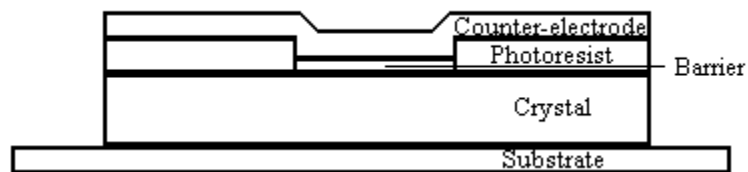


Figure 4-3. Cross-section of a tunnel junction. An area of roughly $20 \mu\text{m}^2$ has been exposed and developed in the photoresist, defining the area of the junction. This figure is not to-scale.

For all tunneling results presented in this work, the counter-electrode was Pb, which has a T_c , convenient for working at liquid He temperatures. The advantage of using a superconducting counter-electrode is the diagnostic capability of measuring its I-V curve below T_c . The quality of the tunnel barrier can be determined by the sharpness of the gap, an example of which for EuB_6 is shown in Figure 4-4. Here, the gap edge can be clearly seen as a change in slope at a bias voltage roughly equal to the value of the

superconducting gap. Another test of junction quality is to determine the ratio of the four-terminal dynamical resistance at energies less than the gap to that at energies greater than the gap. A ratio of $R_{<\Delta}/R_{>\Delta} = 100$ at $T \leq T_C/2$ is considered an indication of a good-quality barrier. Additionally, phonon modes, which appear as local extrema in the tunneling conductance, can be detected at bias voltages 7 mV and 11 mV. In the presence of inelastic tunneling mechanisms, which are highly undesirable when present in the barrier, this phonon structure will be undetectable.

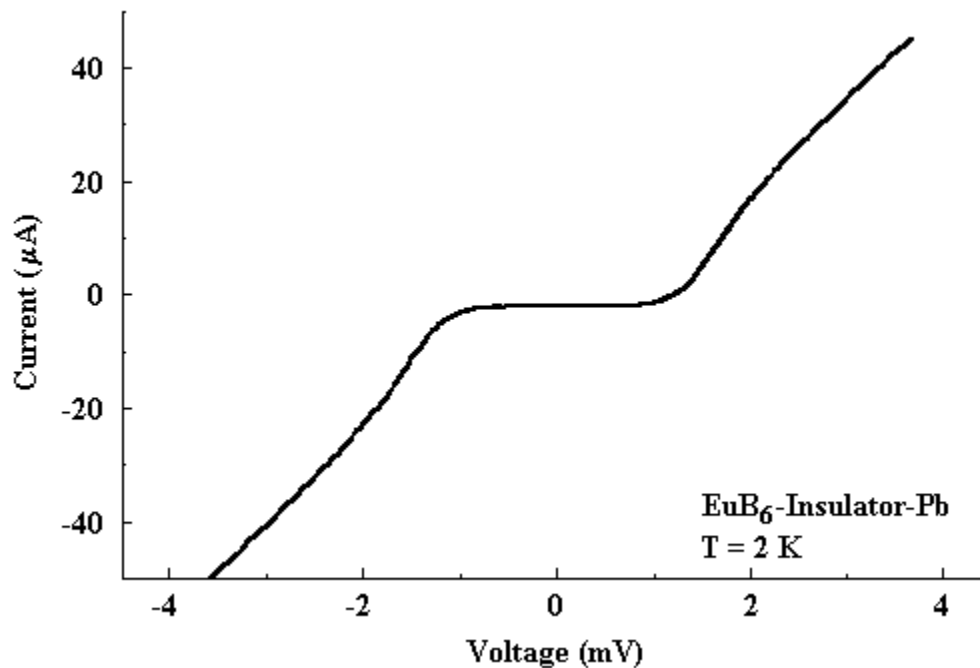


Figure 4-4. I-V characteristic of a EuB₆-I-Pb tunnel junction. The gap about zero bias is clearly seen, as is the break in slope occurring at roughly ± 2 mV.

The most significant difficulty has been to fabricate a high-quality insulating barrier. Many variables contribute to the success of a barrier. Not only must a fabrication method be optimized, which is a challenging process, but the surface of the

crystal must be smooth, the Pb counter-electrode must be protected against shorting to the electrode, and the method of defining the junction area must be able to withstand cold temperatures without cracking.

The process that was found to be optimal for tunneling into CaB₆ was preceded by a 5-minute etch in a weak nitric acid solution. This was designed to remove residual Al left by the growth process from the crystal surface. The next task was to define the junction area. This consisted of the selection of a smooth portion and an increase in the likelihood of forming a uniform barrier. The remainder of the crystal is electrically isolated during this step by spinning a layer of 1350J photoresist at 4000 rpm for 30 seconds. After baking the photoresist layer at 75 °C for at least 20 minutes, optical lithography was used to expose a region of the surface roughly 20 μm² in area. The photoresist was then developed in AZ351, a sodium boride-based developer, for 20 seconds and rinsed in water. A thin insulating layer was then formed on the bare surface of the crystal by a 20-minute exposure to a reactive ion etch of CCl₂F₂ at 20 Watts. This procedure is believed to remove boron from the surface of the crystal, leaving the Ca-rich surface free to oxidize upon exposure to the atmosphere. Using a Cu evaporation mask to limit coverage of the counter-electrode, the sample was loaded into a high vacuum chamber with a base pressure of 5x10⁻⁷ Torr, and 500 nm of Pb were thermally deposited to form the counter-electrode.

While photoresist is used to not only define the junction area but also to electrically isolate the crystal from the Pb, cracks can easily develop along the crystal edges at low temperatures. The material found to be well suited to withstand low temperatures is a mixture of one part Duco cement to three parts n-Butyl Acetate. A drop

of green paint was commonly added to make the adhesive visually distinguishable during manual application. Once the contacts are confirmed to be electrically isolated from each other and from ground, the sample is mounted onto the ^4He probe. Thin Au wire is attached to the contact pads in a four-terminal configuration such that current is injected across the barrier, and voltage is measured independently across the barrier. This eliminates the voltage contribution from the leads that would be present in a two-terminal measurement.

When conducting tunneling measurements, the quantities of interest are typically very small in magnitude. It is essential, therefore, to perform these studies in a low-noise environment. All data sets to be presented were taken in an RF shielded room with analog electronics. Care must be taken to prevent voltage transients across the junction, which can easily destroy the thin barrier. For this reason, shorting the junction leads is necessary when setting up the measurement and electrically connecting the sample to the current source.

There are two components of the voltage applied to the junction. One is a DC level produced by a completely passive analog circuit with ramping capabilities as well as a manual voltage adjustment. A small AC voltage at a frequency of roughly 1 kHz, but not a harmonic of 60 Hz, originates from a PAR 124A lock-in amplifier and is added to the larger DC signal. This circuit is shown in Figure 4-5. The DC voltage is the bias voltage. For high-resolution spectroscopy, the AC voltage must be much smaller in amplitude than the DC level, $V_{AC} < 0.05 V_{DC}$, since we will be using this configuration to measure the dynamical resistance, or the inverse of the tunneling conductance, versus bias voltage. The objective is to keep a constant current, with the use of a dropping

resistor, as described above, so that the recorded dynamical resistance of the junction is proportional to the voltage response. The DC voltage drop across the junction is recorded as the bias voltage. The need for low-noise conditions is now apparent when we consider the magnitude of the sample response to the small AC excitation.

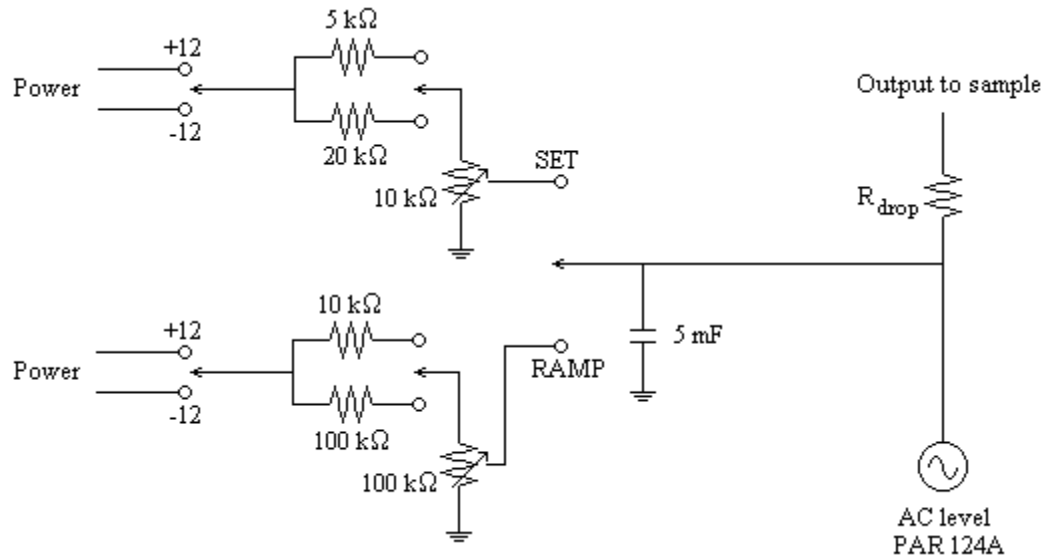


Figure 4-5. Circuit diagram for tunneling measurements. The ramp and set functions manipulated the bias voltage. A lock-in amplifier, set at roughly 1 kHz, produces the small AC excitation.

All tunneling measurements were performed in the simple liquid He probe without magnetic field capabilities, as described above. Diagnostic evaluation of the quality of the superconducting Pb structure is best done at $T < T_c/2$, where the gap has sufficiently developed. By utilizing the pumping port, we were able to reduce the pressure in the He space and, consequently, the temperature of the system. Base temperature for this process is 1.6 K, where ^4He approaches a superfluid, and its vapor pressure is very low. Temperatures above 4.2 K were achieved by varying the vertical

position of the sample within the dewar, taking advantage of the vertical temperature gradient.

It is useful to take tunneling data for a broad range of temperatures. In this way, it is possible to investigate the progression of the density of states as the temperature is altered, an ability especially valuable in the neighborhood of a phase transition. These very sensitive measurements are best taken with an x-y plotter, advantageous for its high resolution. The spectra were then converted into a set of x-y points using Un-Scan-It. Analysis of the data was finally performed using Origin.

CHAPTER 5 PRESENTATION OF RESULTS

In this chapter, the results of this work on CaB_6 and its electron-doped and Ca-deficient variants will be presented. The contents included here will be the foundation for the interpretation to follow in chapter 6. Section 5.1 is devoted to a description of the electronic resistivity as a function of temperature and electron content. In section 5.2, Hall effect data are provided in the form of the Hall voltage versus field and carrier concentration versus temperature and doping concentration. Magnetoresistance data are the subject of section 5.3, and electron tunneling spectra are presented in section 5.4.

One fundamental complication with attempting to measure transport properties in the single-crystal samples has been the variation in sample dimension and in sample composition. The absolute values of the resistivity are difficult to determine because the effective sample thickness, where the current is uniform, is suspected to be smaller than the physical crystal thickness. In addition, the variations in composition occur even within a single batch of crystals. To compensate for these sources of error, resistivity data that is normalized to the value at 300 K is presented for the electron-doped and Ca-deficient compounds and to the value at 50 K for the stoichiometric material. The issue of non-uniformity within a crystal batch has been addressed by using a single sample where possible throughout our series of measurements. In this way, the resistivity, Hall effect, and magnetoresistance data shown below correspond to representative samples of the same crystal stoichiometry and physical dimensions for each doping concentration.

5.1 Resistivity Measurements

Resistivity measurements are of importance in the effort to identify the electronic environment in these materials. In the process, the consistencies of various band structure predictions with experimental data have been inspected and will be addressed further in the next chapter. As will be demonstrated here, however, behaviors in the resistivity can be complex, with physical interpretations that are not immediately apparent.

Figure 5-1 shows resistivity versus temperature for the electron-doped material. The metallic nature seen here is in agreement with that reported earlier. The resistivity, normalized to the value at 300 K, shows a decrease of roughly 30 percent in the temperature range studied. At the lowest temperatures, there is a small upturn that may indicate a type of charge carrier localization. The nature of the interaction will be revisited in the following chapter of this work.

The stoichiometric material was expected to exhibit semiconducting behavior, according to a portion of the previously published work. Resistivity versus temperature, as shown in Figure 5-2, instead appears to retain marginal metallicity. The temperature dependences of the resistivities of roughly a dozen crystals grown from the same melt were measured to verify the seemingly contradictory behavior. Small variations are observed within the sample batch since the transport behavior of these crystals are highly dependent on the ratio of Ca to B₆, but the data shown corresponds to a representative CaB₆ crystal. At high temperature, an initial decrease in resistivity is seen, followed by an increase, a small maximum at 50 K, and another minimum at lower temperature. In fact, the form of the resistivity appears to indicate a competition between high and low temperature regions.

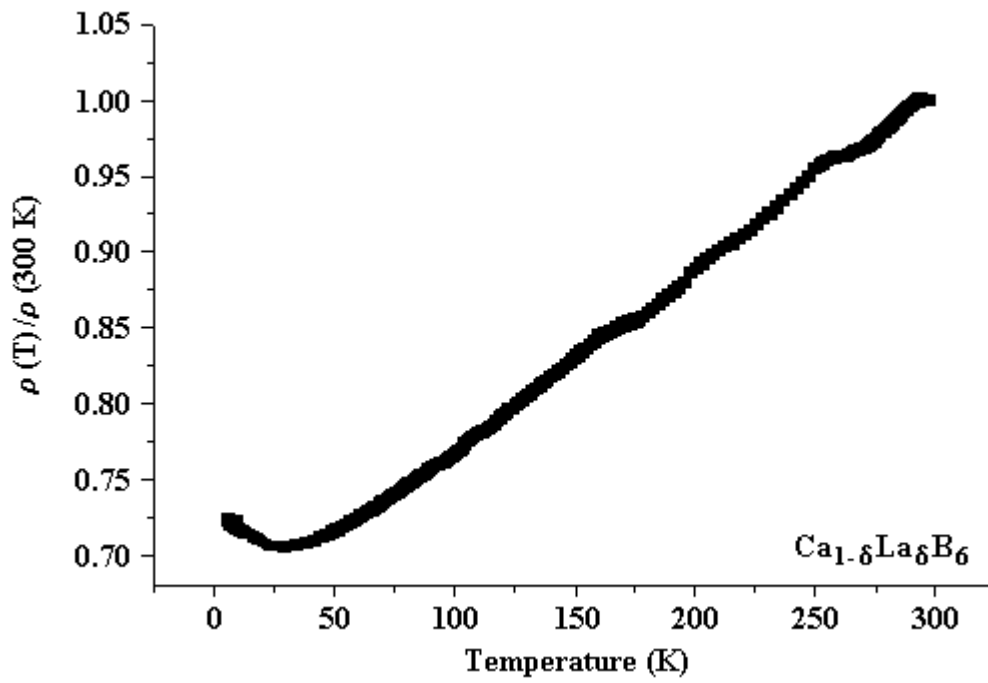


Figure 5-1. Normalized resistivity versus temperature in $\text{Ca}_{1-\delta}\text{La}_{\delta}\text{B}_6$.

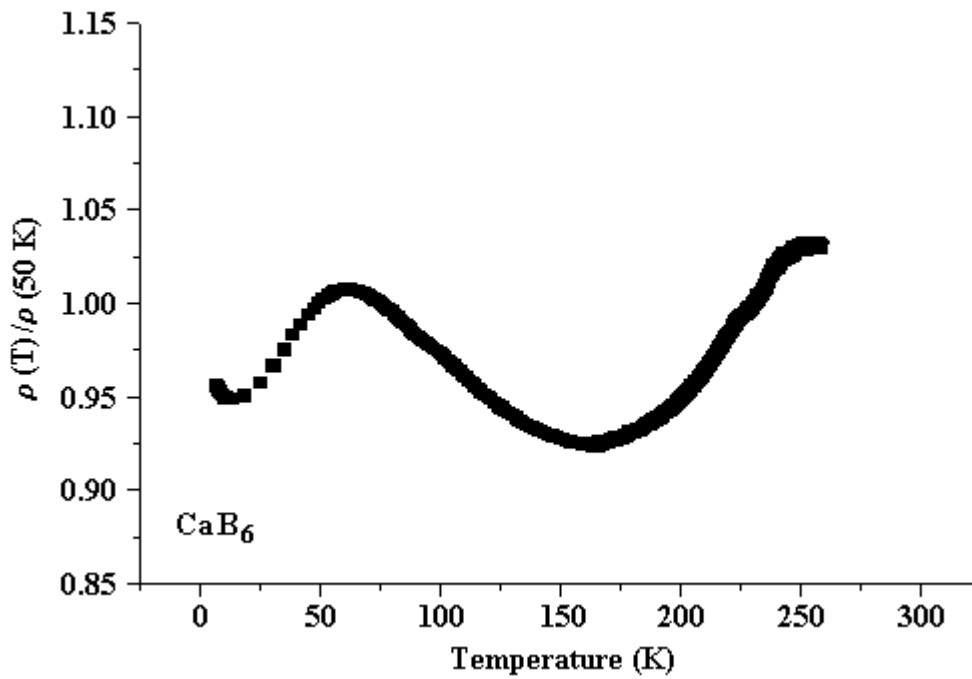


Figure 5-2. Normalized resistivity versus temperature in CaB_6 .

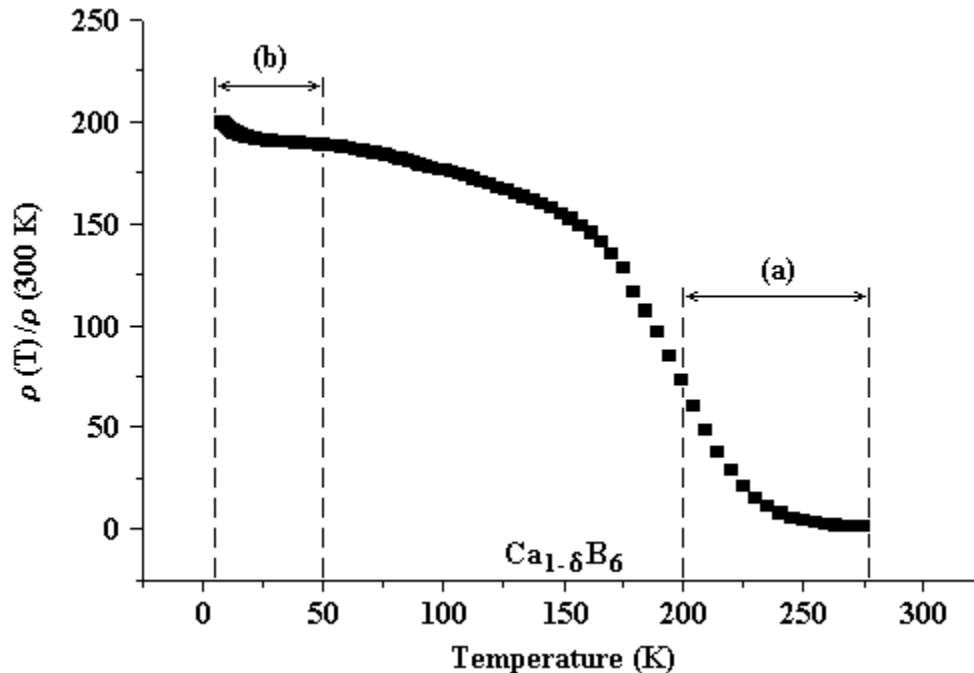


Figure 5-3. Normalized resistivity versus temperature in $\text{Ca}_{1-\delta}\text{B}_6$. The high temperature fit in Figure 5-4(a) is confined to region (a), and the low temperature fit in Figure 5-4(b) is confined to region (b).

Interestingly, semiconducting behavior was found to be present in the resistivity of crystals that were Ca-deficient. A large number of same-batch samples were measured. Data taken on a sample representative of the batch are shown in Figure 5-3 and indicate a sharp resistive rise around 175 K, followed by a low-temperature plateau. The low-temperature and high-temperature regions were fit independently to an activated form, $\rho(T) = \rho_0 \exp(\Delta/k_B T)$, where ρ_0 is the value of the resistivity when T is large. The results of this fit, as shown in Figure 5-4, are in excellent agreement with the semiconducting model, where the high temperature fit (a) yields a gap value of roughly 3500 K, or 350 meV, and the low temperature fit (b) gives a much smaller gap of roughly 0.5 K, or 0.05 meV. The temperature ranges to which these fits have been confined are shown in Figure 5-3 as regions (a), for the high-T fit, and (b) for the low-T fit. The

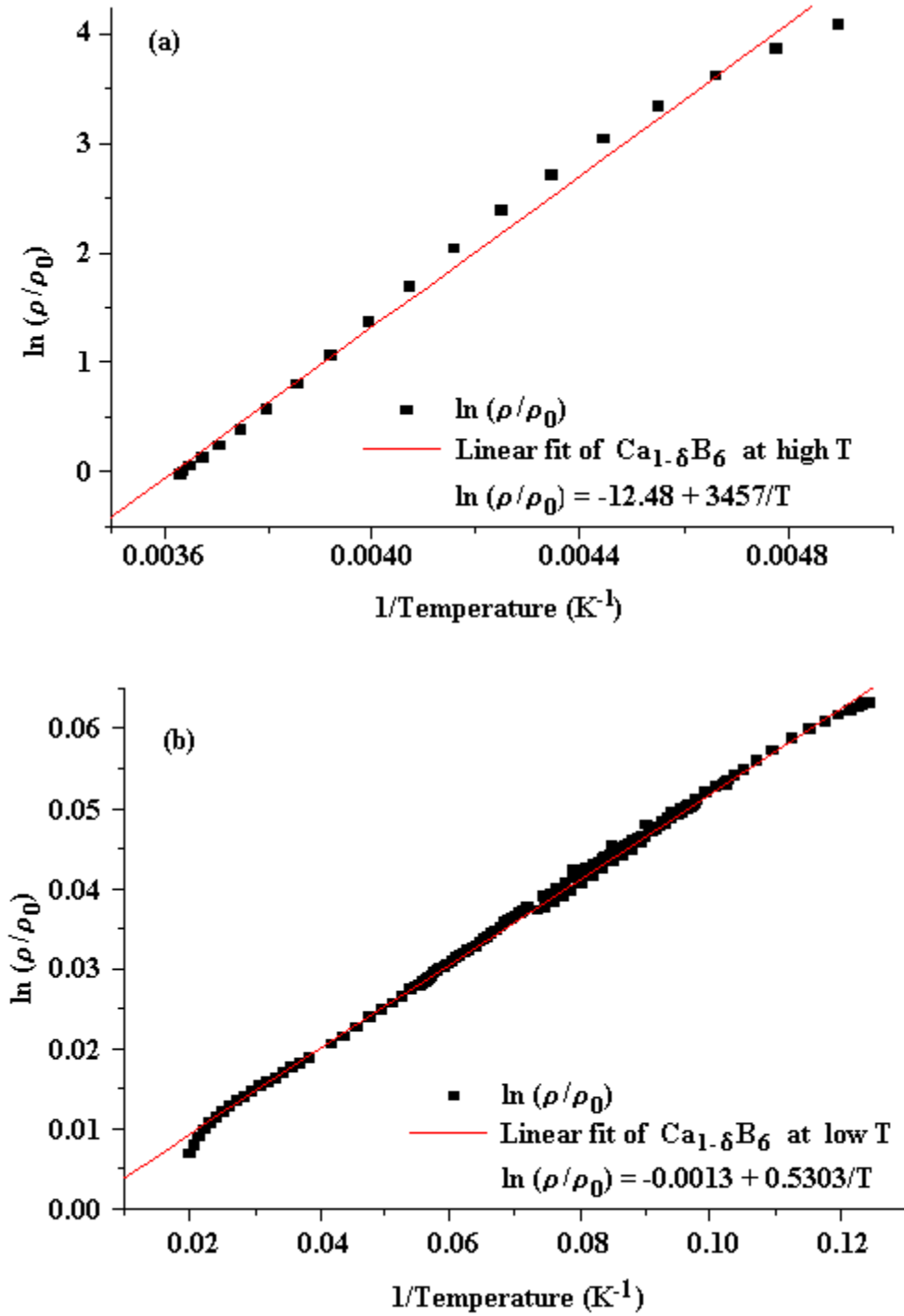


Figure 5-4. Fit of resistivity versus temperature to activated form in $\text{Ca}_{1-\delta}\text{B}_6$.
 (a) High temperature limit.
 (b) Low temperature limit.

deviation from these fits at intermediate temperatures may represent interactions poorly described by the independent two-component model employed to investigate the asymptotic limits of the resistivity results in $\text{Ca}_{1-\delta}\text{B}_6$.

To ensure that the activated behavior in the Ca-deficient material is due to Ca vacancies, a post-growth method was developed to further deplete the Ca concentration. Annealing in an oxygen atmosphere exploits the low vapor pressure of CaO to remove Ca from the surface of the crystal. This anneal was conducted at a temperature of roughly 250 °Celsius. A subsequent anneal in an inert Ar environment at a slightly higher temperature was performed in an effort to restore uniformity to the crystal, thus enhancing the concentration of Ca vacancies in the bulk.

The effect of the annealing procedure on the behavior of resistivity with temperature is shown in Figure 5-5. The data in black were taken on a Ca-deficient crystal prior to anneal. After anneal, as shown in red, the same crystal displays no detectable change in the value of the high-temperature resistivity, as can be seen in Figure 5-6, which is a magnified view of the high-temperature region of Figure 5-5. The values of the high- and low-temperature gaps do exhibit a 2-3 percent enhancement after anneal. The change in gap values implies that, by removing the electron donor cations from the system, the Fermi level has been shifted downward in energy and apparently deeper into a band gap. These data suggest the presence of the thermal excitation of carriers from a source in addition to the valence band.

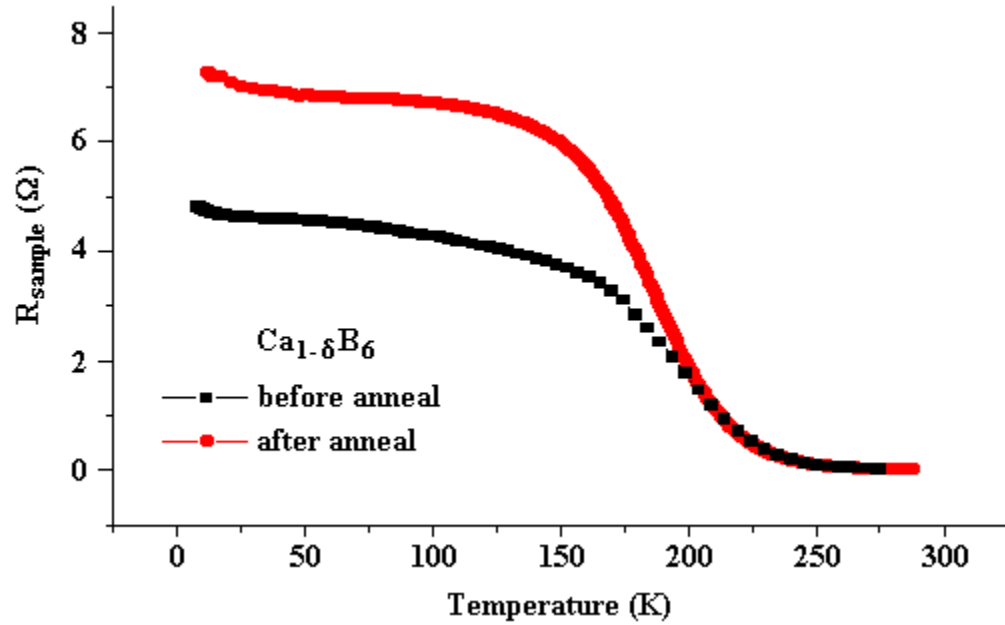


Figure 5-5. Resistance versus temperature in $\text{Ca}_{1-\delta}\text{B}_6$ prior to (black squares) and following (red circles) O_2 anneal.

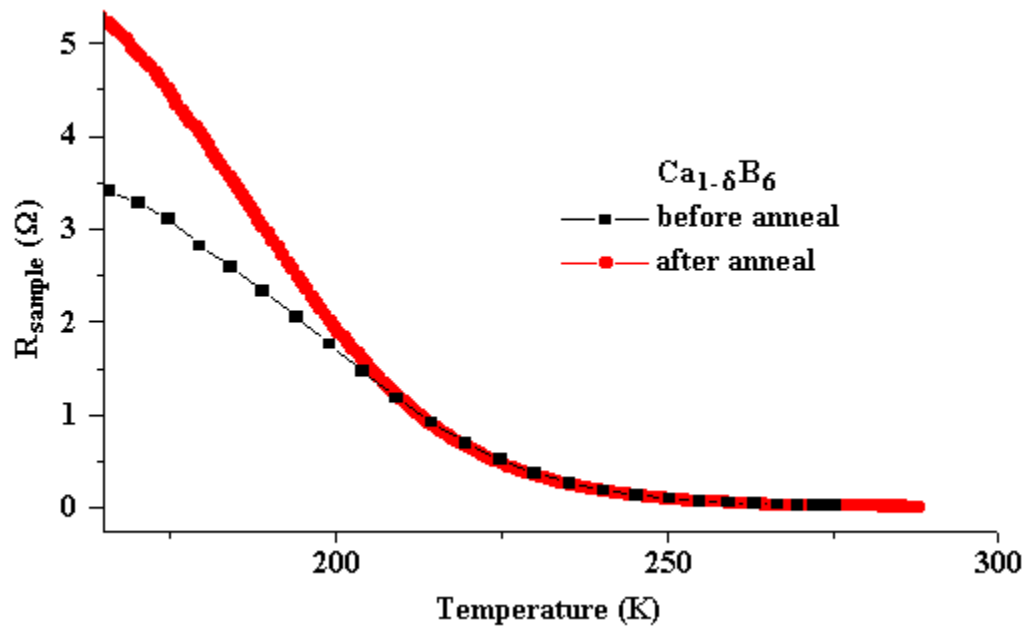


Figure 5-6. High temperature region of Figure 5-5.

5.2 Hall Effect Measurements

A series of Hall effect measurements was performed with the intention of determining not only the sign of the carriers in each doping regime but the carrier concentration as a function of doping level. We initially expected that in the La-doped system the carriers would be electrons, that in the stoichiometric system there would be equal numbers of electrons and holes, and in the Ca-deficient system the carriers would be exclusively holes. The data contradict these expectations but are consistent with the resistivity versus temperature behaviors presented above. A band structure model incorporating this information will be fully developed in chapter 6. An alternative motive of pursuing these measurements was to investigate the possible appearance of the anomalous Hall effect as a signature of ferromagnetism.

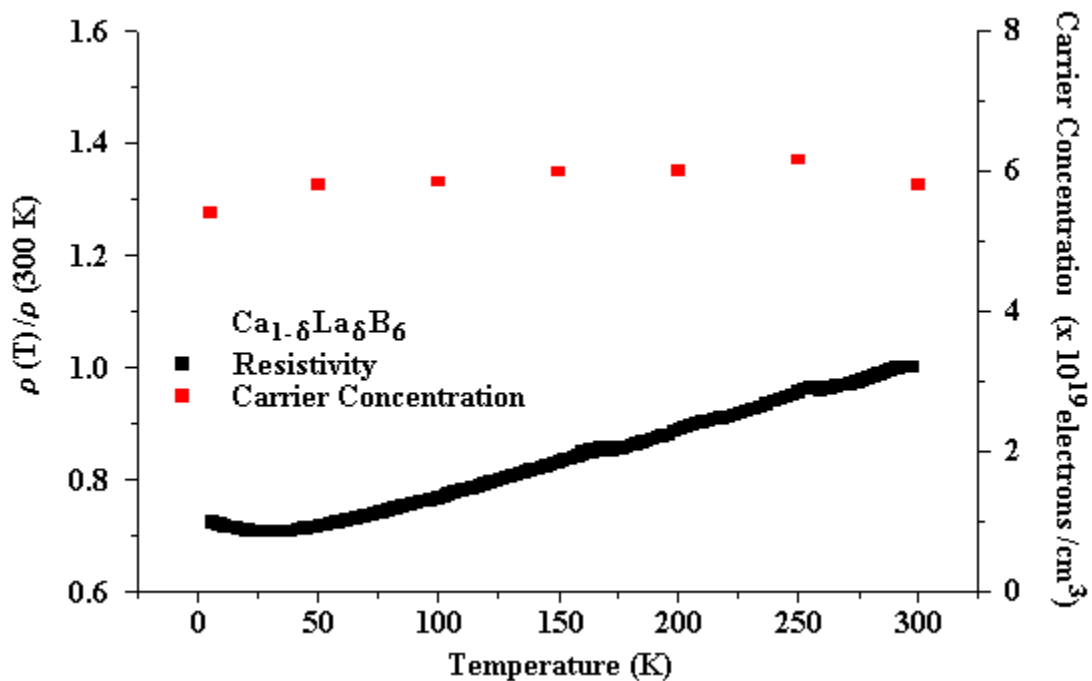


Figure 5-7. Carrier concentration (red) and normalized resistivity (black) versus temperature in $\text{Ca}_{1-\delta}\text{La}_\delta\text{B}_6$.

The Hall effect has been studied as a function of temperature for each of the three doping concentrations. Figures 5-7 through 5-9 display the results of Hall effect measurements in red. The resistivities versus temperature for the same samples are included for comparison and are shown in black. The La-doped material exhibits a carrier concentration of roughly 5×10^{19} electrons/cm³, as seen in Figure 5-7. This electron concentration is approximately independent of temperature, indicating that the conduction electrons reside in the conduction band and are not thermally excited from a band lower than the Fermi level.

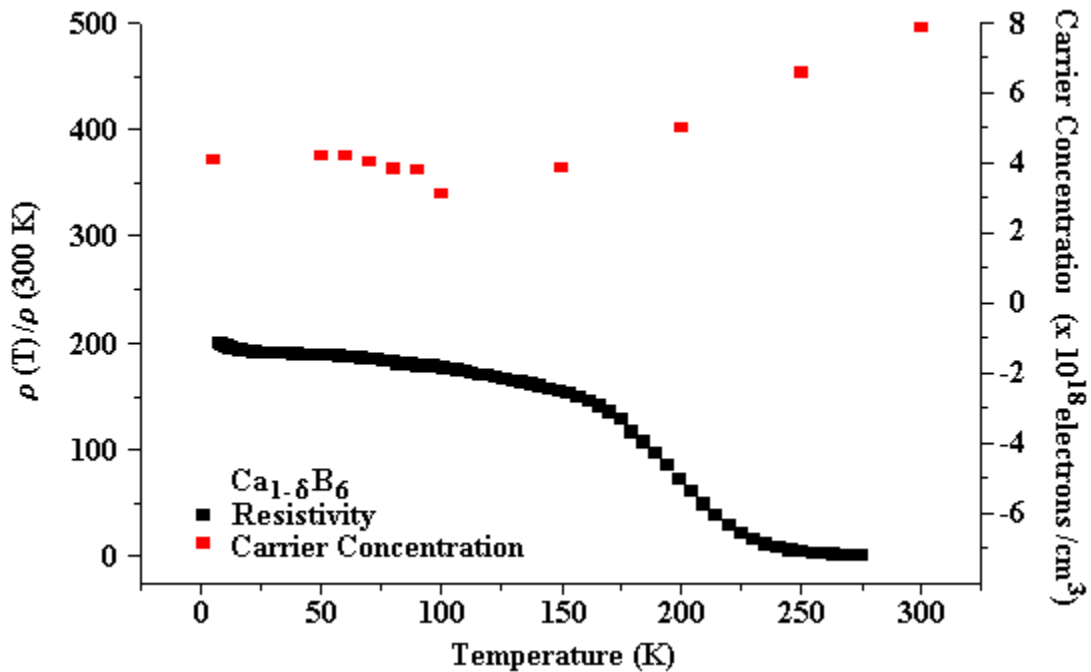


Figure 5-8. Carrier concentration (red) and normalized resistivity (black) versus temperature in $\text{Ca}_{1.8}\text{B}_6$.

Figure 5-8 shows data for the Ca-deficient material, with the carrier concentration shown in red and accompanied by the resistivity in black for comparison. The electron concentration is and is found to be an order of magnitude lower than that seen in the

electron-doped analog. Notice, however, that the Ca-depleted compound retains electron-like carriers. This indicates that the mid-gap position has not been crossed in reducing the Fermi level in energy. The electron concentration is found to decrease in the region of increasing resistivity, as to be expected. As the resistivity levels off, the electron density demonstrates a simultaneous leveling. The concomitant behaviors of resistivity and carrier concentration are consistent with a standard interpretation. Here the increase in resistivity is due to a combination of phonon freeze-out and a reduction in thermally excited electrons about the Fermi level.

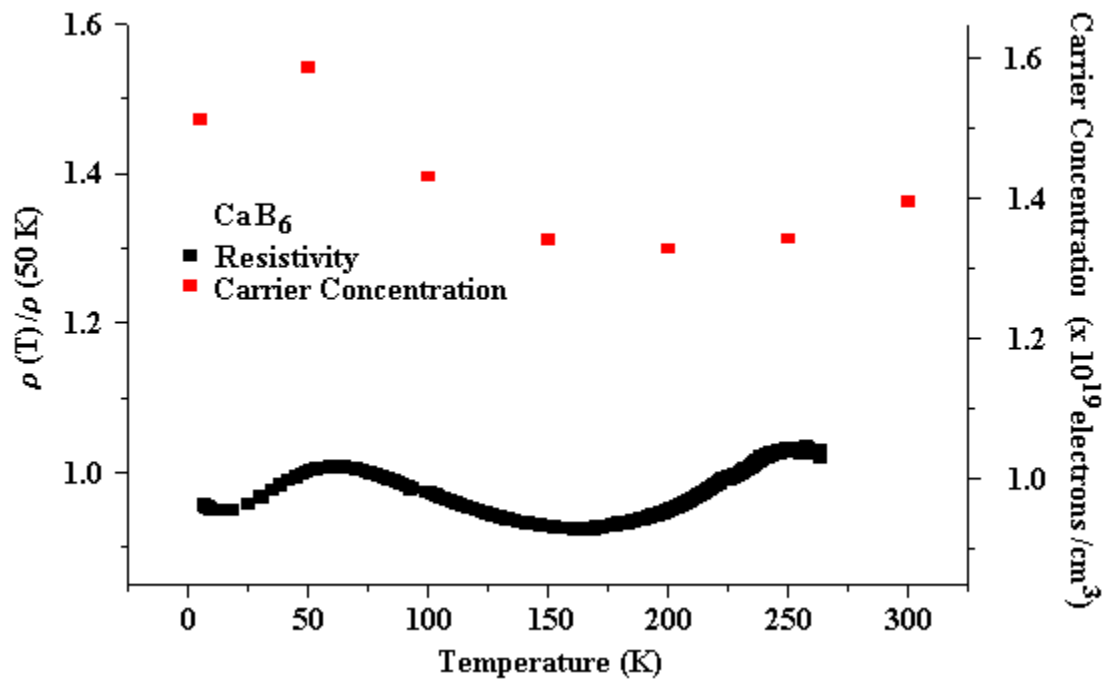


Figure 5-9. Carrier concentration (red) and normalized resistivity (black) versus temperature in CaB_6 .

The stoichiometric material exhibits an interesting behavior in carrier concentration versus temperature, as seen in red in Figure 5-9. The carrier concentration

is found to be approximately 1×10^{19} electrons/cm³. This value agrees with a Fermi level reduced in energy at a reduced electron density with respect to the La-doped system. Interestingly, the behavior of the carrier concentration with temperature mirrors that seen in the resistivity. Because of the low carrier density present in this material, it may be that electron-electron correlations dominate over electron-phonon scattering. Such a scenario might give rise to a directly proportional relationship between resistivity and electron density.

The anomalous Hall effect is a manifestation of spin-dependent scattering and is commonly observed in materials that exhibit long-range ferromagnetic order. In the presence of an external magnetic field, the moments in the solid align accordingly. As a result, the internal magnetic field and associated Lorentz forces acting on the spin-polarized electrons will be field-dependent until the saturation field is attained. The observable result is that the Hall voltage exhibits a hysteresis that mirrors that seen in magnetization.

The possible appearance of hysteresis in the Hall voltage was investigated in an attempt to further verify the presence of long-range magnetic order in CaB₆. The results are shown in Figure 5-10, where an unusual kind of hysteretic behavior is seen. These data were taken on the initial zero-field cool-down of the crystal. With subsequent field sweeps, the effect seems to disappear. Magnetization data on a collection of crystals grown from the same melt but randomly oriented with respect to the applied field are shown in Figure 5-11. The good agreement in saturation field seen in the two independent measurements is convincing that the effect observed in the Hall voltage is not only consistent with but is related to the magnetic state of the material. That the

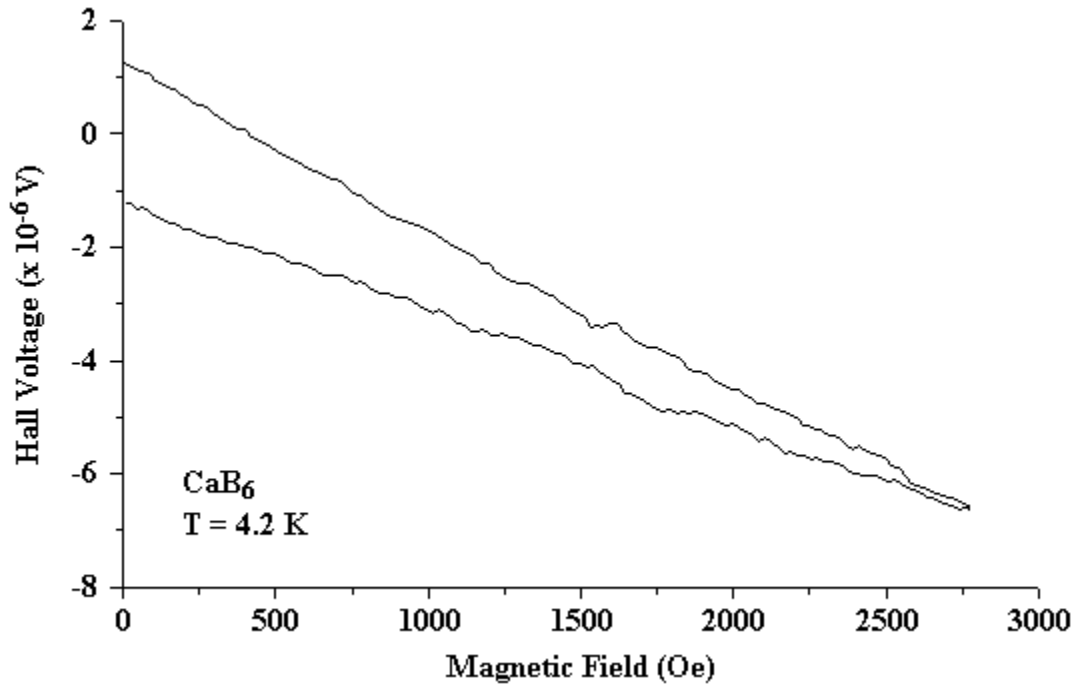


Figure 5-10. Hysteresis in Hall voltage versus magnetic field in CaB_6 at 4.2 K. The saturation field is roughly 2500 Oe, or 0.25 T.

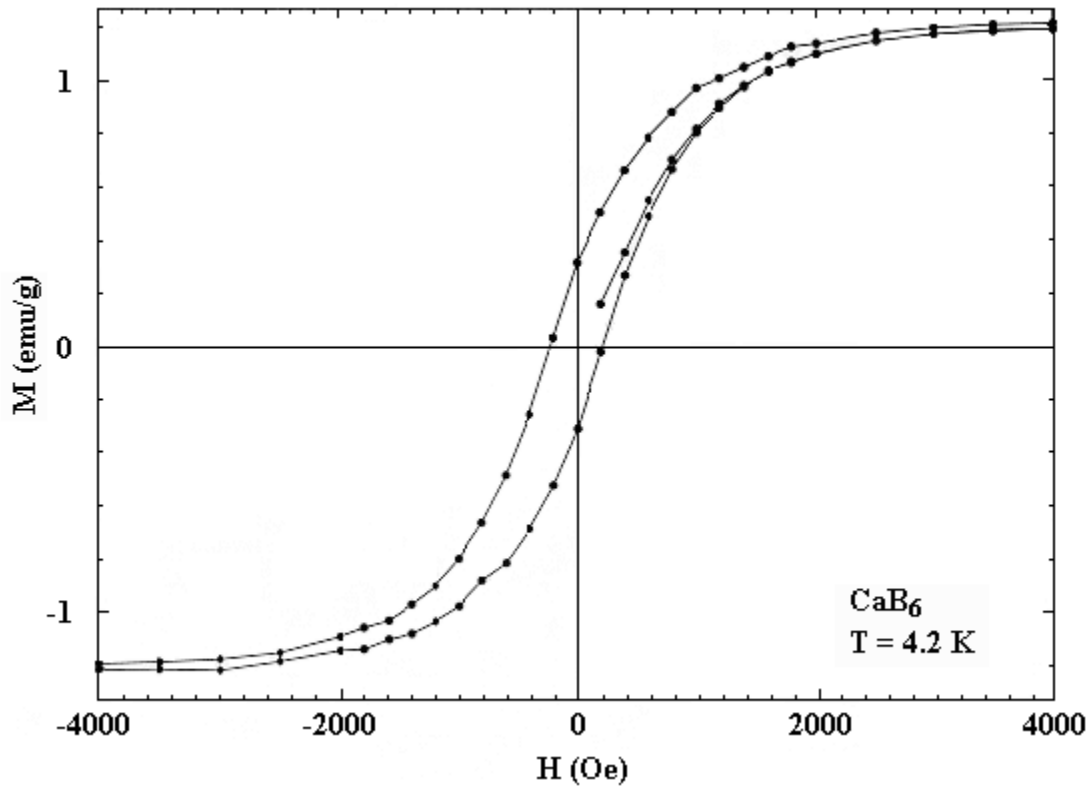


Figure 5-11. Hysteresis in magnetization versus magnetic field in CaB_6 at 4.2 K. The saturation field is roughly 2500 Oe, or 0.25 T (data provided by Bianchi and Fisk).

hysteresis persists in the multi-crystal data may be accounted for by intra-batch non-uniformity arguments. These will be presented in the following chapter.

5.3 Magnetoresistance Measurements

Magnetoresistance measurements can provide a good deal of information about the electronic interactions present within our system. As has been discussed in chapter 3, a typical metal displays a positive H^2 dependence of resistance on magnetic field. Oftentimes, deviations from this behavior can reflect the importance of electron-electron correlations.

In magnetoresistance studies of the CaB_6 system, negative signals were found for all three doping concentrations. In Figure 5-12, magnetoresistance, in terms of fractional change, versus magnetic field is given for La-doped CaB_6 at various temperatures. A small negative magnetoresistance of roughly 0.6% is observed at 5 K, the lowest temperature for which data has been taken, and at a field of 6 T. With increasing temperature, the magnitude of the magnetoresistance begins to diminish, a trend seen in all three materials.

An effect similar in magnitude to that of the La-doped compound is observed in the stoichiometric material, a material that retains some degree of semimetallic nature as suggested by the preceding resistivity and Hall effect data. The magnetoresistance for stoichiometric CaB_6 is shown in Figure 5-13. A maximum effect is observed at 5 K and 6 T of roughly 0.5 %. Again, the signal becomes smaller as the temperature is increased. It is rather noticeable that, at temperatures below 30 K, the electron-doped material

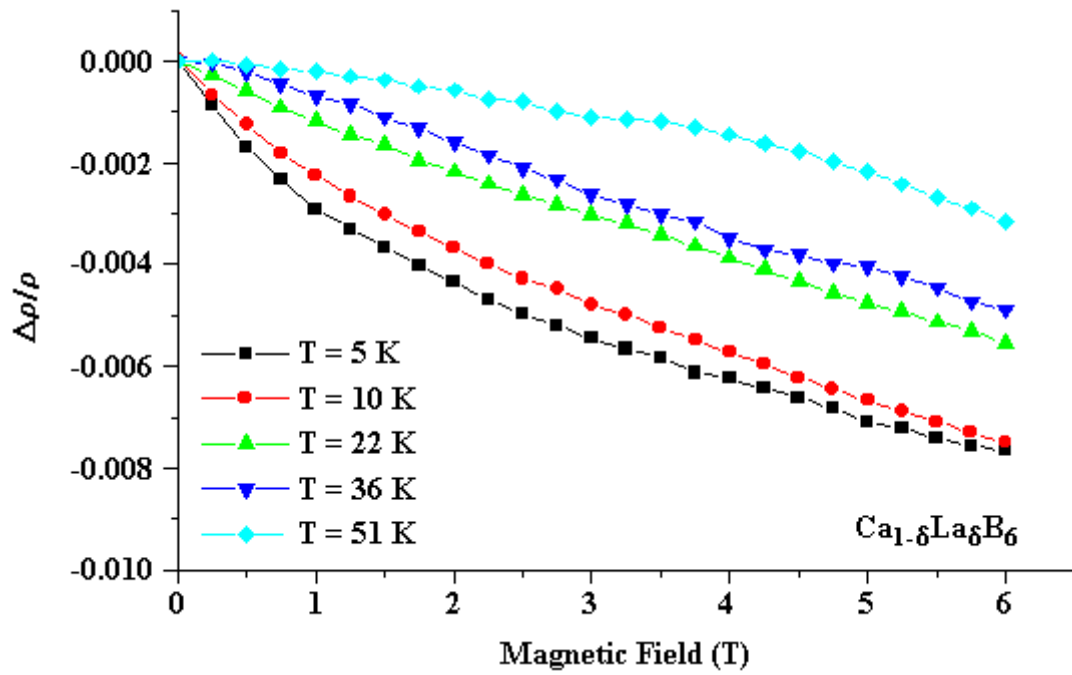


Figure 5-12. Magnetoresistance versus magnetic field in $\text{Ca}_{1.8}\text{La}_{0.2}\text{B}_6$.

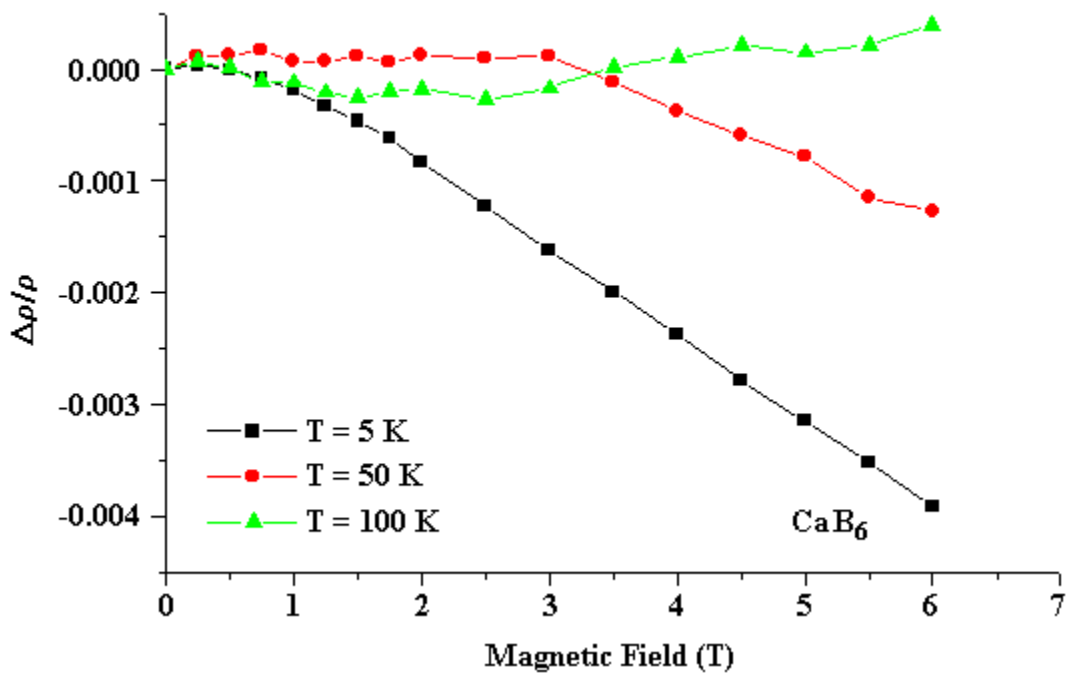


Figure 5-13. Magnetoresistance versus magnetic field in CaB_6 .

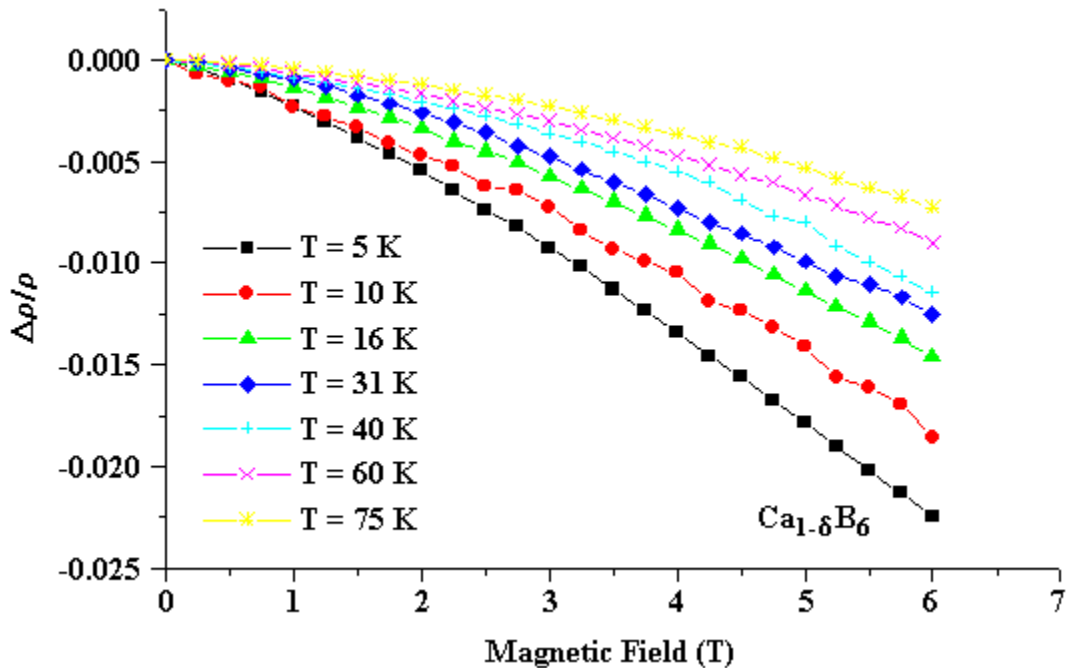


Figure 5-14. Magnetoresistance versus magnetic field in $\text{Ca}_{1-\delta}\text{B}_6$.

exhibits a magnetoresistance of a different functional form than that seen in the stoichiometric compound. This observation will be addressed in chapter 6.

Data for the vacancy-doped compound is shown in Figure 5-14. These data indicate a much larger effect than that seen in the two metallic materials. The maximum value of the negative magnetoresistance at 5 K and 6 T is nearly 2.5%, a signal that is approximately five times larger than that seen in the electron-doped and stoichiometric analogs. The trend of decreasing signal with increasing temperature is preserved in this data set.

5.4 Tunneling Measurements

Tunneling measurements were performed in advance of the transport studies discussed above. The initial goal in undertaking tunneling experiments was to investigate the possible appearance of zero-bias anomalies, in analogy with the features seen in the

spectra of ferromagnetic EuB_6 below its Curie temperature. Additional information provided by these measurements has been influential in the analysis of the $\text{Ca}_{1-\delta}\text{La}_\delta\text{B}_6$ results.

In early measurements, a sharp feature at zero bias in a tunneling spectrum of La-doped CaB_6 was observed at very low temperature, as shown in Figure 5-15. Many external conditions can influence the appearance of these features, including stray magnetic fields, temperature variation, and even the passage of time. Therefore, while the detection of this feature is supporting evidence for ferromagnetism, the data cannot stand alone as a convincing signature of magnetic order. Additionally, it is important to

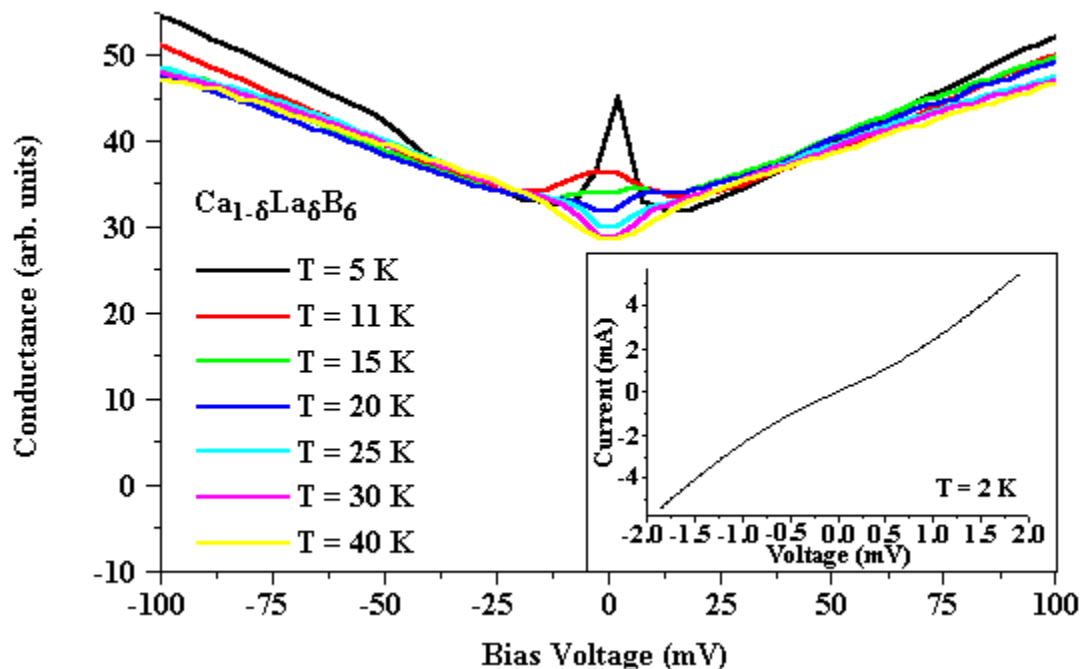


Figure 5-15. Tunneling conductance versus bias voltage in $\text{Ca}_{1-\delta}\text{La}_\delta\text{B}_6$.

note that the I-V characteristic, shown as an inset, appears to be of a lower quality than is typically desired. While it is possible that the conductance peak at zero bias may be

washing out the Pb structure, contributions due to undesirable inelastic transport mechanisms may also be present.

It is also noticeable that the peak diminishes rather quickly with increasing temperature and appears to be completely absent for temperatures above 25 K. Whether this reduction in intensity indicates a transition, magnetic or otherwise, is not definite. These results may be interpreted to be evidence for a second transition well below the T_C of the material that has no bearing on the bulk ferromagnetism. While a double transition is reminiscent of that seen in ferromagnetic EuB_6 , we hesitate to draw parallels between the two systems based on these data.

Subsequent tunneling spectra on additional crystals are shown in Figures 5-16 and 5-17. Figure 5-16 is accompanied by the I-V characteristic in the inset for this particular junction and exhibits a well-defined gap region about zero voltage. In the tunneling conductance, the superconducting Pb gap appears at zero bias for temperatures below $T_c = 7.2$ K. There is an unusual feature in the center of the gap, however. It seems that there may exist a zero bias component to the low-temperature spectra that is unrelated to the superconducting gap. Due to the absence of this feature in the tunneling spectra of Figure 5-17, it is clear that more extensive studies are required to ascertain its origin.

The spectra exhibited in Figure 5-17(a) represent higher temperature behavior and may indicate the formation of a pseudo-gap centered about 22 mV, a feature and energy scale common to many of the previously studied hexaborides. The low-temperature data do not display a clean zero bias peak, as seen previously. There are many maxima in the

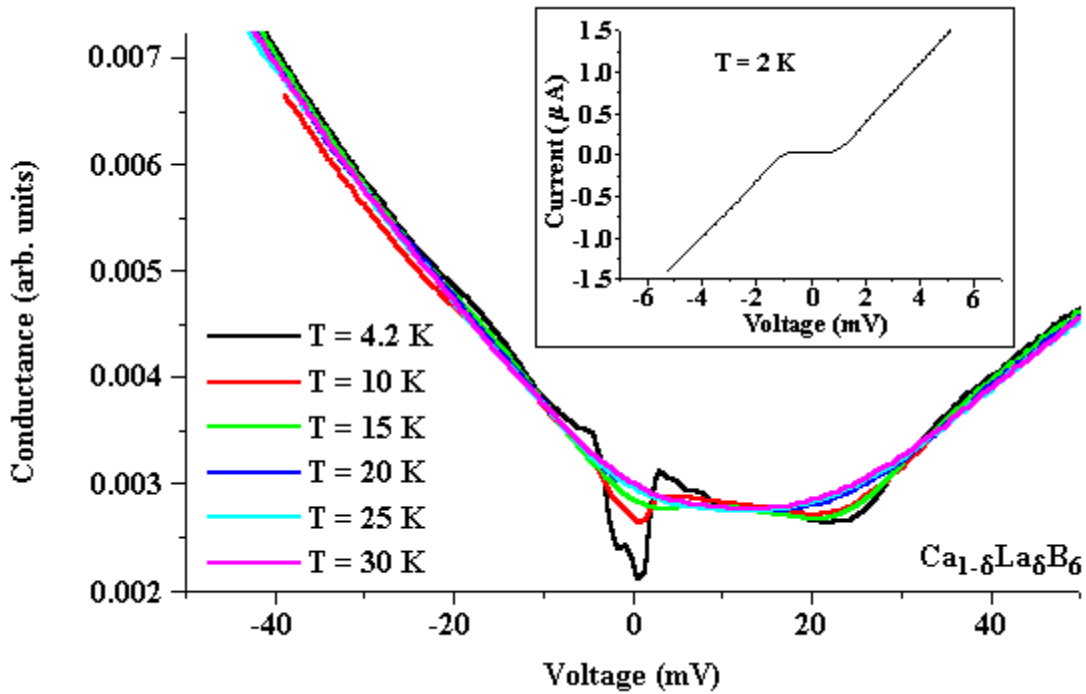


Figure 5-16. Tunneling conductance versus bias voltage in $\text{Ca}_{1-\delta}\text{La}_{\delta}\text{B}_6$.

spectrum at low temperatures, as shown in Figure 5-17(b), but the width and energy scales are rather large to be attributed to a zero bias phenomenon. In the bias range shown, there appear to be features centered about ± 10 , ± 20 , and ± 30 . These features are reminiscent of a system in which some type of inelastic excitation couples to the conduction electrons of the system. A discussion of what these excitations may represent will be given in chapter 6.

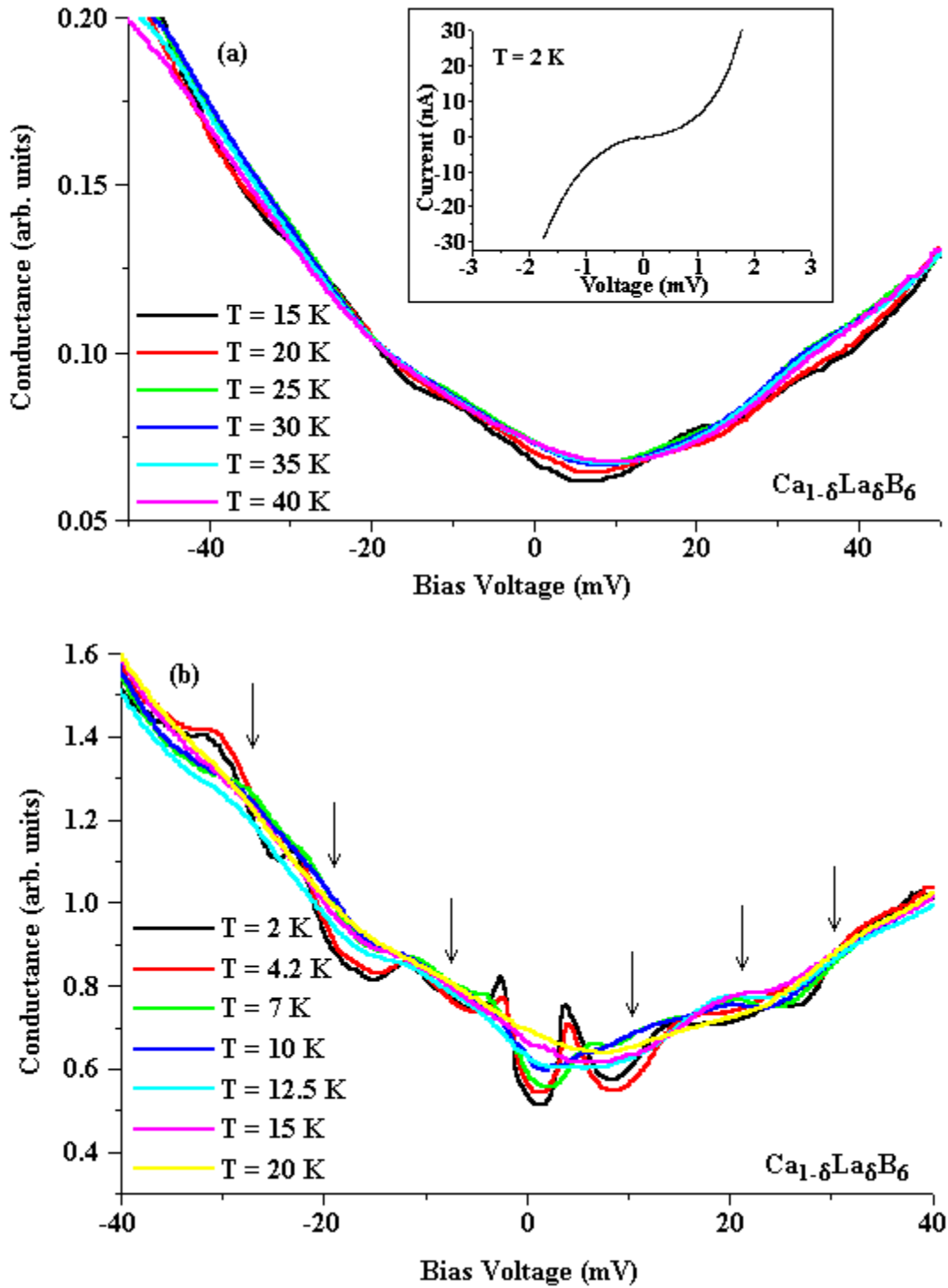


Figure 5-17. Tunneling conductance versus bias voltage in $\text{Ca}_{1-\delta}\text{La}_\delta\text{B}_6$ (a) for $15\text{ K} < T < 40\text{ K}$ and (b) for $2\text{ K} < T < 20\text{ K}$.

CHAPTER 6 INTERPRETATION AND MODELING OF THE DATA

This chapter will serve as the interpretation and conclusion portion of this dissertation. The first section contains an analysis of results. Through reasonable speculation, a simple band structure model involving a gapped band structure with contributions from an impurity band has been developed that is consistent with these observations. A description of the model is given in section 6.2.

6.1 Interpretation of the Data

To formulate a coherent description of the CaB_6 system, an overview of results must be organized. The findings of the transport measurements must be collected and placed in a context. Trends must be identified, and consistency must be achieved. To these ends, the significant results for each quantity studied are summarized below for the CaB_6 system in the three doping concentrations.

6.1.1 $\text{Ca}_{1-\delta}\text{La}_\delta\text{B}_6$

In lightly La-doped CaB_6 , the reduction of resistivity with decreasing temperature suggests metallic behavior to a temperature of 28 K. These data imply that the Fermi level has been raised in energy by the presence of additional electrons so that it crosses the conduction band and induces metallic behavior, at least at high temperatures. At lower temperatures, there is a resistive minimum and a subsequent crossover to non-metallic behavior. Possible origins of this low-temperature rise in resistivity are discussed below.

The carrier concentration is consistent with the metallicity observed in the resistivity. For a doping level of 0.5% of a trivalent cation into a divalent matrix with a much lower electron density, the value of the carrier concentration should roughly correspond to one conduction electron per 200 unit cells. One electron per unit cell gives approximately 10^{22} electrons/cm³, so that 1 electron per 200 unit cells gives 5×10^{19} electrons/cm³, in good agreement with the Hall effect results presented in Figure 5-7. Additional carrier concentration may accompany impurities or defects in the crystal, but this density is expected to be a small correction to that arising from the intentional La doping.

The lack of significant temperature dependence in the carrier concentration data indicates that these dominant electrons are native to the conduction band, as opposed to being thermally excited from a lower-lying band. Our observations support the intended effect for the electron-doped material; the Fermi level appears to cross the upper band.

In a typical metal, resistivity at high temperature is expected to be linear, as is seen in $\text{Ca}_{1-\delta}\text{La}_\delta\text{B}_6$. At low temperatures, saturation is expected to occur with T^5 -dependence, representing a combination of electron-phonon scattering, which is of the form T^3 , and small-angle electron-electron scattering, which is of the form T^2 . Verification of these low-temperature behaviors is thwarted by the resistive minimum that appears at approximately 28 K. The small minimum in the resistivity of the La-doped CaB_6 at low temperatures has not been identified, but such a feature can be produced by several mechanisms. The focus here will be on three possible scenarios: a lattice distortion, weak localization, and the Kondo effect.

A change or distortion of the lattice, such as may be associated with a Jahn-Teller distortion, can induce semiconducting behavior, if the Fermi level of the material is in close proximity to the bottom of the gap [78]. This transition would be second order and does not require the presence of significant electron-electron correlations to occur. If electronic correlations are substantial, both weak localization and the Kondo effect can produce a minimum in resistivity versus temperature.

In consideration of the possible band structure transition, a potential mechanism may be a Jahn-Teller-like distortion, as has been seen in several other magnetic hexaborides [79,80]. With expansion of the lattice, even if directionally asymmetric, a change in the band structure relative to the Fermi level can occur. When the Fermi level crossing is reduced or eliminated, an increase in resistivity can follow. Physical explanations for this phenomenon include the reduced overlap of carrier states associated with adjacent ions and an effective decrease in carrier number per unit cell.

Weak localization is a consequence of elastic scattering mechanisms present in a solid. Quantum mechanics predicts that, in maneuvering around an arrangement of elastic scattering centers, there are many possible electronic paths. This phenomenon preserves the phase of the electronic wavefunction and can give rise to interference effects and an effective reduction in the mobility of the charge carriers. An increase in sample resistance accompanies weak localization at low temperatures and is typically observable in materials with minimal screening, that is, where the electron density is very low. Low temperatures and low carrier concentrations are required because the interference effect associated with weak localization is destroyed by excessive inelastic scattering events, such as inelastic electron-electron scattering and electron-phonon

scattering. It is interesting to note that, under the conditions of weak localization, inelastic scattering actually has the potential to increase the conductivity of a material as it destroys the phase coherence of the carrier wavefunction.

Predictions made by Altshuler and Aronov [81,82] indicate that electron interaction effects can induce localization in three dimensional systems with finite disorder. At low temperatures, the conductivity is proposed to behave with a correction term proportional to the square root of temperature, as shown in Equation (6-1):

$$\sigma(T) = \sigma_0 \left[1 + \frac{\alpha}{k_F l} \left(\frac{kT\tau}{\hbar} \right)^{1/2} \right], \quad (6-1)$$

where α is a constant that can be positive or negative, k_F is the Fermi wavevector, l is the mean free path, and τ is the elastic scattering time. Figure 6-1 shows normalized conductivity versus the square root of T for $\text{Ca}_{1-\delta}\text{La}_\delta\text{B}_6$. The temperature range that has been used in the fit is shown as the upper axis. The fit turns out to be reasonable. The intercept of the linear fit is given by the value of the conductivity extrapolated to zero temperature. From the fit and using $200 \text{ } \Omega^{-1}\text{-cm}^{-1}$ as an estimate of the conductivity at 300 K using typical crystal dimensions, the value of σ_0 is roughly $135 \text{ } \Omega^{-1}\text{-cm}^{-1}$.

Further comparison to Equation (6-1) can yield an estimate of the mean free path. Using the approximations that $\alpha \sim 1$, $l/\tau \sim v_F$, and $m \sim m_e$, and by taking the value of the Fermi energy to be 0.062 eV [60], the mean free path is found to be roughly 5 microns. This result is consistent with predictions that the hexaborides are typically clean systems. We verify that this second term is truly a correction in that $k_F l \sim 10^4$, and consequently much larger than unity. While Fermi liquid theory enhances the effective carrier mass, which is proportional to the square of the mean free path but not accounted for in this

calculation, this mass correction may be compensated to some extent by a smaller value of α (see the magnetoresistance calculation below based on weak localization predictions).

There are several reasons to suspect that weak localization theory may be unsuitable for application toward the single crystal hexaborides. The first hint of incompatibility is seen in the comparison of single-crystal CaB_6 with other systems in which weak localization is known to occur. These are highly disordered systems, such as P- and Nb-doped Si and Au-Pd thin films [82], containing many elastic scattering sites. High disorder is unexpected for the CaB_6 compound, even with the anticipation of defects. The theory of Altshuler and Aronov, however, appears to be fairly consistent

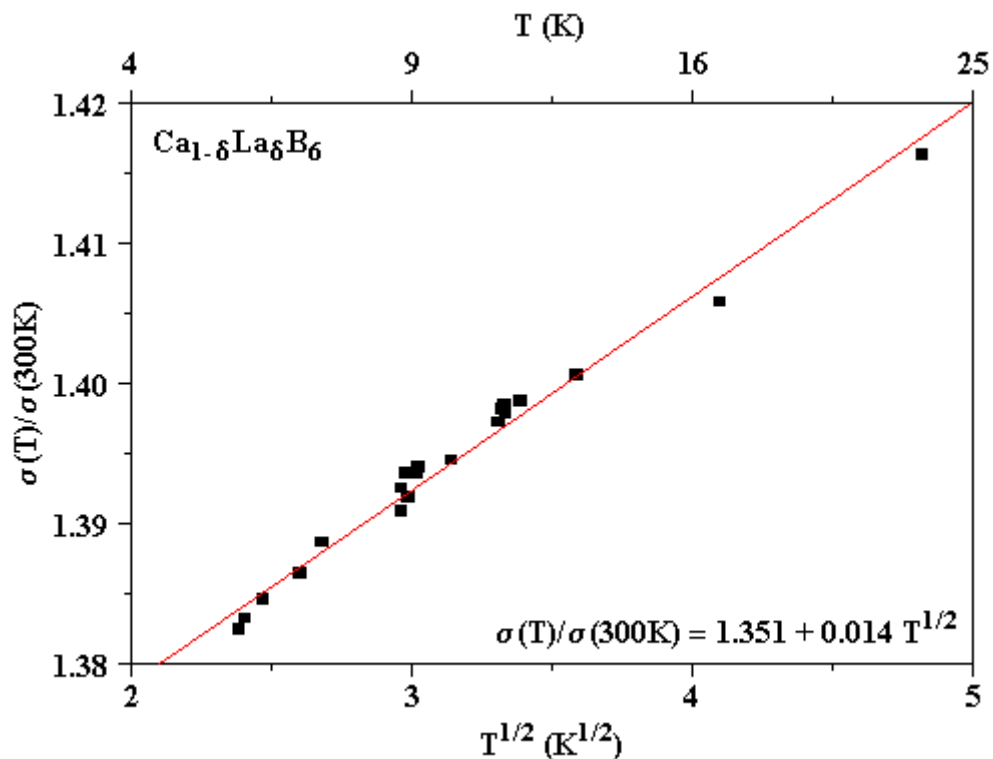


Figure 6-1. Normalized conductivity versus $T^{1/2}$ in $\text{Ca}_{1-\delta}\text{La}_{\delta}\text{B}_6$ for $5 \text{ K} < T < 24 \text{ K}$.

with our experimental results, indicating that disorder may play a role in the low-temperature properties of the La-doped material and may even indicate a degree of disorder introduced to the system by a structural transition.

An alternate effect known as the Kondo effect can also produce a minimum and subsequent increase in resistivity with decreasing temperature. Kondo-like behavior occurs in the presence of a dilute concentration of magnetic impurities. The electron gas couples to the magnetic impurities through the Ruderman-Kittel-Kasuya-Yosida (RKKY) interaction, where Friedel-like oscillations in the type of coupling, ferromagnetic or antiferromagnetic, form radially in the space around the ion. Through the conduction electrons, the magnetic ions interact with each other indirectly. The resistance minimum occurs at low temperatures due to scattering by the exchange coupling, which effectively localizes conduction electrons around the magnetic ions [83].

The Kondo theory provides a prediction of the form of resistivity versus temperature, as shown in Equation (6-2). At high temperature, the resistivity is dominated by the normal T^5 contribution. At low temperatures, a competition ensues between the T^5 dependence and the Kondo contribution, which is of the form $\ln T$ for a three-dimensional system.

$$\rho = aT^5 + c\rho_0 - c\rho_1 \ln T, \quad (6-2)$$

where c is the concentration of the magnetic impurity,

ρ_0 is a measure of the exchange scattering,

and $\rho_1 = 3zJ/\varepsilon_F$ (z = number of nearest neighbors and

J is the exchange constant).

Figure 6-2 shows a plot of normalized resistivity versus $\ln T$ from 5 K to approximately 28 K. The experimental results are shown in black, while a fit to Kondo behavior is shown in red. For the temperature range plotted, the agreement appears to be reasonable. By calculating a rough estimate of the resistivity at 300 K to be 10 m Ω -cm, using approximate crystal dimensions, we find that $\rho_1 = 0.011 * 10 \text{ m}\Omega\text{-cm} = 0.11 \text{ m}\Omega\text{-cm}$ (see Kondo fit in Figure 6-2). We can infer from this modeling procedure a measure of the exchange energy in the case that the Kondo model is relevant to this material. By taking the Fermi energy to be 0.062 eV, the magnetic impurity concentration to be 0.005, and the number of nearest neighbors for this cubic crystal to be 6, an approximate value

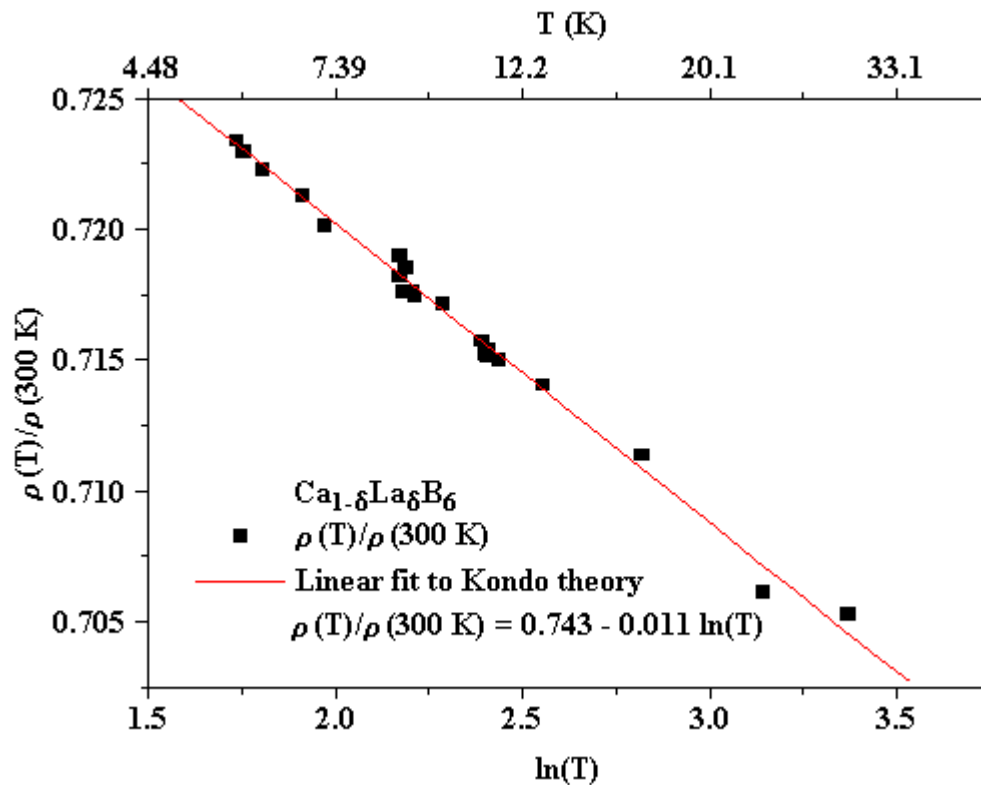


Figure 6-2. Normalized resistivity versus $\ln T$ in $\text{Ca}_{1-\delta}\text{La}_\delta\text{B}_6$ for $5 \text{ K} < T < 28 \text{ K}$. A fit to linear behavior is displayed in red and represents the behavior predicted by Kondo theory.

of J is determined to be 70 meV. In temperature, 70 meV corresponds to roughly 700 K, a figure not far from the reported T_C of this material.

It is important to emphasize that the Kondo effect is typically incompatible with the presence of ferromagnetic order. This observation seems to provide two possible scenarios for this material that are mutually exclusive. For a compound that is truly ferromagnetically ordered, we would be obliged to abandon this model in favor of a mechanism that can coexist with long-range order. If the La-doped material is actually well described by the Kondo picture, the presence of disordered local magnetic moments is implied. In conjunction with the recent theoretical prediction that magnetic moments may be associated with B_6 vacancies or substitutions with Ca, as described in chapter 2, the suggestion of a Kondo state is a consistent one, provided they are disordered. This second possibility may constitute further evidence for non-uniform sizes and distributions of moment-carrying defect pockets, in which superparamagnetic or paramagnetic behavior is possible in place of ferromagnetism, the proposals of which were discussed in chapter 2.

A few important caveats regarding these suggestive models should be noted. First, it should be recognized that $\ln T$ behavior could arise from mechanisms other than the Kondo effect. These other mechanisms are governed by electron correlation effects and, as it is not clear that they are necessarily related to this system, have been omitted from the discussion here. It is also essential to note that, due to the narrow range in temperature over which these fits have been performed, the agreement to the models discussed above only suggests a particular mechanism. The fits cannot be considered to be conclusive.

In the magnetoresistance observed in the La-doped compound, the curvature changes sign at a temperature near 28 K, suggestive of a correlation between this effect and the minimum in resistivity versus temperature. It was seen in the results presented in Figure 5-12 of chapter 5 that at 22 K and below, the curvature of the data is positive, while at temperatures greater than 36 K, the curvature becomes negative in sign.

Deviations from positive H^2 magnetoresistance suggest a more complex electronic environment than a simple free-electron model. Here we consider mechanisms that can produce a negative magnetoresistance, including the Kondo effect, weak localization where spin-orbit scattering is negligible and an alternate mechanism in which a decrease in resistivity can be produced due to band shifting at the Fermi level in the presence of a magnetic field.

At temperatures below T_K , at which the Kondo minimum in the resistivity occurs, Kondo theory predicts a negative power law behavior in magnetoresistance versus magnetic field. Monod [84] determined the field dependence of the resistivity to be approximately $\rho \sim -H^n$, where $n \approx 1.7$ to 1.8. This functional form, however, gives a negative curvature for magnetoresistance versus temperature, which is contradictory to our findings. We therefore assert that the Kondo effect is most likely not the mechanism driving the 28 K transition in $\text{Ca}_{1-\delta}\text{La}_\delta\text{B}_6$.

In the presence of weak localization in three dimensions and where spin-orbit scattering is sufficiently weak, we expect the quantity $\Delta\rho/\rho^2$ to behave as $-\sqrt{H}$ [85]:

$$\frac{\Delta\rho}{\rho^2} = -\beta \frac{0.605}{2\pi^2} \frac{e^2}{\hbar} \left(\frac{eH}{\hbar} \right)^{1/2} \quad (6-3)$$

Experimental data are shown for $\text{Ca}_{1-\delta}\text{La}_\delta\text{B}_6$ in Figure 6-3, where the 5 K data are

explicitly fit to the weak localization model (shown in solid red). The qualitative agreement between experiment and theory is good at the lowest temperatures, while the data tend to deviate from $-\sqrt{H}$ as the temperature is increased. From this fit, we can estimate the value of β as defined in Equation (6-3), which is unity for free electrons. This calculation reveals the value of β to be roughly 5×10^{-5} , an unexpectedly low figure that indicates either an overwhelmingly detrimental contribution from electron correlations or the inapplicability of weak localization theory in this form to the low-temperature behavior of the La-doped system.

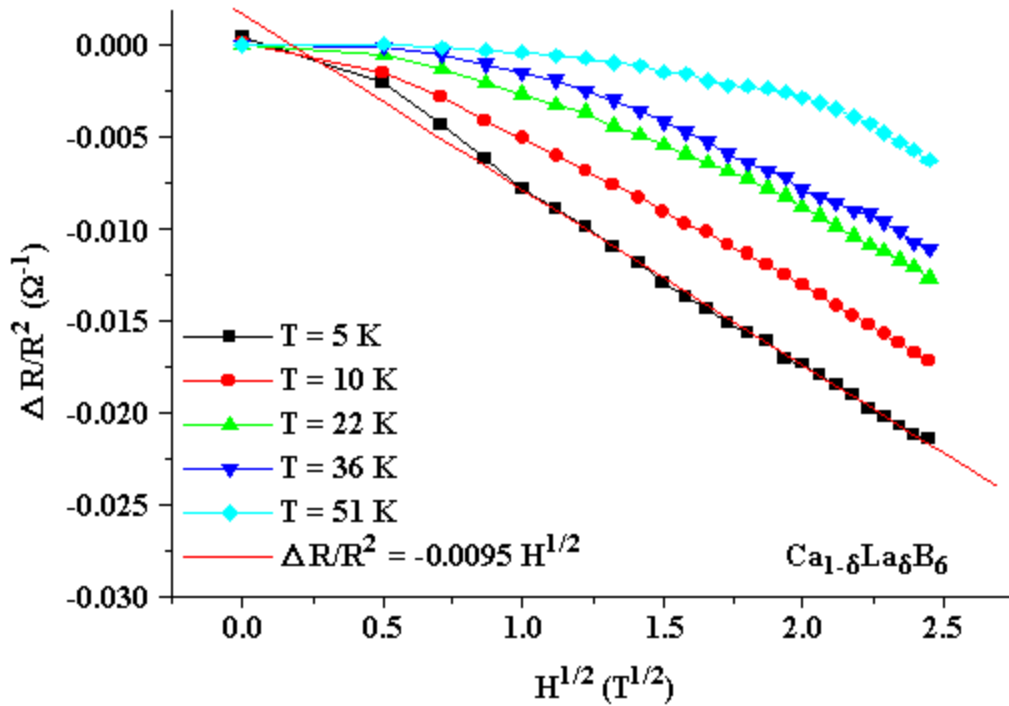


Figure 6-3. $\Delta R/R^2$ versus $H^{1/2}$ in $\text{Ca}_{1-\delta}\text{La}_\delta\text{B}_6$.

A relevant mechanism for the negative magnetoresistance appearing in this material may also lie in the proximity of its electron transport properties to the

semiconducting state. The overlap of the Fermi level near the minimum in the conduction band implies that a negative contribution may result from externally induced paramagnetic splitting of the conduction band, enhancing the conductivity for a majority spin band and reducing the sample resistance by a small but finite amount. The ratio of the band splitting induced by an external field to the Fermi energy can give us a prediction of the magnetoresistance we would expect from such a paramagnetic splitting in a semimetallic material.

A simple calculation, based on the Drude model of conductivity in a metal, can be performed for comparison to the experimental data. This is done below (see Equations (6-4) through (6-6) and Figure 6-4) for the other semimetallic compound CaB_6 , whose magnetoresistance is not complicated by a low-temperature transition like that occurring at 28 K in this material. The value obtained for CaB_6 , however, is expected to be roughly applicable to both materials because of their similarity in electronic environments.

Limited tunneling studies, as shown previously in Figure 5-15, support the finding that La-doped CaB_6 exhibits ferromagnetism, with the appearance of a ZBA-like feature, in analogy with EuB_6 , in the early tunneling spectra at low temperatures. Subsequent tunneling results have been shown in Figures 5-16 and 5-17, with the I-V characteristic included in the inset. The zero bias peaks seen in previous spectra are not convincingly present in these data. Owing to the sensitivity to external influences, such as remnant magnetic field or cooling rate, the later data may reflect dissimilarity in environment, compared to that of the previous junction. It must also be noted that the later spectra were taken with an x-y plotter, while the early data were recorded digitally using a programmable voltage source and a Lab View program. The voltage resolution of the

analog technique was typically higher than in the digital technique, owing to a component of human error, which may indicate that data taken with the x-y plotter are higher quality.

Significant to the later tunneling results are features that appear to be inelastic peaks at bias voltages between ± 10 and ± 30 meV. The features occur at energies characteristic of phonons, but this identification is simply speculative. The reduction of intensity with increasing temperature, accompanied by the near-disappearance of these peaks around 25 K contributes to the conclusion that there is a transition occurring in the vicinity of this temperature in $\text{Ca}_{1-\delta}\text{La}_\delta\text{B}_6$.

The transition temperature observed in these data for the electron-doped CaB_6 is too low to be associated with the ferromagnetism. One self-consistent description of a transition that may give the transport behavior presented in this work is that of a Jahn-Teller-like structural distortion. It is conceivable that, upon distortion of the lattice, certain phonon modes are lowered in energy and couple more effectively to the density of states. The phonon scattering mechanism is consistent with the energies at which peaks appear in the tunneling spectra, as well as the symmetry in the features about zero bias voltage. It is important to acknowledge, however, that although this work provides evidence for the identification of the excitations as phonons, the assertion is only speculative.

6.1.2 Stoichiometric CaB_6

Because of the comparatively high electron density and the absence of clearly activated transport behavior, we conclude that the stoichiometric CaB_6 exhibits marginal metallicity in place of expectations of semiconductivity. The Fermi level in this compound is expected to cross the conduction band at a position very close to the band

minimum, and we find that a high-temperature region appears to be discrete from a low-temperature region.

Because the Fermi level lies in very close proximity to the conduction band edge in the stoichiometric sample, it may be that subtle features of and near the conduction band account for the complex form of the resistivity as a function of temperature. For example, the effects of a small splitting of the conduction band or the existence of an impurity band might significantly influence the transport properties in this material.

The carrier concentration is found to be nearly an order of magnitude lower than what is observed in the electron-doped compound. This result is consistent with a reduction in Fermi level accompanying the lack of trivalent La. The observation that the carriers are electrons, accompanied by the moderate electron density, verifies that in this stoichiometry, the material is not of a semiconducting nature.

Paramagnetic splitting of the conduction band in magnetic field may be the origin of the negative magnetoresistance in this material. In a field of 6 T, the paramagnetic shifts of the opposite spin components of the conduction band are expected to be small, only marginally increasing the density of states at the Fermi level for one spin band and reducing it equally subtly for the other.

Using the simple Drude model to estimate the change in conductivity in the limit of zero temperature and governed by the relations

$$\begin{aligned}
 \varepsilon &= \frac{\hbar^2 k^2}{2m} \\
 &= \frac{\hbar^2}{2m} (3\pi^2 n)^{2/3} \\
 &= \frac{\hbar^2}{2m} \left(3\pi^2 \frac{\sigma m}{e^2 \tau}\right)^{2/3}, \tag{6-4}
 \end{aligned}$$

we can solve for the magnetoconductance using

$$\frac{\sigma - \sigma_0}{\sigma_0} = \left(\frac{\varepsilon_{\uparrow}^{3/2} - \varepsilon_0^{3/2}}{\varepsilon_0^{3/2}} \right) + \left(\frac{\varepsilon_{\downarrow}^{3/2} - \varepsilon_0^{3/2}}{\varepsilon_0^{3/2}} \right), \quad (6-5)$$

where

$$\left. \begin{array}{l} \varepsilon_{\downarrow} \\ \varepsilon_{\uparrow} \end{array} \right\} = \varepsilon_F \pm \mu_B H$$

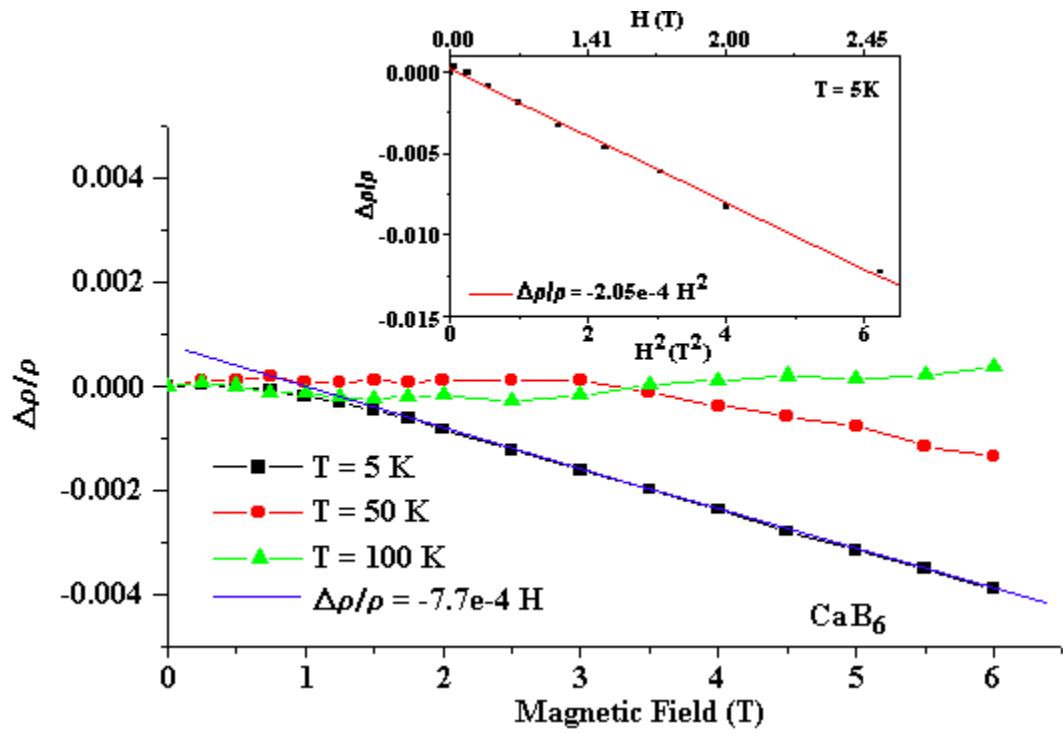


Figure 6-4. Magnetoconductance in CaB_6 versus H with fit to linear for $2 \text{ T} < H < 6 \text{ T}$. Inset shows magnetoconductance versus H^2 for $0 \text{ T} < H < 2.5 \text{ T}$.

Finally, we obtain

$$\begin{aligned} \frac{\Delta\sigma}{\sigma_0} &= \frac{(\varepsilon_F + \mu_B H)^{3/2} - \varepsilon_F^{3/2}}{\varepsilon_F^{3/2}} + \frac{(\varepsilon_F - \mu_B H)^{3/2} - \varepsilon_F^{3/2}}{\varepsilon_F^{3/2}} \\ &= \left(1 + \frac{\mu_B H}{\varepsilon_F} \right)^{3/2} + \left(1 - \frac{\mu_B H}{\varepsilon_F} \right)^{3/2} - 2 \end{aligned} \quad (6-6)$$

We obtain a result that, at very small fields, depends quadratically on magnetic field. With a Fermi level located very near the bottom of the conduction band, one band will become dominant at higher fields, while the Fermi level overlap with the other is suppressed, thus giving linear dependence on the magnitude of the field. At much higher fields, the $H^{3/2}$ behavior will become apparent. These are fields not attained in our magnetoresistance studies, since for $\mu_B H/\epsilon_F$ to be of the order of unity, $H \sim 10^3$ T. The results presented in this work are confined to a maximum field of 6 T and remain within the linear regime at the highest fields, where one spin band dominates over the other.

We can calculate a zero-temperature estimate of the intermediate field magnetoresistance in CaB_6 . Using the values $\epsilon_F = 0.062$ eV and $\mu_B = 5.8 \times 10^{-5}$ eV/T, an effect of roughly 0.75% can be expected at a field of 6 T. This result is in moderately good agreement with the 0.4% effect seen at 5 K, as shown in Figure 5-13 of the preceding chapter.

The magnetic field dependences described by the band shifting calculation performed above (see Equations 6-4 through 6-6) can be tested against experimental results. This is done in Figure 6-4, which shows magnetoresistance versus H^2 for small field in part (a) and magnetoresistance versus H for moderate field in part (b).

We next investigate the prefactors of the low-field H^2 and high-field H dependencies of magnetoresistance at low temperature. In Figure 6-4(a), the coefficient of the H^2 dependence is found to be $-2.05 \times 10^{-4} \text{ T}^{-1}$. From the calculation, we expect this value to approximate the quantity $-(\mu_B/\epsilon_F)^2 = -10^{-6} \text{ T}^{-1}$. It appears that the calculation is an underestimate of the experimental findings by two orders of magnitude. The origin of

this discrepancy has not been identified, but the qualitative success of the low field fit merits consideration.

The high-field calculation predicts the slope of magnetoresistance versus field to be $-(\mu_B/\varepsilon_F) = -10^{-3} \text{ T}^{-1}$. The theoretical value is adequately close to our experimental findings, the linear fit of which gives a prefactor of $-7.7 \times 10^{-4} \text{ T}^{-1}$ (Figure 6-4(b)), that we consider this simple Drude-based theory to be a good approximation to the physics described by these magnetoresistance measurements.

It is interesting to note that if there are conduction electrons at the Fermi level in this material, there is no significantly distinguishing characteristic between this very lightly doped semiconductor and the La-doped CaB_6 at temperatures above 28 K. Consequently, the ferromagnetism generated in $\text{Ca}_{1-\delta}\text{La}_\delta\text{B}_6$ may also appear in this material with a significantly diminished moment, as inferred by other workers [39]. Supporting data lies in the hysteresis seen in the Hall voltage versus magnetic field results for CaB_6 , in which the saturation field is in excellent agreement with that acquired from magnetization versus field measurements, as shown in Figures 5-10 and 5-11 in the preceding chapter.

6.1.3 $\text{Ca}_{1-\delta}\text{B}_6$

The semiconducting transport that is expected in CaB_6 instead appears in the Ca-deficient compound. In order to ascertain the validity of this finding, a post-growth anneal procedure enabled the further depletion of Ca in a single crystal. The comparison of the resistivities before and after the annealing process indicates that the value of the gap had been measurably increased. This data supports the hypothesis that it is the Ca-

deficient material that is semiconducting, and with further Ca depletion, the material approaches a mid-gap Fermi level.

There are data that suggest that the semiconducting nature of this material is unconventional. This is shown in Figure 6-5, which depicts Hall mobility versus temperature. These data were calculated by taking the ratio of Hall coefficient to the resistivity. This plot indicates that the mobility is temperature-dependent, judging by the large deviation occurring at room temperature. In the absence of scattering, the mobility of a simple semiconductor does not depend on temperature. To see this, it is necessary to analyze the temperature dependences of the Hall coefficient and the resistivity. The Hall coefficient is known to follow the form of $1/n$, which to first order, exhibits a temperature dependence $1/\exp(-\Delta/kT)$, giving $R_H \propto \exp(\Delta/kT)$. Meanwhile, the resistivity follows the form $\rho \propto \exp(\Delta/kT)$. When the ratio of the two quantities is formed, the exponentials cancel, giving a temperature-independent mobility.

Including the effect of scattering events adds temperature dependence to the Hall mobility. One type of temperature dependence can be associated with phonon freeze-out, which would give an increase in mobility with decreasing temperature. Scattering mechanisms associated with defects tend to lower the mobility with decreasing temperature. The temperature dependence seen in $\text{Ca}_{1-\delta}\text{B}_6$ may be due to a combination of factors. At high temperatures, we find a mobility that is reduced with decreasing temperature, indicating the presence of defects, possibly in the form of Al inclusions, B_6 vacancies, or anti-site substitutions. Judging by the temperature at which the mobility is suppressed, such a defect density would be unexpectedly high, but this remains a possibility in light of recent proposals that defects are present. In the low temperature

region, the mobility appears to be increasing with decreasing temperature, as shown in the inset of Figure 6-5, indicating that phonon freeze-out may dominate in this regime. Higher resolution data at all temperatures are desirable to determine the reproducibility of these temperature dependences.

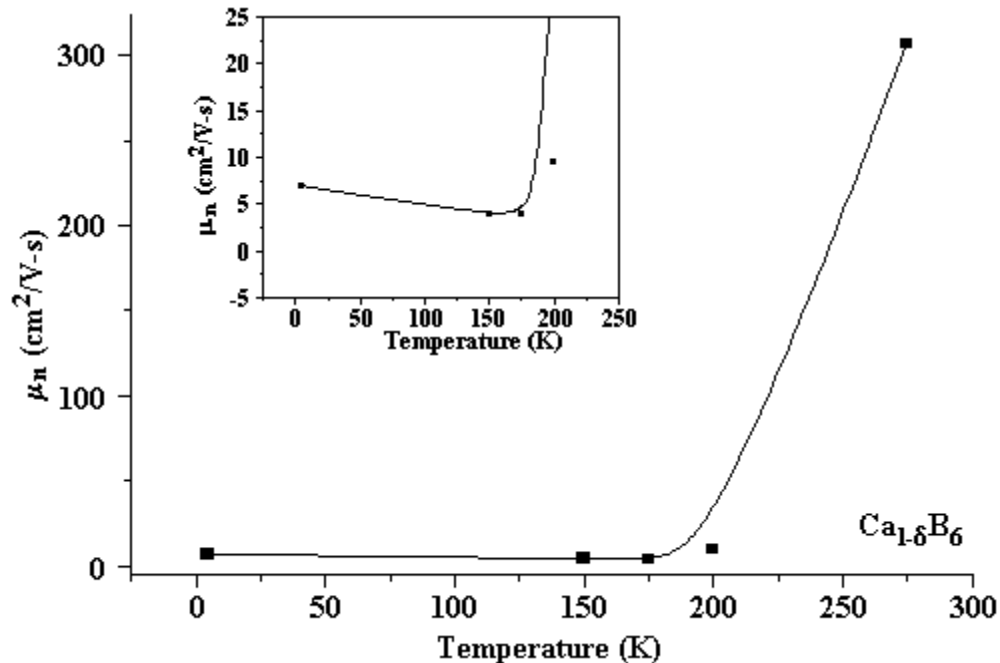


Figure 6-5. Hall mobility versus temperature in $\text{Ca}_{1-\delta}\text{B}_6$. The solid line is a guide for the eye. The inset shows in detail the temperature dependence in the low mobility regime.

In a fit to a semiconducting model where $\rho(T) = \rho_0 \exp(\Delta/k_B T)$, the two temperature ranges suggested by the resistivity can be individually interpreted to represent thermally activated behavior. The values of the gap can be compared, and it is found that the high-temperature gap of roughly 350 meV is larger by orders of magnitude than the low-temperature gap, which was found to be approximately 0.05 meV. This unusually small value may be susceptible to a significant amount of error, due to the comparatively large amount of thermal energy available to excite the electrons at these

temperatures. Nevertheless, activated transport is clearly seen in Figure 5-4 (b), and our results can be interpreted to indicate that inelastic effects are minimal at these temperatures.

The implication of our findings is that thermal activation over a large gap governs the high-temperature data. The low-temperature data seems to be dominated by a much smaller band gap, where lower-lying thermal excitations remain sufficient to promote carriers into the conducting regime. The large band gap frozen out at high temperatures may correspond to the intrinsic separation between the conduction and valence bands, while the small band gap could represent the presence of an impurity band residing very close to the bottom of the conduction band.

The value of ρ_0 in the relation $\rho(T) = \rho_0 \exp(\Delta/kT)$ can be easily obtained for the high temperature gap by noting the limiting value of the resistivity in the high temperature limit. By extrapolating the low temperature data to a high temperature limit, a different value of ρ_0 has been obtained. This difference in the high-temperature resistivities can be attributed to a difference in carrier population. For a two-gap model, such an analysis yields an effective population across the dominant gap at high temperature that is nearly 200 times that promoted across the low-temperature gap.

If we turn our attention to the magnetoresistance exhibited by this material, we find an effect at high field that is similar to its metallic relatives. We expect that paramagnetic splitting of the conduction band by the external field will produce a smaller gap for one spin band. The energy of the gap that dominates in the low temperature region of the data has been found to be nominally 0.05 meV. If we compare this energy to that of the field-induced paramagnetic splitting with $\mu_B H$ at 1 T being 6×10^{-5} eV, or

0.06 meV, we discover that the energy scales are very similar. In other words, the fields attained in experiment appear to be sufficient to induce a closing of the smaller band gap and the associated onset of semimetallic behavior. For fields above roughly 1 T, then, we expect this material to follow the simple Drude magnetoresistance behavior invoked to describe the magnetoresistance in $\text{Ca}_{1-\delta}\text{La}_\delta\text{B}_6$ and CaB_6 , a linear dependence on magnetic field in the limit of a majority spin band dominating charge transport.

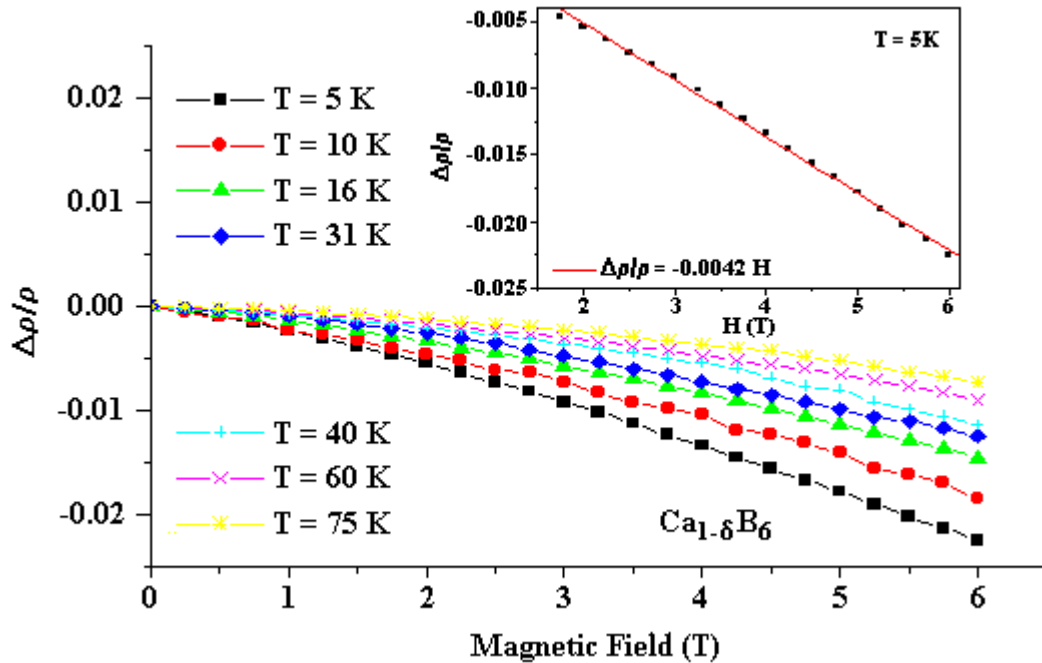


Figure 6-6. Magnetoresistance in $\text{Ca}_{1-\delta}\text{B}_6$ versus H with linear fit at $T = 5\text{ K}$ for $1.5\text{ T} < H < 6\text{ T}$ shown as inset.

The inset of Figure 6-6 shows a linear fit of magnetoresistance versus magnetic field between 1.5 T and 6 T. The coefficient is theoretically predicted to be approximately $-(\mu_B/\epsilon_F) = -10^{-3}\text{ T}^{-1}$, and the experimentally determined slope is of the same order at $-4 \times 10^{-3}\text{ T}^{-1}$. We consider this fit to be a successful one. The low field

behavior is less easily modeled, presumably because of a variety of contributions from a complex band structure in a regime between semimetallic and semiconducting behaviors.

6.2 Band Structure Model

The interpretations given above for all three compounds can be integrated to form a self-consistent model for this system. To begin, a candidate band structure model is presented in Figure 6-7. This model includes a gap between the conduction and valence bands. The conduction band may experience a splitting into spin up and spin down components in response to local moments, and this has been tentatively incorporated into the model as dashed curves. The position of the Fermi level depends on the doping level of the material.

The Fermi level of the La-doped compound is depicted in position (a). This positioning accounts for the metallic character exhibited by this material at temperatures greater than 28 K. A Fermi level position characteristic of the stoichiometric material is shown in position (b), though this positioning will vary with small changes in the ratio of Ca:B₆ of the crystal. A significant overlap of one band compared to the other may give rise to the two-domain behavior of the resistivity as a function of temperature, as shown in Figure 5-3. The Ca-deficient compound corresponds to the Fermi level in position (c), where an impurity band located at the Fermi level lies at higher energy than mid-gap to represent that the carriers are electrons.

The magnitude of the magnetoresistance for each sample is also consistent with the model. The metallic overlap of the Fermi levels for both the La-doped and parent materials imply the small magnetoresistances seen in experiment. There are two gaps

shown to reflect different activation energies associated with promotion from the valence and impurity bands into the conduction band.

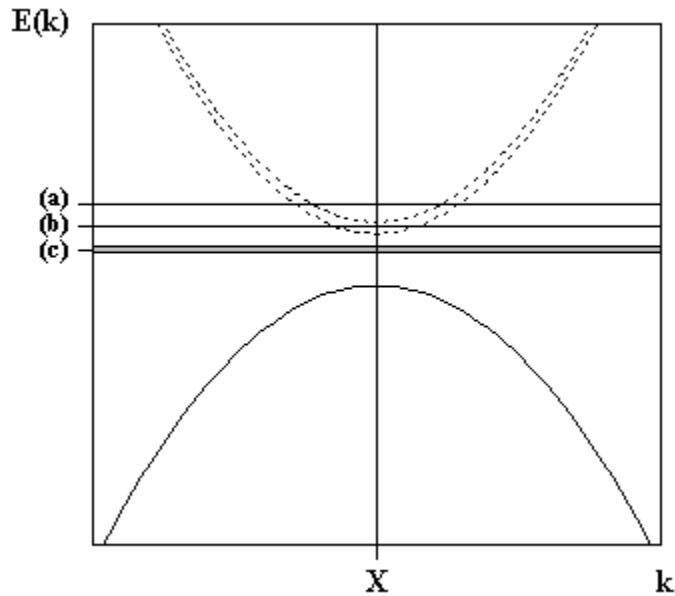


Figure 6-7. Band structure model depicting shifts in the Fermi level as a function of doping level:

- (a) $\text{Ca}_{1-\delta}\text{La}_\delta\text{B}_6$,
- (b) CaB_6 , and
- (c) $\text{Ca}_{1-\delta}\text{B}_6$ (shading indicates impurity band).

The suggestion of Monnier and Delley (see chapter 2) that there exist local moments with B_6 vacancies or anti-site substitutions is consistent with our picture. These workers suggest that the moments are confined to the surface of the single crystals, in moderate agreement with the ESR studies performed by Kunii, and to grain boundaries in polycrystalline samples. We propose that the moments need not be confined to the surface. Inhomogeneous distribution of these defects, as implied by the work of Terashima et al., is possible because of local fluctuations in temperature during Al flux growth. Not only could localized thermal pockets produce inhomogeneities, but

significant clustering of these defects may also occur more so in the flux growth method than in the more thermally uniform growth method of float-zone techniques. It may follow that larger magnetic domains, that is, larger clusters of B_6 defects, are formed more often in flux-grown single crystals than in float-zone grown single crystals.

The above discussion serves as justification for the correlation between Al flux growth and ferromagnetism, as discussed in chapter 2. The finding that La substitution for a B_6 octahedron lacks a magnetic moment serves to explain the disappearance of ferromagnetism at high La doping levels, where B_6 vacancies may begin to be filled with substitutional La. Because ferromagnetism appears to be confined to the two semimetallic systems, it may be that the order depends not only on the cluster size but also on the carrier concentration, possibly indicating a carrier-mediated exchange.

Variations in size of magnetic domains with differing growth conditions, such as temperature and technique, is a highly applicable speculation. The anomalous Hall effect data presented in Figure 5-10 are puzzling because of the disappearance of hysteretic behavior following the first application of magnetic field. This crystal may not be of a ferromagnetic nature. Instead, the domains may be in the paramagnetic or superparamagnetic regime so that full hysteresis is not seen. That the initial voltage at zero field differs from that seen in subsequent sweeps is yet unexplained, but the effect has been found to reappear upon thermal cycling of the sample. The apparent contradiction with the hysteresis present in magnetization versus field may be resolved by recognizing that, of the multiple samples used for the measurement, a fraction of the crystals could possess large domains and exhibit ferromagnetism, while the remaining crystals possess small domains and exhibit paramagnetism or superparamagnetism.

There are two conclusions we can draw about the hysteretic Hall voltage effect presented in this work: the agreement in saturation field with magnetization data indicates that the unusual first-sweep behavior appears to be related to the magnetic environment of the sample, and this La-doped crystal is most likely non-ferromagnetic.

We therefore believe our data to be consistent with the presence of inhomogeneous clustering of locally magnetic defects, the characteristic size of which determines the bulk magnetism in this material. A summary of this work is given in chapter 7 to follow.

CHAPTER 7 SUMMARY

This summary chapter serves as the closing of this dissertation. Section 7.1 will briefly reiterate the major results of this work, and suggestions for future experimental work on CaB_6 will be presented in section 7.2.

7.1 Synopsis of Experimental Results

The transport studies of La-doped, intended stoichiometric, and Ca-deficient CaB_6 have produced a number of clarifying results for single crystals grown by the Al flux technique. We have established that the crystals labeled CaB_6 exhibit semimetallic behavior, in contrast with expectations of intrinsic semiconductivity or perfect electron-hole compensation. This finding may imply that the CaB_6 samples are not truly stoichiometric, and some type of impurity or defect contributes electrons to the system. This identification has enabled a model band structure to be presented and has given rise to an improved understanding of the electronic environment present in this system.

Through results of resistivity, Hall effect, and mobility studies as a function of temperature and doping level, we suggest the existence of an impurity band in the semiconducting material, giving rise to the low-temperature plateau observed to correlate with off-stoichiometry effects. Vacancies of B_6 octahedra and anti-site substitutions are two possible defects that could produce an impurity band while also possessing a small magnetic moment, according to a recent theory. It is speculated in this work that these impurities are formed in clusters, in a process driven by local fluctuations in melt

temperature during growth. That the size of the clusters probably depends on growth conditions lends credence to a mechanism of interplay between an impurity-based magnetic moment and critical cluster size, possibly coupled with a lower limit on the carrier concentration in the case of a carrier-mediated magnetism, above which ferromagnetic order is possible.

7.2 Future Directions

CaB_6 may ultimately be successfully applied to the field of spintronics. There is much work to be done, however, before the integration can be accomplished. Further investigations into off-stoichiometry effects are imperative to the conclusive understanding of ferromagnetism in these compounds.

Complications to experimentation in these samples are associated with a charge current distribution within these crystals that is presently unclear and may be non-uniform through the thickness of the sample. Thin film growth may be a method of reducing the effects of inhomogeneous charge transport. Alternatively, efforts to fabricate thin films of these materials are expected facilitate several technical aspects of scientific investigations. A greater degree of dopant control may be achievable, and quality of electrical contacts could be significantly improved, including those required for possible future spin-polarized tunneling experiments to determine spin imbalance of charge carriers.

The formation of field-gated devices using CaB_6 as a counter-electrode may enable simultaneous study of the metal-insulator and ferromagnet-non-ferromagnet transitions. From a pure physics standpoint, the ability to observe these transitions could give rise to interesting experiments, while from a device standpoint, the manipulation of

charge carriers and modulation of the magnetism in a semiconducting environment at room temperature is a technological advance that is greatly anticipated.

LIST OF REFERENCES

- [1] H.C. Longuet-Higgins and M.deV. Roberts, "The electronic structure of the higher borides MB₆," *Proceedings of the Royal Society of London Series A, Mathematical and Physical Sciences* **224**, 336-347 (1954).
- [2] Robert W. Johnson and A.H. Daane, "Electron Requirements of Bonds in Metal Borides," *Journal of Chemical Physics* **38**, 425-432 (1963).
- [3] J.P. Mercurio, J. Etourneau, R. Naslain, and P. Hagenmuller, "Etude comparee des proprietes electriques des hexaborures d'euporium et d'ytterbium," *Materials Research Bulletin* **8**, 837-844 (1973).
- [4] R.E.J. Sears, "¹¹B chemical shifts and quadrupole coupling constants in the alkaline-earth hexaborides," *Journal of Chemical Physics* **76**, 5651-5652 (1982).
- [5] A. Hasegawa and A. Yanase, "Electronic structure of CaB₆," *Journal of Physics C: Solid State Physics* **12**, 5431-5440 (1979).
- [6] S. Massidda, A. Continenza, T.M. de Pascale, and R. Monnier, "Electronic structure of divalent hexaborides," *Zeitschrift fur Physik B* **102**, 83-89 (1997).
- [7] J. Etourneau and P. Hagenmuller, "Structure and physical features of the rare earth borides," *Philosophical Magazine B* **52**, 589-610 (1985) and references therein.
- [8] P.H. Schmidt and D.C. Joy, "Low work function electron emitter hexaborides," *Journal of Vacuum Science and Technology* **15**, 1809-1810 (1978).
- [9] J. Etourneau, J.P. Mercurio, R. Naslain, and P. Hagenmuller, "Structure electronique de quelques hexaborures de type CaB₆," *Journal of Solid State Chemistry* **2**, 333-342 (1970).
- [10] B.T. Matthias, T.H. Geballe, K. Andres, E. Corenzwit, G.W. Hull, and J.P. Maita, "Superconductivity and antiferromagnetism in boron-rich lattices," *Science* **159**, 530 (1968).
- [11] R.L. Cohen, M. Eibschutz, and K. West, "Electronic and magnetic structure of SmB₆," *Physical Review Letters* **24**, 383-386 (1970).
- [12] A. Menth, E. Buehler, and T.H. Geballe, "Magnetic and semiconducting properties of SmB₆," *Physical Review Letters* **22**, 295-297 (1969).

- [13] J.C. Nickerson, R.M. White, K.N. Lee, R. Bachmann, T.H. Geballe, and G.W. Hull, Jr., "Physical properties of SmB_6 ," *Physical Review B* **3**, 2030-2042 (1971).
- [14] J.W. Allen, B. Batlogg, and P. Wachter, "Large low-temperature Hall effect and resistivity in mixed-valent SmB_6 ," *Physical Review B* **20**, 4807-4813 (1979).
- [15] N.F. Mott, "Rare-earth compounds with mixed valencies," *Philosophical Magazine* **30**, 403-416 (1974).
- [16] B. Batlogg, P.H. Schmidt, and J.M. Rowell, "Evidence for a small energy gap in SmB_6 ," in *Valence Fluctuations in Solids*, L.M. Falicov, W. Hanke, and M.B. Maple, eds. (North-Holland Publishing Co., New York), 267-269 (1981).
- [17] S. von Molnar, T. Theis, A. Benoit, A. Briggs, J. Flouquet, J. Ravex, and Z. Fisk, "Study of the energy gap in single crystal SmB_6 ," in *Valence Instabilities*, P. Wachter and H. Boppart, eds. (North-Holland Publishing Co., New York), 389-395 (1982).
- [18] B. Amsler, Z. Fisk, J.L. Sarrao, S. von Molnar, M.W. Meisel, and F. Sharifi, "Electron tunneling studies of the hexaboride materials SmB_6 , EuB_6 , CeB_6 , and SrB_6 ," *Physical Review B* **57**, 8747-8750 (1998).
- [19] T. Kasuya, K. Takegahara, Y. Aoki, K. Hanzawa, M. Kasaya, S. Kunii, T. Fujita, N. Sato, H. Kimura, T. Komatsumbara, T. Furuno, and J. Rossat-Mignod, "Anomalous properties of valence fluctuating CeB_6 and SmB_6 ," in *Valence Fluctuations in Solids*, L.M. Falicov, W. Hanke, and M.B. Maple, eds. (North-Holland Publishing Co., New York), 215-224 (1981).
- [20] N.F. Mott in *Valence Instabilities*, P. Wachter and H. Boppart, eds. (North-Holland Publishing Co., New York.), 397-403 (1982).
- [21] Jozef Roman, Karol Flachbart, Thomas Herrmannsdorfer, Stephan Rehm, Frank Pobell, Elena S. Konovalova, and Youri B. Paderno, "Low temperature magnetic properties of samarium hexaboride," *Czechoslovak Journal of Physics* **46**, 1983-1984 (1996), Suppl. S4.
- [22] S. Gabani, K. Flachbart, P. Farkasovsky, V. Pavlik, I. Bat'ko, T. Herrmannsdorfer, E. Konovalova, and Y. Paderno, "The energy gap of SmB_6 at low temperatures," *Physica B* **259-261**, 345-346 (1999).
- [23] J.M. Effantin, J. Rossat-Mignod, P. Burlet, H. Bartholin, S. Kunii, and T. Kasuya, "Magnetic phase diagram of CeB_6 ," *Journal of Magnetism and Magnetic Materials* **47&48**, 145-148 (1985).

- [24] Z. Fisk, D.C. Johnston, B. Cornut, S. von Molnar, S. Oseroff, and R. Calvo, "Magnetic, transport, and thermal properties of ferromagnetic EuB_6 ," *Journal of Applied Physics* **50**, 1911-1913 (1979).
- [25] C.N. Guy, S. von Molnar, J. Etourneau, and Z. Fisk, "Charge transport and pressure dependence of T_C of single crystal, ferromagnetic EuB_6 ," *Solid State Communications* **33**, 1055-1058 (1980).
- [26] T. Kasuya, K. Takegahara, M. Kasuya, Y. Isikawa, and T. Fujita, "Electronic structure of EuB_6 , transport and magnetic properties," *Journal de Physique, Colloque C5* **41**, C5161-C5170 (1980).
- [27] S. Sullow, I. Prasad, S. Bogdanovich, M.C. Aronson, J.L. Sarrao, and Z. Fisk, "Magnetotransport in the low carrier density ferromagnet EuB_6 ," *Journal of Applied Physics* **87**, 5591-5593 (2000).
- [28] S. Sullow, I. Prasad, M.C. Aronson, S. Bogdanovich, J.L. Sarrao, and Z. Fisk, "Metallization and magnetic order in EuB_6 ," *Physical Review B* **62**, 11626-11632 (2000).
- [29] T. Fujita, M. Suzuki, and Y. Isikawa, "Specific heat of EuB_6 ," *Solid State Communications*. **33**, 947-950 (1980).
- [30] L. Degiorgi, E. Felder, H.R. Ott, J.L. Sarrao, and Z. Fisk, "Low-temperature anomalies and ferromagnetism of EuB_6 ," *Physical Review Letters* **79**, 5134-5137 (1997).
- [31] P. Nyhus, S. Yoon, M. Kauffman, S.L. Cooper, Z. Fisk, and J.L. Sarrao, "Spectroscopic study of bound magnetic polaron formation and the metal-semiconductor transition in EuB_6 ," *Physical Review B* **56**, 2717-2721 (1997).
- [32] M. Kasaya, J.M. Tarascon, J. Etourneau, and P. Hagenmuller, "Study of carbon-substituted EuB_6 ," *Materials Research Bulletin* **13**, 751-756 (1978).
- [33] S. von Molnar, J.M. Tarascon, and J. Etourneau, "Transport and magnetic properties of carbon doped EuB_6 ," *Journal of Applied Physics* **52**, 2158-2160 (1981).
- [34] J.M. Tarascon, J.L. Soubeyroux, J. Etourneau, and R. Georges, "Magnetic structures determined by neutron diffraction in the $\text{EuB}_{6-x}\text{C}_x$ system," *Solid State Communications*. **37**, 133-137 (1981).
- [35] Mitsuo Kasaya, Hitoshi Kimura, Yosikazu Isikawa, Toshizo Fujita, and Tadao Kasuya, "Valence instabilities and electrical properties of the La- and Yb-substituted SmB_6 " in *Valence Fluctuations in Solids*, L.M. Falicov, W. Hanke, and M.B. Maple, eds. (North-Holland Publishing Co., New York), 251-254 (1981).

- [36] D.P. Young, “Dilution studies of the Kondo insulators and alkaline earth and rare earth hexaborides,” Doctoral dissertation, Florida State University (1998).
- [37] D.P. Young, D. Hall, M.E. Torelli, Z. Fisk, J.L. Sarrao, J.D. Thompson, H.-R. Ott, S.B. Oseroff, R.G. Goodrich, and R. Zysler, “High-temperature weak ferromagnetism in a low-density free-electron gas.” *Nature* **397**, 412-414 (1999).
- [38] T. Kasuya, “Exchange-pair Jahn-Teller effects in GdB_6 ,” *Journal of Magnetism and Magnetic Materials* **174**, L28-L32 (1997).
- [39] J.L. Gavilano, B. Ambrosini, H.R. Ott, D.P. Young, and Z. Fisk, “Spin-lattice relaxation studies of selected hexaboride compounds,” *Physica B* **284-288**, 1359-1360 (2000).
- [40] L.V. Keldysh and Yu.V. Kopayev, “Possible instability of the semimetallic toward coulomb interaction,” *Soviet Physics – Solid State* **6**, 2219-2224 (1965).
- [41] Jacques des Cloizeaux, “Exciton instability and crystallographic anomalies in semiconductors,” *Journal of the Physics and Chemistry of Solids*, **26**, 259-266 (1965).
- [42] F. Bloch, *Zeitschrift Physik B* **57**, 549 (1929).
- [43] D.M. Ceperley and B.J. Alder, “Ground state of the electron gas by stochastic method,” *Physical Review Letters* **45**, 566-569 (1980).
- [44] David Ceperley, “Condensed-Matter Physics: Return of the itinerant electron,” *Nature* **397**, 386-387 (1999).
- [45] G. Ortiz, M. Harris, and P. Ballone, “Zero temperature phases of the electron gas,” *Physical Review Letters* **82**, 5317-5320 (1999).
- [46] H.J. Tromp, P. van Gelderen, P.J. Kelly, G. Brocks, and P.A. Bobbert, “ CaB_6 : a new semiconducting material for spin electronics,” *Physical Review Letters* **87**, 016401 (2001).
- [47] M.E. Zhitomirsky, T.M. Rice, and V.I. Anisimov, “Ferromagnetism in the hexaborides,” *Nature* **402**, 251-253 (1999).
- [48] Victor Barzykin and Lev P. Gor’kov, “Ferromagnetism and superstructure in $Ca_{1-x}La_xB_6$,” *Physical Review Letters* **84**, 2207-2210 (2000).
- [49] Leon Balents and Chandra M. Varma, “Ferromagnetism in doped excitonic insulators,” *Physical Review Letters* **84**, 1264-1267 (2000).

- [50] Takashi Ichinomiya, "Impurity-induced ferromagnetism in a doped triplet excitonic insulator," *Physical Review B* **63**, 045113 (2001).
- [51] B.I. Halperin and T.M. Rice in *Solid State Physics*, F. Seitz, D. Turnbull, and H. Ehrenreich, eds. (Academic Press, New York) **21**, 115-192 (1968).
- [52] L.J. Sham and M. Schluter, "Density functional theory of the band gap," *Physical Review Letters* **51**, 1888-1891 (1983).
- [53] J.E. Hirsch, "Metallic ferromagnetism without exchange splitting," *Physical Review B* **59**, 6256-6265 (1999).
- [54] T. Jarlborg, "Ferromagnetism below the Stoner limit in La-doped SrB₆," *Physical Review Letters* **85**, 186-189 (2000).
- [55] R. Monnier and B. Delley, "Point defects, ferromagnetism and transport in calcium hexaboride," *Physical Review Letters* **87**, 157204 (2001).
- [56] H.R. Ott, M. Chernikov, E. Felder, L. Degiorgi, E.G. Moshopoulou, J.L. Sarrao, and Z. Fisk, "Structure and low temperature properties of SrB₆," *Zeitschrift Physik B* **102**, 337-345 (1997).
- [57] P. Vonlanthen, E. Felder, L. Degiorgi, H.R. Ott, D.P. Young, A. D. Bianchi and Z. Fisk, "Electronic transport and thermal and optical properties of Ca_{1-x}La_xB₆," *Physical Review B* **62**, 10 076-10 082 (2000).
- [58] J.L. Gavilano, Sh. Mushkolaj, D. Rau, H.R. Ott, A. Bianchi, D.P. Young, and Z. Fisk, "Anomalous NMR spin-lattice relaxation in SrB₆ and Ca_{1-x}La_xB₆," *Physical Review B* **63**, 140410 (2001).
- [59] J.D. Denlinger, J.A. Clack, J.W. Allen, G.-H. Gweon, D.M. Poirier, C.G. Olson, J.L. Sarrao, A.D. Bianchi, and Z. Fisk, "Bulk band gaps in divalent hexaborides," *cond-mat/0107429* (2001).
- [60] Donovan Hall, D.P. Young, Z. Fisk, T.P. Murphy, E.C. Palm, A. Teklu, and R.G. Goodrich, "Fermi surface measurements on the low carrier density ferromagnet Ca_{1-x}La_xB₆ and SrB₆," *cond-mat/0104184* (2000).
- [61] Satoru Kunii, "Surface-layer ferromagnetism and strong surface anisotropy in Ca_{1-x}La_xB₆ (x = 0.005) evidenced by ferromagnetic resonance," *Journal of the Physical Society of Japan* **69**, 3789-3791 (2000).
- [62] Taichi Terashima, Chieko Terakura, Yuji Umeda, Noriaki Kimura, Haruyoshi Aoki, and Satoru Kunii, "Ferromagnetism vs. paramagnetism and false quantum oscillations in La-doped CaB₆," *Journal of the Physical Society of Japan* **69**, 2423-2426 (2000).

- [63] Tomoaki Morikawa, Takashi Nishioka, and Noriaki K. Sato, "Ferromagnetism induced by Ca vacancy in CaB_6 ," *Journal of the Physical Society of Japan* **70**, 341-344 (2001).
- [64] H. Munekata, H. Ohno, S. von Molnar, Armin Segmuller, L.L. Chang, and L. Esaki, "Diluted magnetic III-V semiconductors," *Physical Review Letters* **63**, 1849-1852 (1989).
- [65] N. Theodoropoulou, A.F. Hebard, M.E. Overberg, C.R. Abernathy, S.J. Pearton, S.N.G. Chu, and R.G. Wilson, "Magnetic and structural properties of Mn-implanted GaN," *Applied Physics Letters* **78**, 3475-3477 (2001).
- [66] I. Bat'ko, M. Bat'kova, K. Flachbart, J. Kovac, E.S. Konovalova, Yu.B. Paderno, and S. Ramakrishnan, "High residual resistivity of carbon doped EuB_6 ," *Solid State Communications* **98**, 895-898 (1996).
- [67] A. Lacerda, D. Rickel, M.F. Hundley, P.C. Canfield, J.D. Thompson, Z. Fisk, P. Haen, and F. Lapierre, "High field magnetoresistance in SmB_6 ," *Physica B* **199 & 200**, 469-470 (1994).
- [68] E.L. Wolf, *Principles of Electron Tunneling Spectroscopy*, Oxford University Press, New York, 20, 395-408 (1985).
- [69] W.L. McMillan and J.M. Rowell in *Superconductivity*, R.D. Parks, ed. (Dekker, New York) 561 (1969).
- [70] Michael Tinkham, *Introduction to Superconductivity*, (McGraw-Hill, New York) 70-74 (1996).
- [71] Heather D. Hudspeth, "Electron tunneling measurements on ferromagnetically doped lanthanum manganite films," Doctoral Dissertation, University of Florida (2000).
- [72] J.M. Rowell and Y.L.Y. Shen, *Physical Review Letters* **17**, 15 (1966).
- [73] F. Mezei and A. Zawadowski, *Physical Review B* **3**, 3127 (1971).
- [74] M.A. El-Semary, Y. Kaahwa, and J.S. Rogers, *Solid State Communications* **12**, 593 (1973).
- [75] J.R. Cooper and A.F.G. Wyatt, *Journal of Physics* **F3**, L120 (1973).
- [76] A.F.G. Wyatt, *Journal of Physics* **C7**, 1303 (1974).
- [77] L.J. van der Pauw, "A method of measuring specific resistivity and Hall effect of discs of arbitrary shape," *Philips Research Reports* **13**, 1-9 (1958).

- [78] N.F. Mott, *Metal-Insulator Transitions*, (Taylor and Francis, London) 21-22 (1990).
- [79] K. Takahashi, H. Nojiri, K. Ohoyama, M. Ohashi, Y. Yamaguchi, M. Motokawa, and S. Kunii, "Neutron-scattering study of DyB₆," *Journal of Magnetism and Magnetic Materials* **177-181**, 1097-1098 (1998).
- [80] V.V. Novikov, "Components of the low-temperature heat capacity of rare-earth hexaborides," *Physics of the Solid State* **43**, 300-304 (2001).
- [81] B.L. Altshuler and A.G. Aronov, "Contribution to the theory of disordered metals in strongly doped semiconductors," *Soviet Physics JETP* **50**, 968 (1979).
- [82] R.C. Dynes and P.A. Lee, "Localizations, interactions, and the metal-insulator transition," *Science* **223**, 355-360 (1984).
- [83] Charles Kittel, *Introduction to Solid State Physics*, (John Wiley and Sons, New York) p. 628 (1996).
- [84] P. Monod, "Magnetic Field Dependence of the Kondo Resistivity Minimum in CuFe and CuMn Alloys," *Physical Review Letters* **19**, 1113 (1967).
- [85] J.B. Bieri, A. Fert, G. Creuzet, and A. Schuhl, "Weak localisation in metallic glasses. I: magnetoresistance," *Journal of Physics F: Metal Physics* **16**, 2099-2118 (1986).

BIOGRAPHICAL SKETCH

Stephanie April Getty was born to Paul and Michelle Getty on April 12, 1977 in Douglasville, Georgia. At the age of ten months, she moved to Hialeah, Florida and remained a south Floridian until the age of seventeen. She began pre-school at Advent Montessori, and by the time she transferred to the first grade at a public school, she had learned the basics of cursive writing and multiplication. She credits the unconventional teaching techniques of the Montessori program with a great deal of her scholastic success to follow.

Stephanie graduated as salutatorian from Piper High School in June 1994. She decided to attend college at the University of Florida in Gainesville and, accompanied by 30 Advanced Placement credit hours, enrolled as a sophomore in the fall of 1994. She began to investigate the field of experimental condensed matter physics in December of 1996, under the advisement of Professor Gary Ihas. Her duties as undergraduate research assistant included the restoration of a ^4He cryostat, assisting in low temperature measurements of conducting polymers, and thermometry calibrations.

During the following summer, Stephanie participated in the Summer Research Program at Bell Laboratories, Lucent Technologies under the guidance of Dr. C.H. Chen. She learned to operate the transmission electron microscope and used bright field and selected area diffraction modes to characterize impurities in Ni films. Upon her return to the University of Florida, Stephanie continued work with Professor Gary Ihas until December of 1997.

At the mid-point of her fourth year, Stephanie began work under Professor Fred Sharifi. Initial experimental responsibilities focused on the preparation of substrates for applications to nanofabrication using electron-beam lithography. Before long, Stephanie was familiar with thin film growth and electron tunneling spectroscopy techniques and enjoyed her work to such a degree that she decided to continue her research under Professor Sharifi as a graduate student, beginning in August of 1998.

Stephanie's graduate studies included electron transport and tunneling measurements in the doped CaB_6 system. In addition, she demonstrated viability of a process to create evaporation masks of sub-micron features in thin Si_3N_4 membranes using electron-beam lithography. Her tunneling work also included the formation and preliminary study of tunnel junctions of UPt_3 , considered to be an unconventional superconductor.

In the spring of 2001, Stephanie's work with Professor Sharifi was concluded, and she proceeded to write her dissertation under the advisement of Professor Art Hebard. She hopes to obtain future employment either in industrial research or at a national laboratory.